University of Southampton

Faculty of Engineering and Physical Sciences

Engineering Materials

Investigation of Damage Initiation in Carbon Fibre Reinforced Polymer Composites Using Synchrotron Radiation Computed Tomography and Digital Volume Correlation

By Stephen Wilby

Thesis for the degree of Master of Philosophy

December 2020

Supervisors:

Professor S. Mark Spearing

Professor Ian Sinclair

Dr Mark Mavrogordato

Engineering Materials

Faculty of Engineering and Physical Sciences

UNIVERSITY OF SOUTHAMPTON

ABSTRACT

FACULTY OF ENGINEERING AND PHYSICAL SCIENCES

MASTER OF PHILOSOPHY

INVESTIGATION OF DAMAGE INITIATION IN CARBON FIBRE REINFORCED POLYMER COMPOSITES USING SYNCHROTRON RADIATION COMPUTED TOMOGRAPHY AND DIGITAL VOLUME CORRELATION

BY STEPHEN WILBY

Despite the vast interest in this critical research area, the complicated, interacting early stage damage mechanisms in cross ply Carbon Fibre Reinforced Polymers (CFRP) are poorly understood. The two-dimensional nature of the techniques commonly used to date in the analysis of these mechanisms is insufficient to adequately explain the three-dimensional nature of damage initiation. The work conducted in this research makes use of synchrotron radiation computed tomography (SRCT) in an effort to develop our understanding of the physical micromechanics associated with the earliest stages of damage initiation. Complementary techniques such as Digital Volume Correlation (DVC) and image segmentation have been used to analyse the strains associated with crack initiation in cross ply laminates loaded and imaged in 3D *in situ*. (The use of these techniques, to investigate damage initiation in CFRP is limited to the best of the author's knowledge). The use of SRCT and DVC has been evaluated to determine the techniques ability to track displacements in an anisotropic & heterogeneous material, the results of which show that reasonable levels of confidence may be achieved in measuring strain heterogeneity perpendicular to the fibres within a ply. The formation of transverse ply cracks is shown to correlate with an extended region of elevated tensile strain, which exists at lower loads than that at which the transverse ply crack formed. The study shows the usefulness of the SRCT technique in determining where damage initiates and the local strain state at initiation, which is potential significant for accurate and physically based initialization and validation of micromechanical models.

Keywords: damage initiation in carbon fire reinforced polymer, synchrotron radiation computed tomography, digital volume correlation, strain mapping.

List of Tables

List of Figures

List Of Acronyms

SIFT Strain Invariant Failure Theory
CT Computed tomography
DVC Digital Volume Correlation
DIC Digital Image Correlation
CFRP Carbon fibre reinforced polymer
ROI Region of interest
SRCT Synchrotron radiation computed tomography
ESRF European Synchrotron Research Facility

Declaration of Authorship

I, Stephen Wilby, declare that the thesis entitled 'Investigation of Damage Initiation in Carbon Fibre Reinforced Polymer Composites Using Synchrotron Radiation Computed Tomography and Digital Volume Correlation and the work presented in the thesis are both my own, and have been generated by me as the result of my own research.

I confirm that:

- This work was done wholly or mainly while in candidature for a research degree at this University;
- Where any part of this thesis has previously been submitted for a degree or any other qualification at this University of any other institution, this has been clearly stated;
- Where I have consulted the published work of others, this is always clearly attributed;
- Where I have quoted from the work of others, the source is always given.
- With the exception of such quotations, this thesis is entirely my own work;
- I have acknowledged all main sources of help;
- Where the thesis is based on work done by myself jointly with others, I have made clear exactly what was done by others and what I have contributed myself;
- Parts of this work have been submitted for publication as indicated.

Signed:

Date:

Acknowledgements

I wish to thank particular individuals and groups for which this work would otherwise not be possible. Firstly thanks to my three supervisors; Professor Mark Spearing, Professor Ian Sinclair and Dr Mark Mavrogordato for their knowledge, support and encouragement throughout the project. Thanks to Dr Richard Boardman, Dr Orestis Katsamenis mu-VIS, for their very much-appreciated help and support.

The work in this thesis benefited considerably through the use of synchrotron facilities at the Swiss Light Source (SLS) and the European Synchrotron Radiation Facility (ESRF). My particular thanks to assistance provided by Lucas Helfan for his expert knowledge and help on Beamline ID19 at the ESRF. My appreciation and thanks goes out to the staff at Boeing for the sponsorship and supply of materials used in this project. Particular thanks goes to Dan Charles, Sam Tucker, Joe Schaefer and Brian Justusson for their invaluable role as my technical points of contact. Thanks to the staff within the Faculty of Engineering and Physical Science, graduate school office and finance office for their tireless efforts behind the scenes.

I would like to thank my friends and colleagues at the University of Southampton, which made the PhD enjoyable to work on by providing invaluable advice for academic discussion and many distractions.

1 Introduction

1.1 Background and motivation

The high specific stiffness and strength, manufacturing flexibility and somewhat customisable properties of fibre-reinforced composites means that they have evolved to become an increasingly common choice for weight-critical structural applications, *e.g* primary structures in aerospace applications [1]. Most practical applications require a laminate stacking sequence with plies in several orientations to reinforce against multi-axial primary loading and incidental transverse loads [2]. However, off-axis plies are susceptible to fibre/matrix debonding, matrix cracking and delamination, which contribute to failure of the lamina [3-6]. The growing usage of carbon fibre composites has led to a demand by industry for improved performance modelling techniques. Due to the intrinsic difficulties in experimentally identifying and statistically quantifying damage initiation events, such as scale, number and location of debonds and micro-cracks, widely accepted models for damage initiation are yet to be established [7].

The Boeing Corporation's newest passenger jet, the 787 "Dreamliner" aircraft is fabricated from 50% by weight of composite material as seen in Figure 1-1. Each 787 contains approximately 35 metric tons of carbon fibre reinforced polymer (CFRP) [8]. Many other aircraft manufacturers such as Airbus and Russia's United Aircraft Corporation are using CFRP extensively in the production of their aircraft.

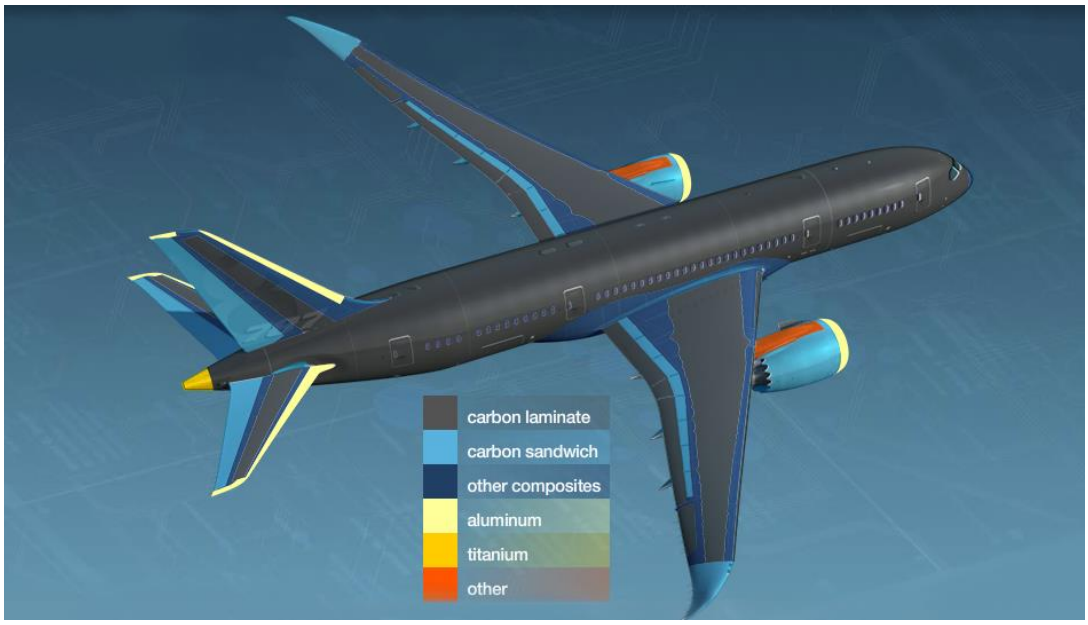

Figure 1-1: The material make-up of the Boeing 787 shows the fuselage and wings are predominately CFRP [8]

Accurate damage modeling prediction techniques in the design and construction of aircraft components could a) help to reduce the expensive and time consuming, multiscale physical testing programmes currently used to ensure

aircraft safety and b) exploit optimisation techniques, thus reducing the tendency of current manufacturers to over-engineer components fabricated using CFRP.

Gosse and Christensen developed an early stage damage prediction model, designed to predict the initiation of damage in composite materials [9]. Their model, "The Onset Theory" (formerly the strain invariant failure theory or SIFT) uses two strain invariants, distortion and dilatation, to predict damage initiation. As described in 2.4.4.1, they suggest that the strategy allows them to determine the strains at which damage will initiate in laminated material [10]. Significant experimental challenges exist in the direct visualization of damage at (a) microstructural relevant length-scales, (b) under mechanically representative conditions, and (c) in realistic composite microstructures. As such mechanistic initialization and precise physical calibration/validation of models is difficult.

The use of computed tomography (CT) as a material investigation tool has gathered momentum in the last two decades, which has led to a wide range of lab-based and synchrotron-based computed tomography facilities becoming available to the materials researcher. The use of micro-focus computed tomography ('microCT') to investigate carbon fibre reinforced polymer materials has been documented [11-16] and has been used to inform and develop modelling capabilities of interply crack damage progression [16]. Computed tomography offers a volumetric, three-dimensional view of a region of interest within an otherwise opaque material. With achievable voxel resolution as low as a few tens of nanometres, the benefits of CT as applied to CFRP include the ability to test *in situ,* resolve individual fibres, polymer matrix, toughening particles and the air gaps associated with voids and damage. Figure 1-2 is an example CT image showing a transverse ply crack in a CFRP coupon loaded and scanned *in situ*.

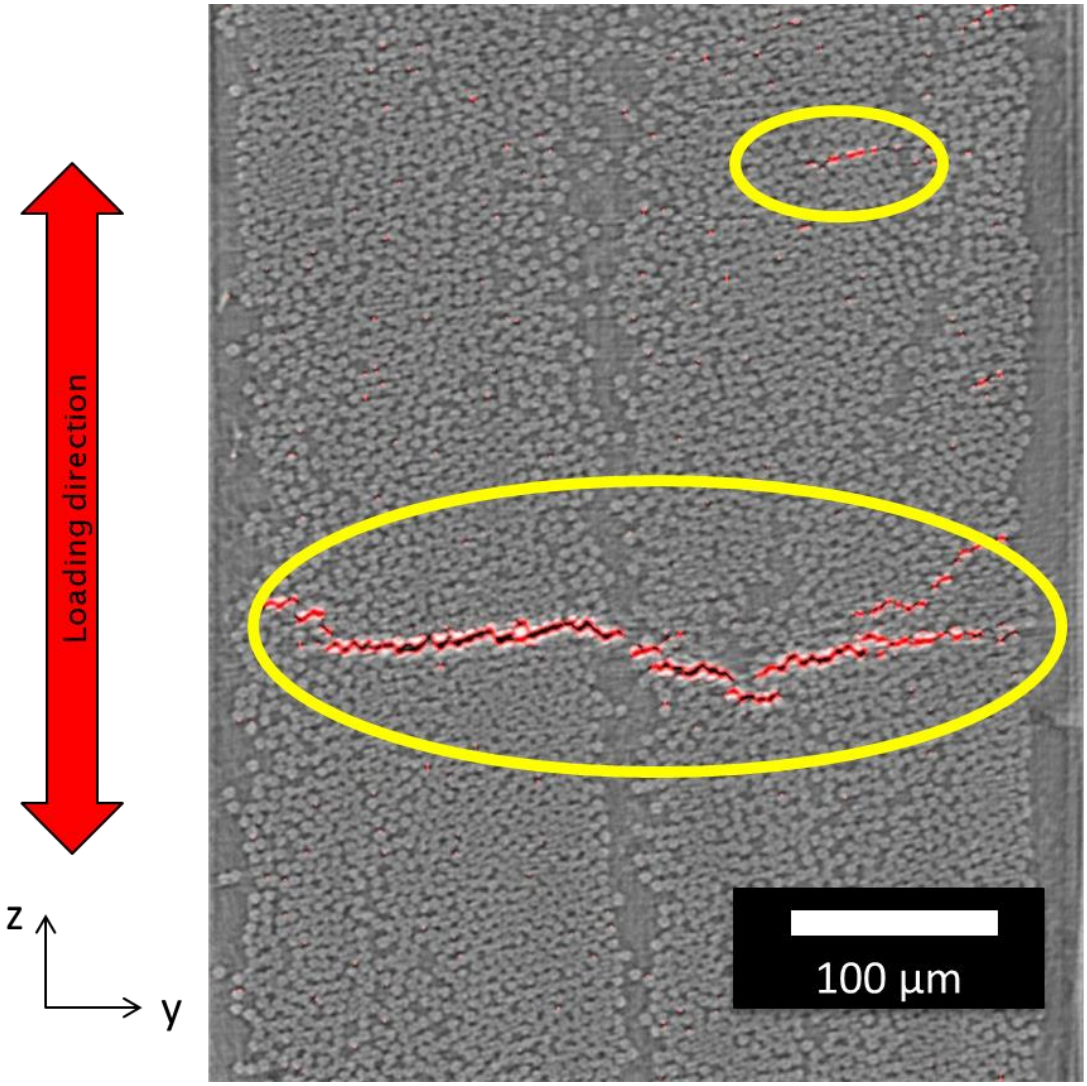

Figure 1-2: CT image of a transverse ply crack in $[0,90]_{2s}$ CFRP loaded and scanned *in situ*.

In conjunction with three dimensional, volumetric imaging via computed tomography, digital volume correlation (DVC), the three-dimensional extension of digital image correlation (DIC) has been shown to identify displacements and the location of microstructural-scale strains in studies on a range of materials, including metallic foams and concrete [17-20]. More recently it has been used on carbon fibre reinforced polymer materials [16, 21, 22]. DVC has been used to identify the location and magnitude of strains in these materials, with the corresponding potential to verify strain maps generated by finite element models [23, 24]. Most recently it has been the displacement values generated by DVC that have been of interest [25-27]. By directly meshing and importing the microstructure of the volume of interest into a finite element model and using the recorded DVC displacement values to define the boundary conditions of the volume, detailed materials models may be realised. Accurate strain values can then be extracted from the finite element analysis, which can be used to validate and inform techniques such as onset theory.

1.2 Aim and Objectives

1.2.1 Aim:

Developing our understanding of damage initiation in CFRP has always been of great interest. Despite this interest the mechanisms of early stage damage are poorly understood. Due to the three-dimensional nature of damage initiation two-dimensional techniques are not adequate to describe the complicated mechanics. The aim of the research is to develop our understanding of damage initiation in CFRP using SRCT and DVC, two established three-dimensional imaging and analysis techniques, whose use is limited in this area of interest (to the best of the author's knowledge).

1.2.2 Objectives:

- Use and validation of high-resolution computed tomography to capture the earliest stages of fibre-matrix transverse microcrack initiation in CFRP.

- Use and validation of DVC used on volumetric scans at the identified crack location (imaged during prior load steps) to detect local strains and therefore characterise the driving forces for microcracking.

- As part of the DVC validation, determine accuracy of the displacement values from DVC. Ultimately these displacement values may be used as calibration and modelling boundary conditions (for multiscale models) for the first time in a study looking at transverse damage initiation in composite materials.

1.3 Research Novelty

SRCT and DVC are established tools in the study of materials; both techniques have been recently used to characterise damage in CFRP [11-16, 21,22]. To the best of the authors knowledge this is the first study to use both SRCT and DVC in conjunction to characterise damage initiation in CFRP. Although limited analysis has been conducted in this study, the development and validation of the techniques for both SRCT and DVC in conjunction may be of use in future studies.

1.4 Thesis Outline

- Chapter 1 is an introduction to the topic, a brief outline of the techniques used and the aims and objectives of the research.

- Chapter 2 describes the basic principles of unidirectional composite material layup and a literature review describing current methods of investigation and the techniques used in this work.

- Chapter 3 is a description of the methods and materials used in the study.

- Chapter 4 Is a self-contained article describing methods and validation of the SRCT and DVC techniques.

- Chapter 5 Is a self-contained article containing details of the work conducted

with regards to the characterisation of damage initiation.

2 Literature Review

2.1 Composite Damage Initiation

2.1.1 Introduction

The ability to analyse composite materials on different scales, depending on the focus of the investigation is incredibly important [28]. The macroscopic behaviour of composite material is determined by characteristics at lower length scales [28]. Research has emphasized the need to model composite materials at different length scales including micromechanical, macro mechanical, laminate and structural levels [29]. Developments in computational capabilities have led to the study of finer levels including the atomic level using molecular dynamics (MD) simulation [28]. The micromechanical scale will be considered in this work.

At the micromechanical level, fibre and matrix are clearly distinguishable materials with different constitutive behaviour [30]. The interaction between fibre and matrix can be studied in detail. Rule of mixtures, analytical micromechanics and unit cell modelling are among the techniques used at this level to predict the response and properties of a composite given the constitutive properties and geometrical arrangement [30]. Local stress and strain effects in the fibre and matrix are also studied at the micromechanical level for given load states, phase properties and phase geometries. Scanning electron microscopy, and optical microscopy are examples of the methods used to capture material response at the micromechanical scale [31, 32].

2.1.2 Anisotropic Material and Axes Definition

Unidirectional, long fibre composite laminae are highly anisotropic with the main load carrying capability in the fibre direction [33]. It is conventional when describing the principal axis of the lamina to assign the fibre direction as 1; the transverse principal axes are designated 2 and 3 respectively as seen in Figure 2-1 [34].

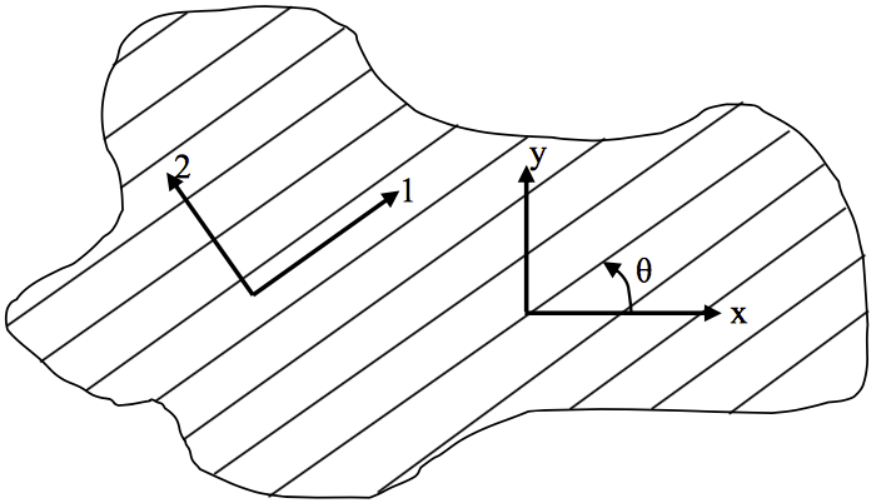

Figure 2-1: Definition of the principal axis of long fibre composite material showing principal axis 1 and 2 and loading axis x and y [34].

The load carrying capability in the transverse directions is significantly lower than in the fibre direction as the material's mechanical properties depend largely on the matrix and the bond strength at the fibre matrix interface in these planes [33]. Designers of composite components, can allow for this anisotropy in material properties by specifying multiple laminae orientations in a stacking sequence of varying orientations, which will allow a given component to carry any predicted multiaxial load cases [33]. Figure 2-2 shows unidirectional laminate layup vs a notional quasi-isotropic laminate design. It is convention to define 0° as the direction of the principal load and the cross plies at the angle which they were laid down relative to this. The quasi-isotropic laminate depicted in Figure 2-2 is designated as a [0, 90, + 45, -45, -45, +45, 90, 0] symmetrical layup or simply $[0/90/ +45/-45]_s$. In this example the 0° layers provide axial strength and stiffness, the +/- 45° provide shear and torsional strength and stiffness and the 90° layers provide transverse strength and stiffness that is ideal for creating a consolidating layer that keeps everything together [33].

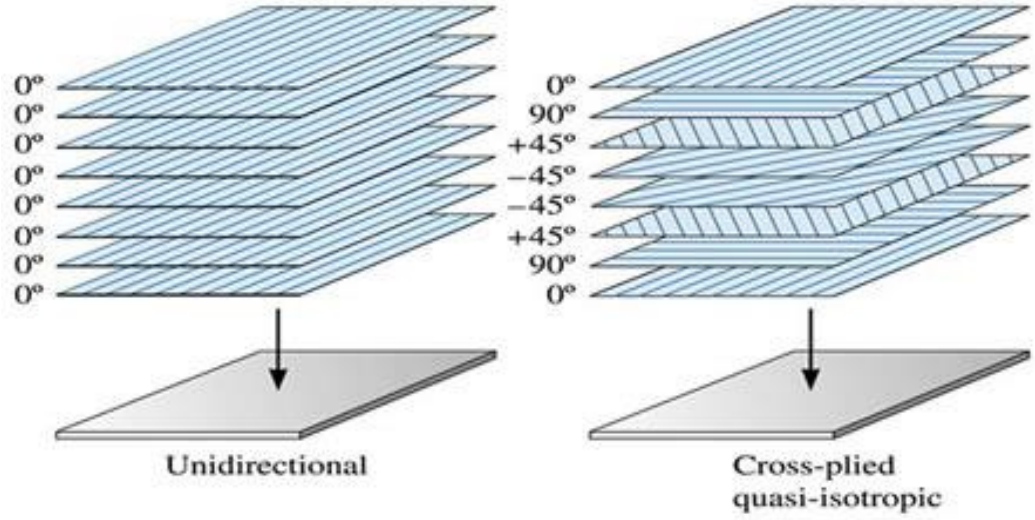

Figure 2-2: A unidirectional laminate vs a quasi-isotropic laminate [0/90/ +45/-45]s [35]

Laminate plate theories are used to predict the properties of the structural element based on the material lamina properties, layup and geometry. Two and three-dimensional approaches (equivalent single layer theories and three-dimensional elasticity theories respectively) are commonly used. Two-dimensional equivalent single layer theories include classical laminate plate theory (CLPT) and first (FSDT) and higher (HSDT) order shear deformation theory. CLPT is used to calculate structural properties in this work.

Classical Laminate Plate Theory

CLPT is based on the Kirchoff-Love hypothesis for plates and shells, which provides a good approximation when the plate is thin. "Thin" is a combination of geometry and material properties. CLPT is used considering a number of assumptions:

- Straight lines perpendicular to the mid-surface before deformation remain straight after deformation

- Transverse normals do not experience elongation (i.e they are inextensible) – transverse normal strains $\varepsilon_z = 0$.

- Transverse normals rotate such that they remain perpendicular to the mid-surface after deformation – transverse shear strains $\varepsilon_{xz} = \varepsilon_{yz} = 0$.

- Linear theory, thus:

    - u(x,y,z), v(x,y,z) and w(x,y,z) are small compared to plate thickness
    - In plane strains ε_x, ε_y and γ_{xy} are small compared to unity.

CLPT gives excellent results for many problems particularly if the average structural properties, i.e those at the centre, are required. The limitations of the theory mean that interlaminar stresses from stress strain relations cannot be predicted. Interlaminar shear stresses are usually highest at a layer interface and at or near a free edge of a laminate.

2.1.3 Damage Initiation

In quasi-isotropic and similar multi-angle laminates it is widely accepted that fibre-matrix debonding leading to microcracking is the first identifiable indication of damage. Initiation occurs in the plies off-axis with regard to the direction of applied load, during tensile deformation, with the orthogonal, 90° plies most susceptible [4]. Microcracking in the 90° plies can occur at relatively low strains compared to the ultimate fracture strain of the laminate and the development and progression of microcracks have significant implications on the long term durability and performance of the material [36]. When cracking initiates in the 90° plies, the stress is redistributed through the adjacent plies and cracks continue to develop as the applied load is increased until the ply is saturated with cracks [37, 38]. The elastic properties of the composite are dominated by the plies with fibres orientated in the direction of the applied load [39]. The accumulation of cracks in the transverse plies results in a slight degradation in the elastic modulus, and this slight change in modulus is often utilised as a relative measure of damage [40]. The imaging of this damage is made difficult as only small permanent deformations remain in the stress-free body after unloading. In order to identify the initiation and progression of microcracking, *in situ* micro-focus imaging techniques such as scanning electron microscopy (SEM), optical microscopy and CT are required [41].

2.1.4 *In situ* Micro-Focus Composite Material Imaging

In early work conducted on the initiation of damage in composite materials Gamstedt *et al* [42] examine the mechanism of transverse ply crack initiation in their study of tension-compression fatigue of glass fibre composite laminates containing transverse plies. They determined, with the use of *in situ* optical microscopy during a tensile test, that the first damage to develop was interfacial debonding at the free edge. Fibre/ matrix debonds coalesced as the specimen was further strained, and formed a transverse crack, Figure 2-3. At low loads,

debonds were widespread and easy to find. The transverse cracks, which ensued, were scarce and emerged stochastically, making further debonds ahead of the crack tip difficult to identify. This highlights the need for an analysis technique, which is capable of detecting strains ahead of crack formation and propagation. The *in-situ* technique used in this study is based on a two-dimensional view of the area of interest and debond propagation along the fibre direction was not observed.

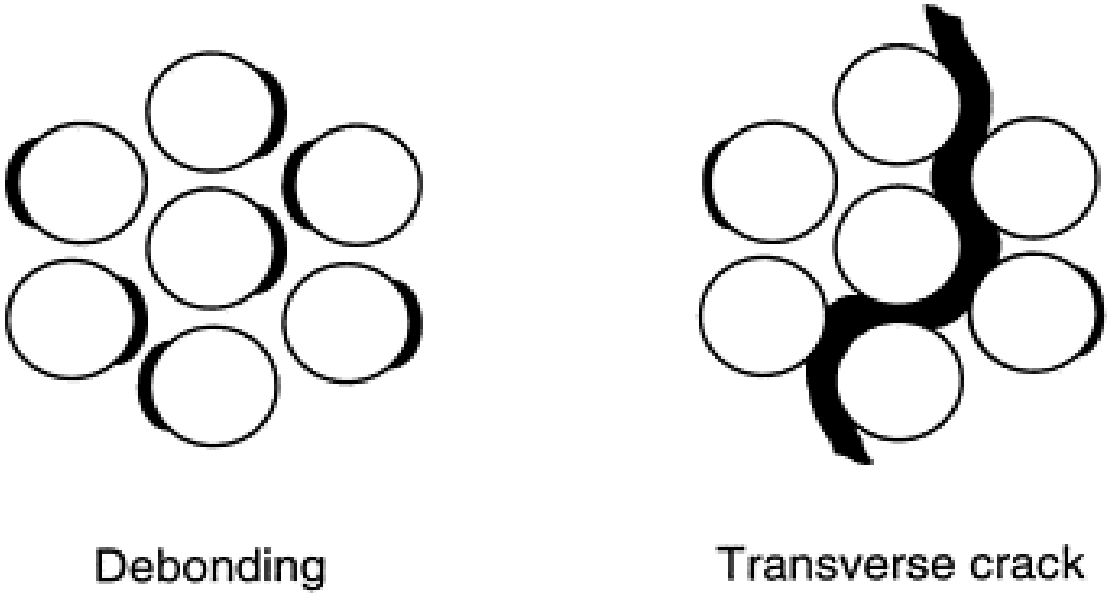

Figure 2-3: Debonds coalesce leading to transverse cracks [41]

Building on the work conducted by Gamstedt *et al*, Martyniuk *et al* [3] conducted an investigation to determine the evolution of fibre/matrix interfacial debonding using X-ray micro tomography to deliver a three-dimensional view of the volume of interest. They use a single glass fibre embedded in a polymer matrix orientated transverse to the direction of load, geometry shown in Figure 2-4.

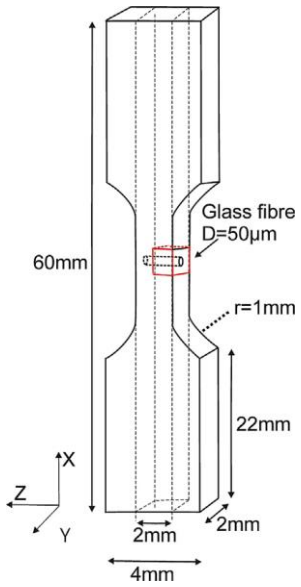

Figure 2-4: The geometry tested by Martyniuk *et al* [3]

In situ testing was conducted at the Swiss Light Source using the TOMCAT beamline. An acoustic emission sensor was also used in the testing to determine when damage initiation events were occurring during loading. Incremental load steps of 5-10 MPa were applied to the test specimen. After each application of stress, the load was backed off 30% in order to minimize deformation. The coupon was then scanned and the results of each load step were analysed. The researchers found that at each load step the fibre/matrix debond widened and propagated along the fibre from the free edge, as seen in Figure 2-5 - Figure 2-7. It is also worth noting the imaging artefact that is identified, highlighted by the red arrow, in both of the images Figure 2-5 when the fibre is parallel to the path of the beam, this artefact will be discussed in 3.4.2.

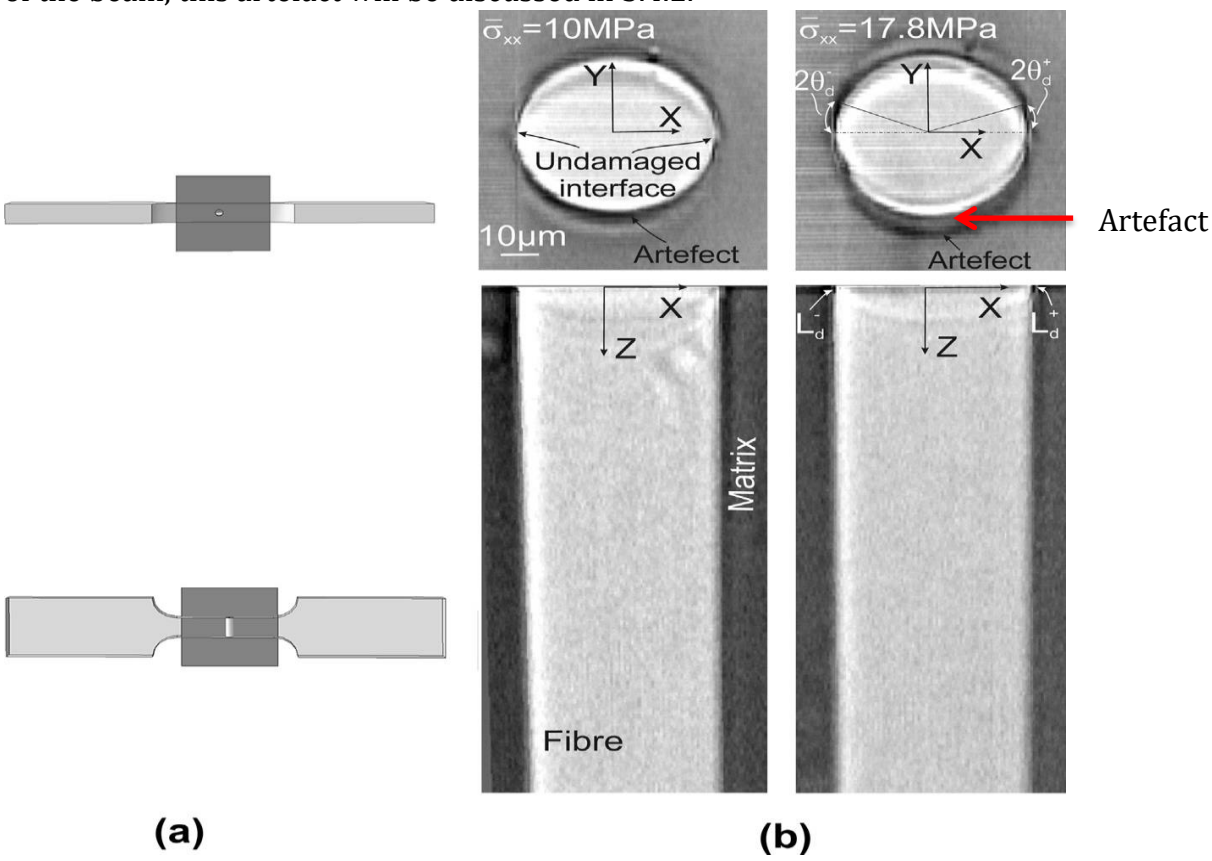

Figure 2-5: Debonds start at the free edge. Note the artefact in the image [3]

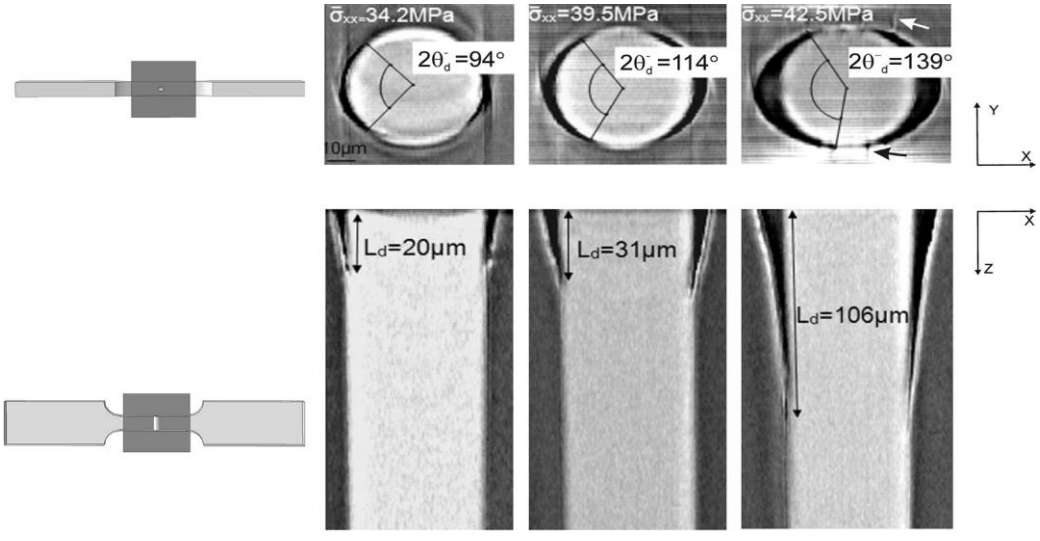

Figure 2-6: The debonds grow and propagate along the length of the fibre [3]

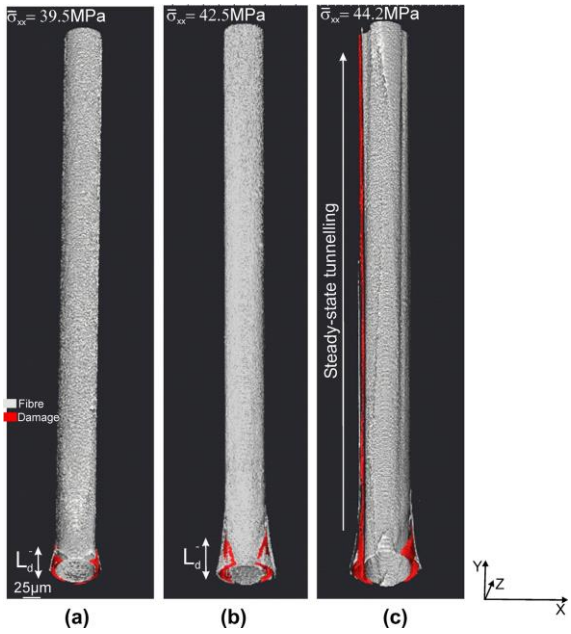

Figure 2-7: The propagation of debonds along the fibre [3]

The results also show that at a higher load a crack kinks into the bulk of the matrix in the location shown in Figure 2-7 and Figure 2-8.

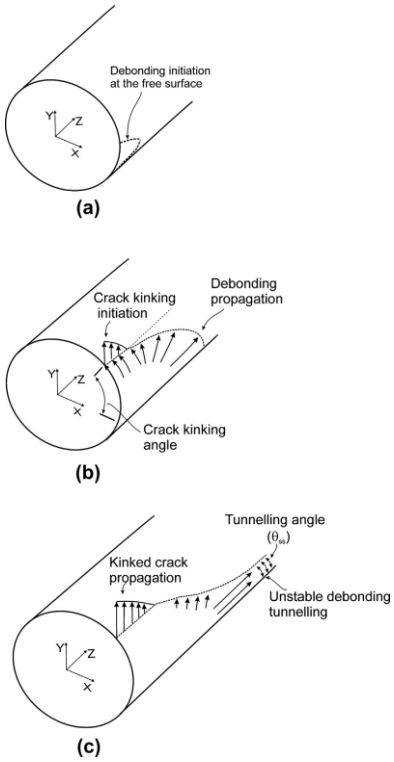

Figure 2-8: Kinked cracks appear as the debond propagates [3]

This experiment may be considered limited in that a single fibre is used and does not determine the impact that the interaction with other fibres may have on initiation. Research has shown that such cracks grow around multiple fibres, coalesce and lead to transverse matrix cracking [43]. The study shows that damage initiation investigations require three-dimensional observations as two-

dimensional surface observation would not adequately describe the fibre/ matrix debond along the length of the fibre. The authors acknowledge that the fibre diameter may have an influence on debond and progression but do not mention the effect multiple fibres or cross plies may have.

Mortell *et al* [44] conducted an investigation into damage initiation and progression using *in situ* SEM micro-mechanical testing on CFRP under bending loads. The experiment was carried out using two layups of the material, first a $[0,90]_s$ was used to study the initiation of damage in transverse plies followed by a $[90,0]_s$ to study damage progression. The material was subjected to a bending load and real time video footage was captured. They found that the initial form of failure was fibre/ matrix debonding in the transverse plies. It was observed that the debond is located at the part of the interface closest to the adjacent fibre where the tensile load direction is perpendicular to the debond, this encourages failure at that location. This observation aligns with those of Maligno *et al* [45] whose work found that when fibres are less than 0.05 μm apart, even small values of chemical shrinkage could cause matrix failure between two fibres. Mortell [44] reinforces this with the observation that when fibres are this close and share an interface, the debonding mechanism will favour one fibre over the other and continue separating that fibre from the matrix, Figure 2-9. This highlights the importance of determining the local fibre volume fraction in studies where damage initiation is the main focus.

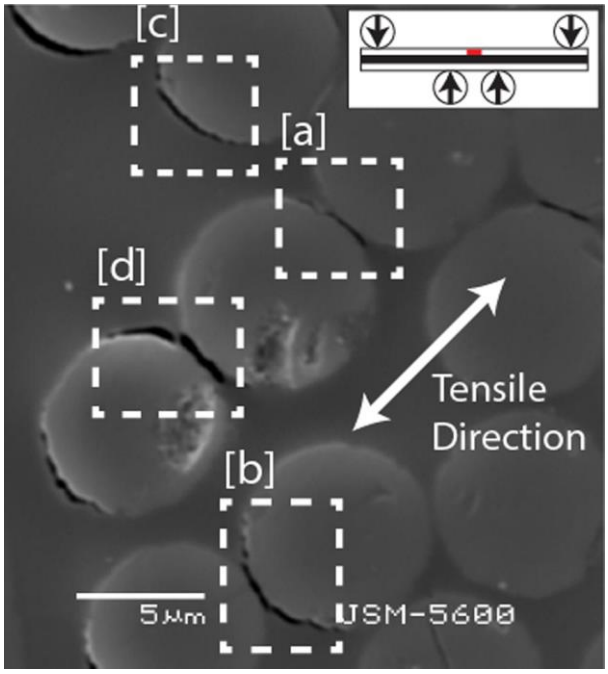

Figure 2-9: SEM investigation into damage initiation, the debonds form orthogonal to the tensile direction [43]

The authors go on to observe the micro-crack growth as debonds grow. It was determined that the growth occurred between one fibre to the next closest with the gaps between the fibres bridged by matrix cracking as seen in Figure 2-10. This indicates that the matrix is the weakest medium for crack propagation. Hobbiebrunken *et al* [46], who also used SEM to study fibre-matrix debonds, observed that as widespread fibre matrix debond grew, small resin bridges

formed between them. Under sustained or increased loading, these resin bridges underwent significant plastic deformation until they ruptured. Mortell *et al's* [44] observation was further reinforced when the crack continued to grow and propagate into resin rich pockets and progress to the next nearest, favourably-debonded, fibre-matrix interface.

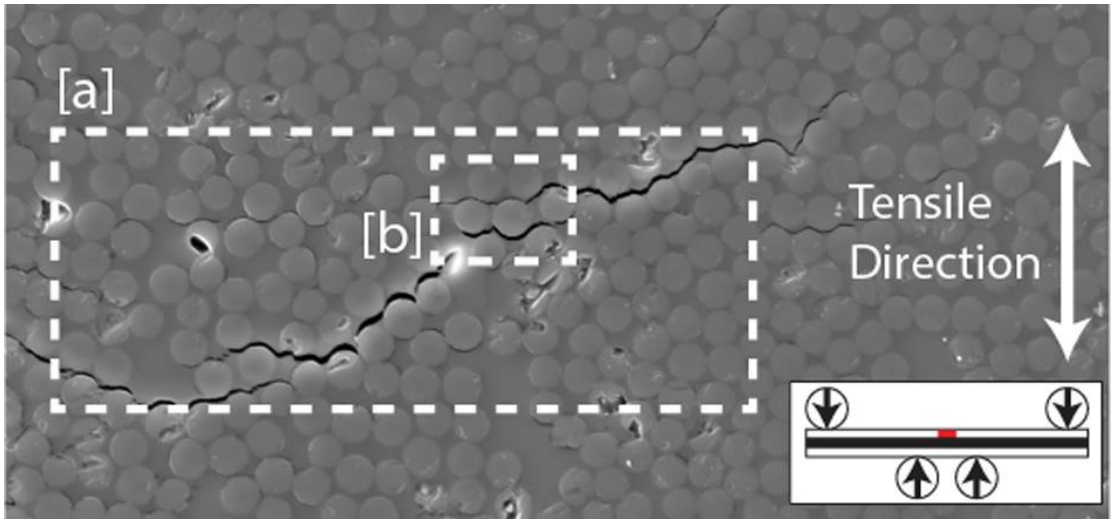

Figure 2-10: The image shows that microcrack propagates through resin rich regions [43]

The authors of this paper offer an account of the initiation and propagation of damage in CFRP using micro-focus techniques and it is clear that the fibre volume fraction of the material plays an important role in damage initiation and propagation. The two-dimensional nature of the technique means that they are unable to track the propagation of the crack through the thickness, along the fibres in the material.

Vaughan and McCarthy [47] collectively investigate the effects of thermal residual stress and fibre-matrix debonding on the transverse behaviour of a fibre reinforced composite. They utilise a strategy described in by Llorca *et al* [48]] and Sato and colleagues [49] where, a cohesive zone model is used to predict the onset of fibre-matrix debonding. The non-linear behaviour in the matrix phase is modelled using the Mohr-Coulomb plasticity theory. A nearest neighbour algorithm, described by Vaughan *et al* [50] and more recently by Ge *et al* [51], is used to reproduce a statistically equivalent fibre distribution for the high volume fraction composites under investigation. They study the thermal residual stress, caused by the temperature change from the curing process on the transverse fracture process and go on to investigate damage accumulation due to cyclic loading to better understand the role that fibre-matrix debonding and matrix plasticity play in the macroscopic response of the composite. Three numerical studies were carried out: 1) a linear elastic analysis to examine the microscopic stress following thermal cool-down from cure temperature. The Interfacial Normal Stress (INS) and the Interfacial Shear Stress (ISS) are of particular interest. 2) The transverse fracture behaviour as a result of fibre-matrix debonding is examined using mechanical and thermal loading. 3) The material is subject to a tensile/ compressive loading regime and the effects of microscopic damage accumulation on the macroscopic response is analysed.

The results of part 1) of their study, in which they study the effect of thermal residual stresses, are shown in Figure 2-11. The authors demonstrate that values for both INS and ISS are higher when the inter-fibre spacing is smaller. This, we are told, is the case across the area of interest. The maximum compressive INS is centrally located between two closely neighbouring fibres whereas the ISS is offset either side of this central location toward the matrix rich region, both shown at point A in Figure 2-11. Compressive INS has been shown to be beneficial to upon mechanical transverse loading [52], while the ISS may contribute to early onset of damage [53].

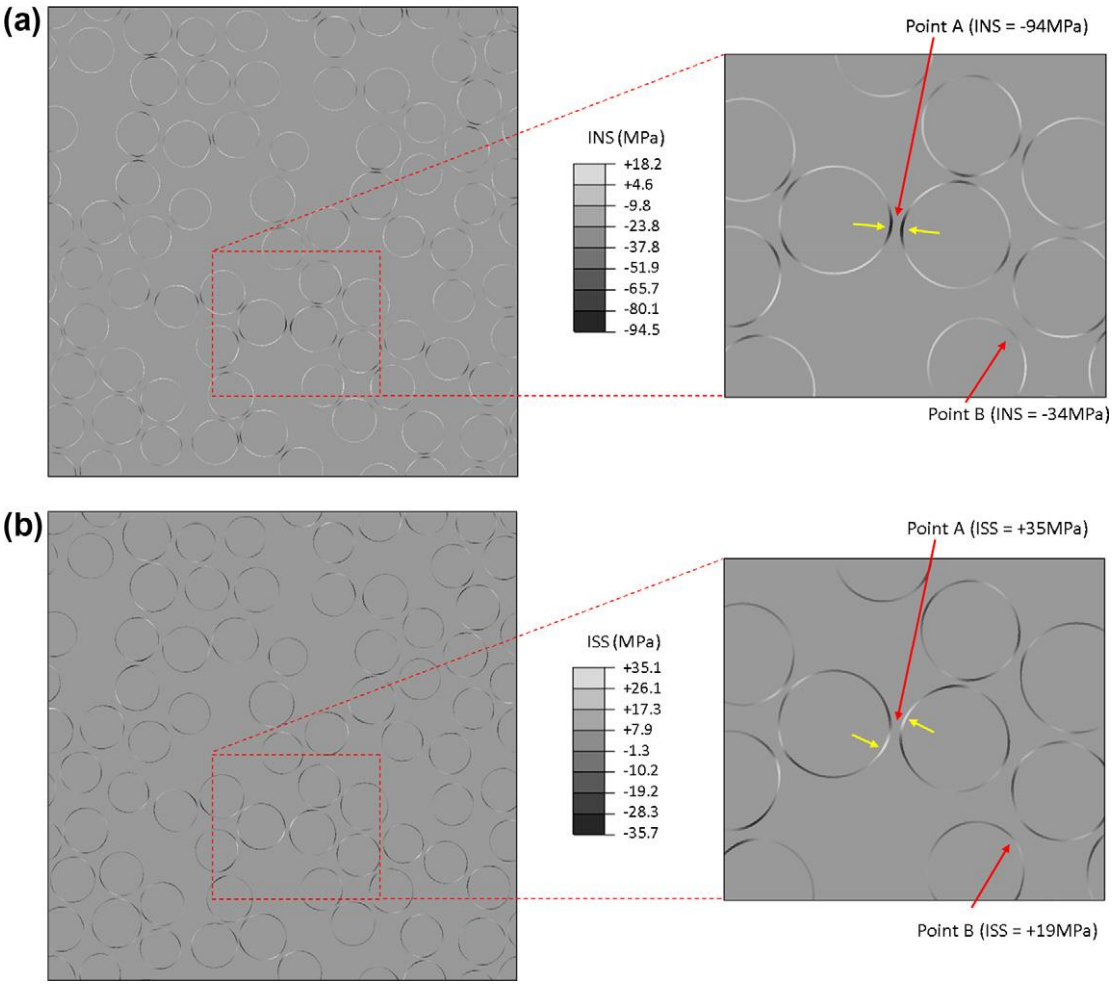

Figure 2-11: The results of the study show that the INS and and the ISS both increase as the inter-fibre spacing decreased [46].

The influence of the fibre-matrix debonding on transverse fracture behaviour was examined using a cohesive zone model at the fibre-matrix interface. Normal (t_n^0) and shear strengths ((t_s^0) of the interface elements were varied to predict a range of fibre-matrix interface strengths. Interfacial fracture energy was used to control damage evolution at the interface. The value used in this study was $10 J/m^2$,which, while being relatively low and representing a somewhat brittle behaviour of the fibre-matrix interface, observation of the material suggests this type of performance, Figure 2-12(a). Figure 2-12(a) also show the response curves of an RVE with a range of interfacial strengths for both the thermo-mechanical loading (TML) and the mechanical loading (ML) cases. It is clear that the interfacial strength has an effect on macroscopic response, with a higher

transverse strength being seen for increasing interface strength for both loading cases.

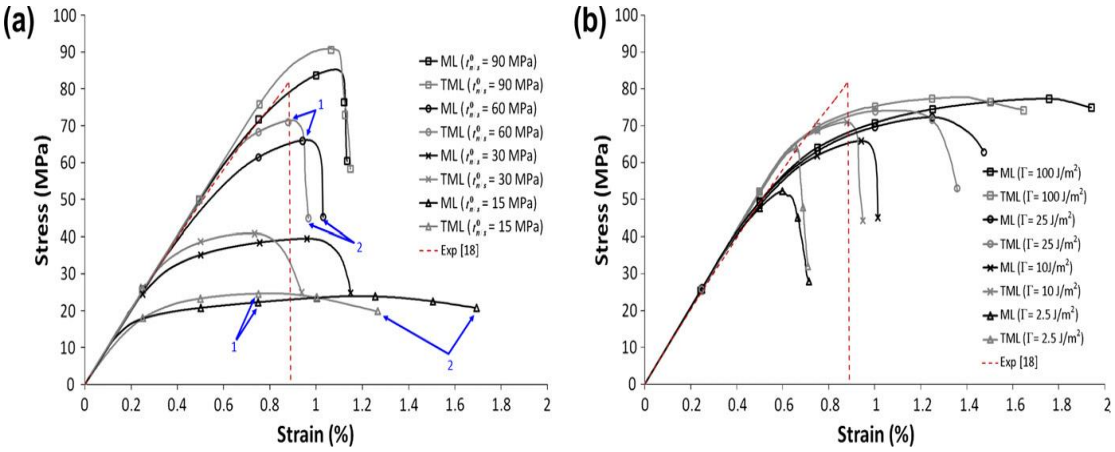

Figure 2-12 (a): Transverse fracture behaviour of an RVE for various interfacial strengths. (b) Influence on fracture energy of the transverse fracture behaviour [46].

Figure 2-12 (b) shows the results of the investigation into the influence on interfacial fracture on the transverse deformation. Three further interfacial fracture energies, brittle and more ductile were considered. The first observation made in the study is that non-linear behaviour occurs at the same point of loading in each case, as the interface strength is the same for all cases ($t^0_{n/s} = 60\ MPa$). Their study highlights the fact that a lower interface energy reduces transverse strength whereas the higher interface strength caused a more ductile macroscopic response. An important observation of increasing the fracture energy has been the increased strain to failure of the composite. This has implications, as it is the low strain to failure of transverse plies that cause damage initiation in cross ply laminates [43].

The authors conclude by saying that the presence of a weak fibre-matrix interface coupled with thermal residual stress can have a detrimental effect causing interfacial cracks to develop during the curing process, thus implicating the manufacturing process in the role of damage initiation. Also reinforced is the effect of the properties of the fibre-matrix interface on the transverse strength of the material. They go on to say that by tailoring the interfacial toughness, the strain to failure could be increased, resulting in the reduction of transverse matrix cracking and other damage mechanisms.

2.1.5 Section Summary

The authors [41,43,45,46] of the studies reviewed in this section make use of two-dimensional techniques to characterise damage initiation in CFRP, imaging damage at the surface of the material. This approach, although valuable, is limited as damage initiation is three-dimensional in nature. This highlights the need to use a three-dimensional technique. The studies reviewed here also acknowledge that in-situ testing and imaging are required in conjunction as when mechanical loading is released cracks close and their identification is made difficult. Where SRCT is used [3], the author images a single fibre to examine fibre matrix debonding. They were able to observe fibre matrix debonding and

crack kinking as the debond propagates along the fibre. This emphasises the potential of the technique to study damage initiation in CFRP although further work is required to study multiple fibre interaction. The work described in this thesis makes use of CT to scan composite material loaded *in-situ* and to capture volumetric scans of early stage damage initiation,

2.2 Computed Tomography

2.2.1 Introduction

Computed tomography (CT) was developed to overcome the limitations of 2D radiography as a medical diagnostic tool [54]. The usefulness of this technique was recognised and was adapted for use in other areas such as material science, archaeology and palaeontology to name a few [55-58]. As a result of the interest and development of system capabilities (resolution at high kV), as well as significant advances in computational performance, the availability of lab-based and synchrotron facilities have increased in the last four decades. CT has been used in a number of investigations on the quantification of damage in advanced composite materials [13, 14, 21, 59-63].

2.2.2 Computed Tomography Technique Description

Figure 2-13 is a schematic representation of the CT technique. The object of interest is placed on a rotation stage and a series of projections (i.e attenuation measurements) of a specific section, depending on the X-ray path, is captured for sequential increments of rotation [55].

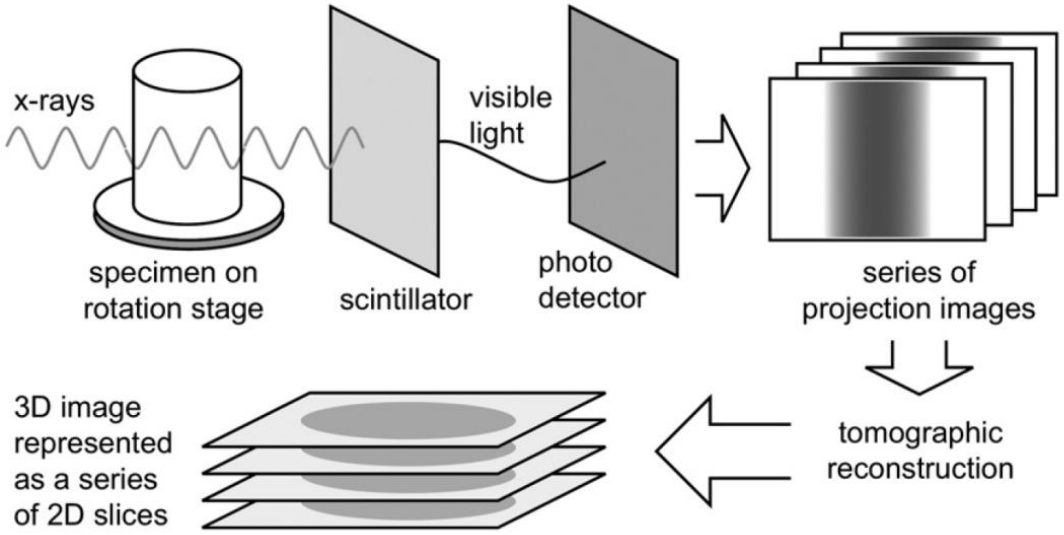

Figure 2-13: Schematisation of the CT technique from the X-rays passing through the specimen to reconstruction [54]

The object is typically rotated through an angle of 360° in a lab-based system and 180° in a synchrotron facility. The difference in the two techniques is the result of the beam geometry; a lab-based system employs a divergent cone beam and requires a 180° plus the cone angle view for complete angular coverage of all areas (centre to edge). Synchrotron facilities benefit from a parallel beam and so 180° rotation is optimal [64]. As the object is rotated, the attenuation of the

incident X-ray beam is measured for a finite number of angular increments. The optimal number of projections (number of projections to capture the area of interest in sufficient detail vs computing cost and increased noise) is dependent on the number of pixels the object obscures over the width of the detector and the reconstruction method; for example: $(\pi/2)n$ is typical for back projection, where n is the number of pixels [54]. The field of view depends on the required voxel resolution and the detector size. Contemporary detectors are typically ≈ 2000 x 2000 pixels; high resolution resulting in a small field of view [64]. The projections, represented as a line integral of attenuation along a path, are combined by reconstruction software using an inverse-Radon transform [55].

2.2.3 The Attenuation of X-rays in Materials

The basic principle of computed tomography (CT) is based on the measurement of the attenuation of X-ray photons due to the interaction with matter for different angular positions. An X-ray is an electromagnetic wave characterised by wavelengths in the picometer to nanometer range. Wavelengths in the range of 10 nm – 0.1 nm correspond to photon energy in the range of 124 eV – 12.4 keV, which are termed "soft" X-rays, whilst wavelengths in the range 0.1 nm – 0.01 nm relate to energy in the range of 12.4 keV – 124 keV, known as hard X-rays [54]. Hard X-rays are able to penetrate denser materials such as steel and nickel. The main modes of interaction between X-ray photons and matter when hard X-rays are used are: the photoelectric effect, the Compton effect and coherent scattering (Rayleigh scattering) [54]. The interaction, attenuation of X-ray photons, and consequently the percentage of energy transferred depends on the energy level used and the atomic number of the material (Z). In this work, moderate energy is used (<20keV) and as such the energy transferred after attenuation is largely due to the photoelectric effect for the low atomic numbers involved [65]. The effect of the interaction is captured by the detector and is used to produce a radiograph. The Beer-Lambert law, equation 1 is the simplest description of the intensity of the radiation after interaction and assumes a homogeneous material and that the radiation is monochromatic [55, 65].

1

$$I = I_0 e^{-\mu L}$$

Where I and I_0 are the transmitted and incident radiation respectively, μ is the linear attenuation coefficient of the material and L the thickness of the object. In this simple case the attenuation coefficient is defined as:

2

$$\mu = \frac{1}{L} ln \frac{I_0}{I}$$

Of course, real materials are not homogeneous and hence equation 1 must be amended to account for an inhomogeneous material:

3

$$I = I_0 e^{-(\mu_1 L_1 + \mu_2 L_2 + \mu_3 L_3 ..)} = I_0 e^{-(\sum_{i=1}^{n} \mu_i L_i)} = I_0 e^{-\int_0^L \mu_1 dL}$$

The attenuation (P) is given by:

4

$$P = ln\frac{I_0}{I} = \sum \mu_i L_i$$

where μ_i is unknown. A further modification to equation 3 accounts for the presence of polychromatic radiation with an inhomogeneous material. The coefficient of linear attenuation is also a function of energy; the equation becomes:

5

$$I = \int_0^{Emax} I_0(E) e^{-\int_0^L \mu(E) dL}$$

Due to the photoelectric effect, at the energy range considered, the linear attenuation coefficient μ is given by:

6

$$\mu(x, y, z) = K\rho\frac{Z^4}{E^3}$$

Where K is a constant, ρ is material density, Z is the material atomic number and E the energy of the incident photons [54].

2.2.4 Tomographic reconstruction

When a series of projections has been acquired, reconstruction of the distribution of linear attenuation coefficients must be undertaken [66]. Filtered back-projection (FBP) is the most commonly used reconstruction tool and most software associated with commercial micro-focus CT systems has this embedded within [55]. Figure 2-14 is a schematic representation of the back projection approach as described by Hsieh [65] in which a single focal spot is taken into account under the assumption that nothing is known about the object.

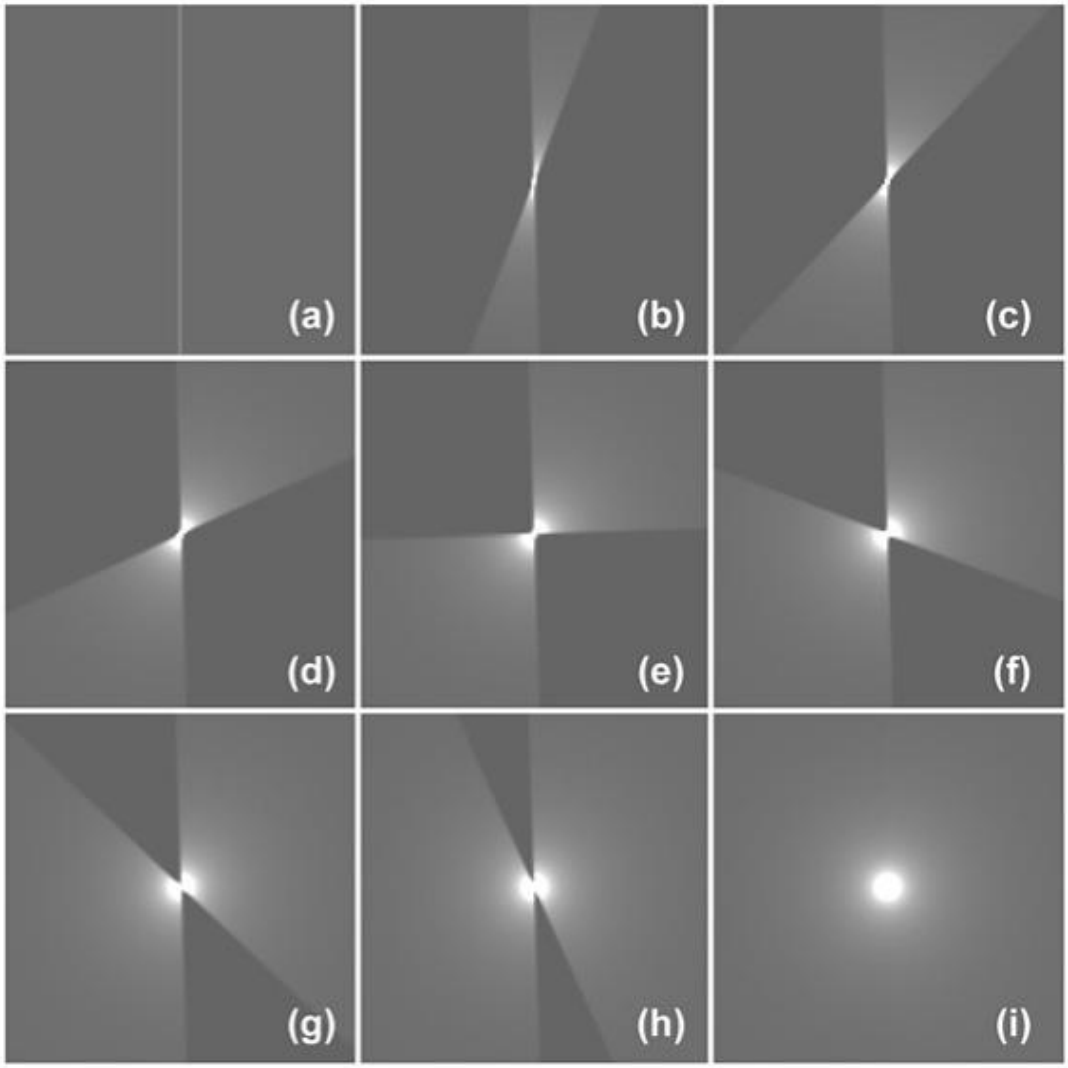

Figure 2-14: The back projection reconstruction method [61]

The first X-ray path, Figure 2-14(a), is not to determine where X-ray attenuation is located along the line. Projections captured at different angular positions are required to provide further information to localise the position of the attenuating point, Figure 2-14 (b - i). In this specific case each projection is represented by an impulse function with the peak centred in at the location where the X-rays intersect the object. The algorithm reverses the projections, hence the name "back-projection", resulting in the two-dimensional representation, Figure 2-14(i). Although the final position of the object has been identified, the back-projection yields a blurred representation, Sources of blurring include the size of the sampling aperture (which can be regulated by the focal spot size and the detector size), the size of the voxels, the number of projections and the reconstruction filter selected. Noise is caused by the variation in material attenuation coefficients between voxels. The blurring can be understood by the profile of the reconstructed point, Figure 2-15. The black line represents the back-projection of the object, while the actual object is the grey line [65].

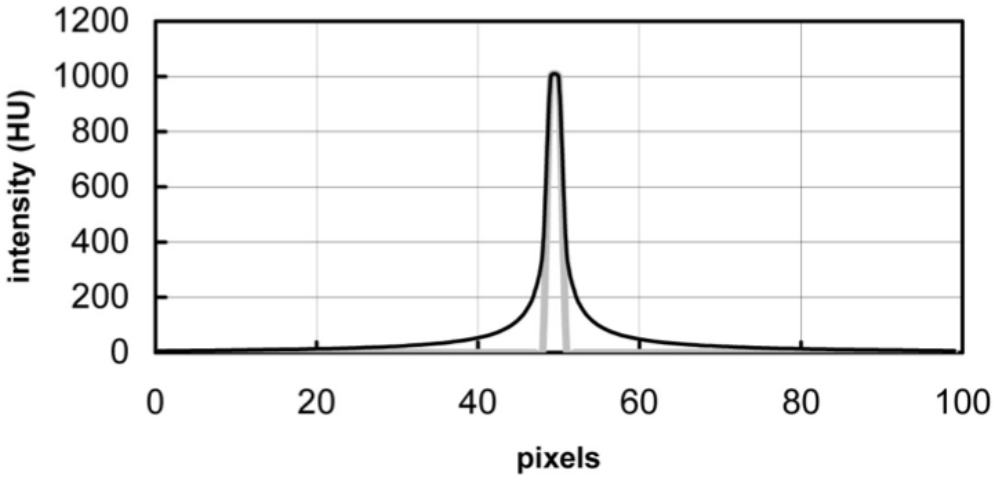

Figure 2-15: Explanation of the blurring that occurs when using the back-projection technique [61]

Since the final representation, Figure 2-14(i), is the impulse response of the back-projection method, it is possible to obtain a more accurate representation of the original object by the deconvolution of the back-projections with the inverse of the impulse response [65]. This process is known as filtered back projection (in which a high pass filter is applied during reconstruction). Figure 2-16 a-e is an example of the filter back projection method and a comparison with standard back projection Figure 2-16 f.

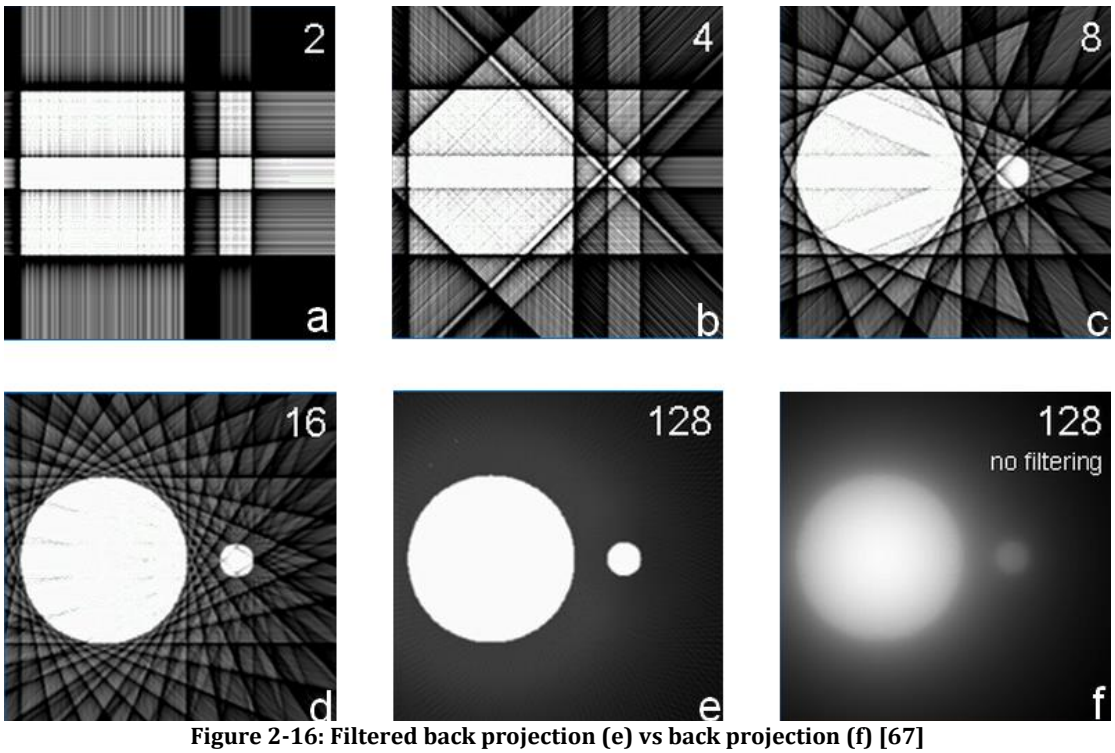

Figure 2-16: Filtered back projection (e) vs back projection (f) [67]

2.2.5 Artefacts

A greyscale representation of the coefficient of linear attenuation is typically used for reconstructed CT volumes. There are a number of factors which could inhibit this process resulting in an image that differs from the original object.

These potential sources of error, referred to as artefacts, have different consequences and solutions [54, 55, 65, 66]. Artefacts appear as distortions of the image that affect the overall image quality which can ultimately compromise the information contained. The presence of artefacts can introduce significant errors when the data captured by CT is used for quantification. Common artefacts include [55, 65]:

- Beam-hardening; associated with a polychromatic X-ray spectrum and with the energy dependence of the attenuation coefficient. When a polychromatic source is used, most materials absorb X-rays at lower energy easily (due to photoelectric absorption), and this determines a change in the energy spectrum that causes beam-hardening artefacts. These artefacts are not typical of synchrotron sources, where monochromatic radiation is used. Beam hardening can cause streaking artefacts, cupping or shading on the reconstructed images.

- Ring artefacts; due to the presence of individual mis-calibrated or defective pixel elements in the detector, ring artefacts appear as concentric dark or bright rings centered on the rotation axis.

- Motion artefacts; are due to movements that can occur during the scan or the setup of the scanner. The misalignment between the centre of rotation of the specimen and the stage causes blurring such as double images and crescent streaks.

Specific software used in the post-processing can correct some of these artefacts, however, not all artefacts can be avoided and/ or corrected (e.g. motion artefacts) [66].

2.2.6 Phase Contrast

Phase contrast exploits the fact that the X-ray beam is not only absorbed when it penetrates matter but that the phase of the wave is affected [68]. Unlike absorption, phase changes do not influence the wave amplitude of the beam and thus cannot be measured directly behind the sample. The image is created by the interference of the diffracted components of the beam with itself and the non-diffracted parts of the beam, Figure 2-17.

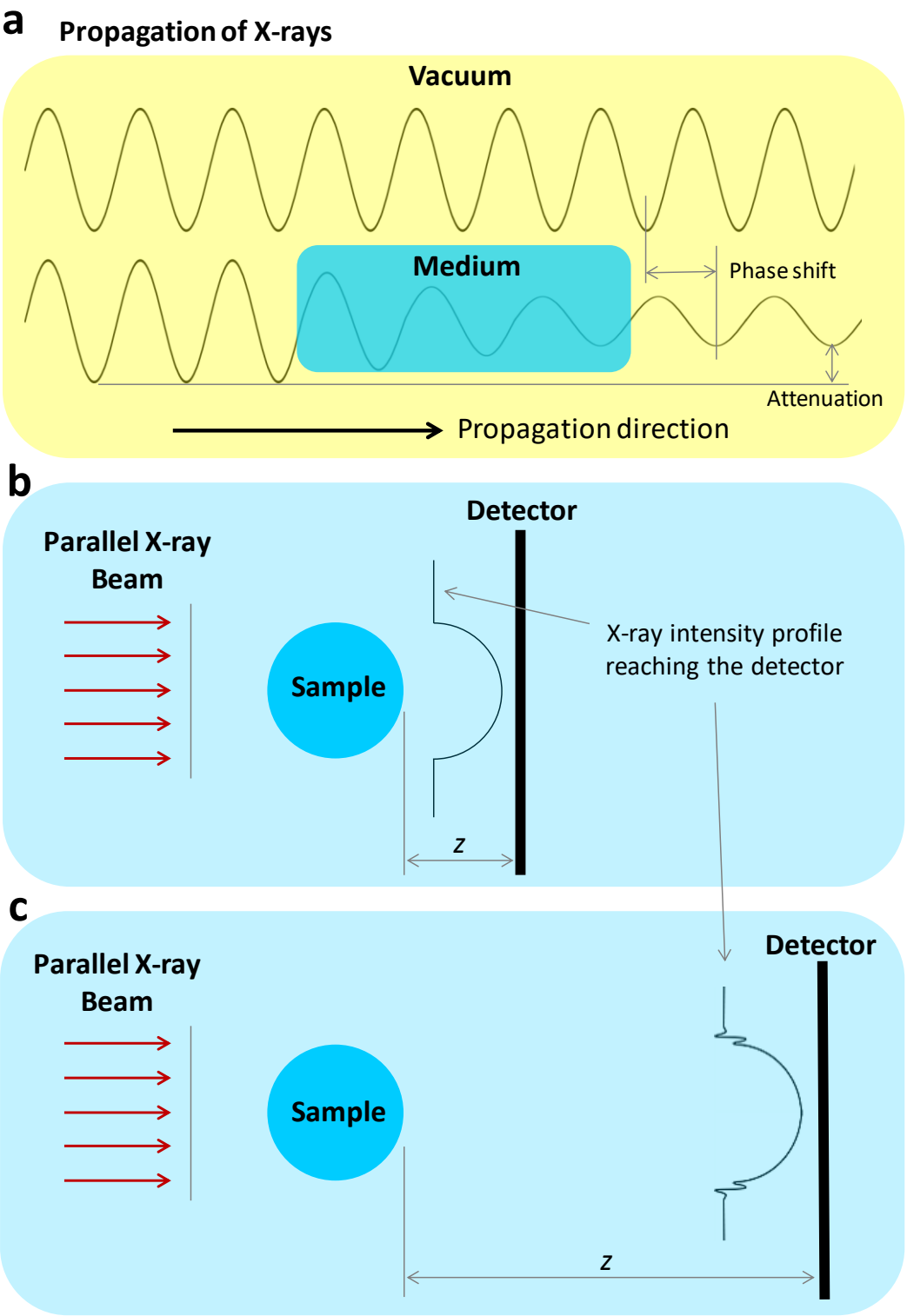

Figure 2-17: Schematic depicting the basic priciple of phase contrast imaging [64]

At the detection plane, these interactions are expressed in lateral intensity variations. The greatest advantage of phase-contrast imaging (not used in this work) is that it creates greater contrast between low Z (the material atomic number) phases, with minimal radiation dose on the sample, this creates edge-enhancement effects. Since phase contrast imaging requires a homogeneous X-ray beam with spatial coherence, synchrotron radiation is particularly well suited for this technique [68].

2.2.7 Synchrotron Radiation Computed Tomography

Two X-ray sources are commonly used to produce X-rays for scientific micro CT applications: lab sources, referred to as micro-focus CT, and synchrotron radiation computed tomography (SRCT) [55]. The latter technique is primarily used in the present study; the quicker scan time associated with SRCT (minutes vs hours) means that issues such as stress relaxation and the associated motion artefacts are reduced.

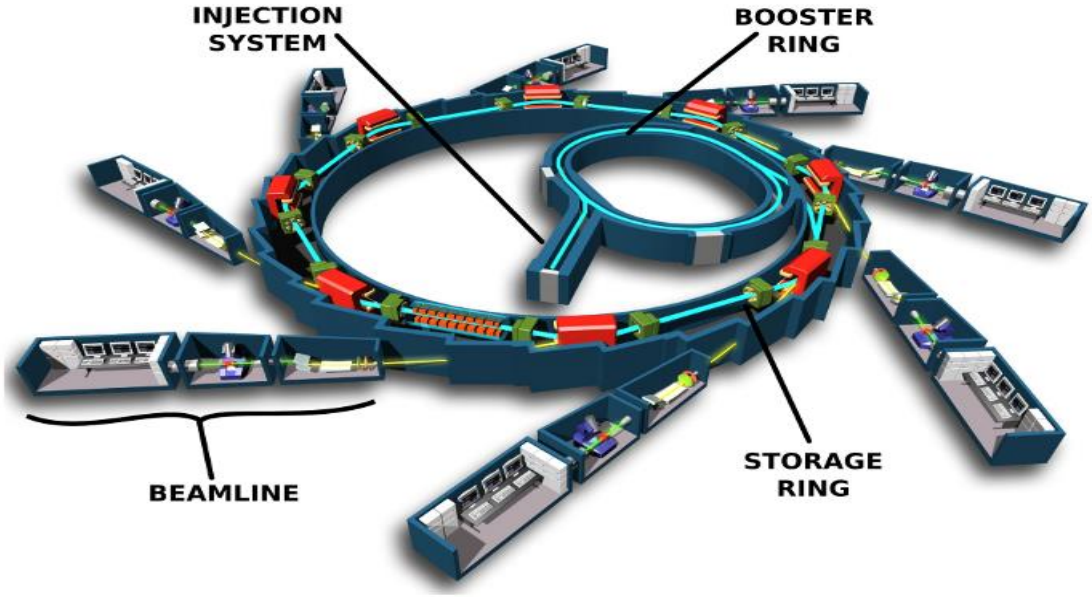

Figure 2-18: The main components of a Synchrotron [69]

The typical contemporary synchrotron is comprised of three main parts, as shown in Figure 2-18: a linear accelerator (known as the linac) where the electrons are pre-accelerated to an intermediate energy of ~100 MeV [68], a circular accelerator (known as the booster) where the electrons coming from the linac are further accelerated up to ~2.4 GeV [68]. The electrons in this final energy stage have a speed of close to the speed of light. The electrons from the booster are periodically injected into the storage ring keeping the current constant. Electrons in the storage ring circulate for many hours generating X-rays via the various bending magnets and insertion devices present. A high vacuum system allows the beam to circulate for ~10h with only small losses, by reducing the frequency of collisions of electrons with other particles [64]. The electrons are forced to follow a circular path within the storage ring due to the presence of bending magnets. They are accelerated along an orbital trajectory within the storage ring by the bending magnets. The consequence of the acceleration of the electrons (represented in blue) being forced along the circular path is the emission of a continuous spectrum of synchrotron light (represented in yellow).

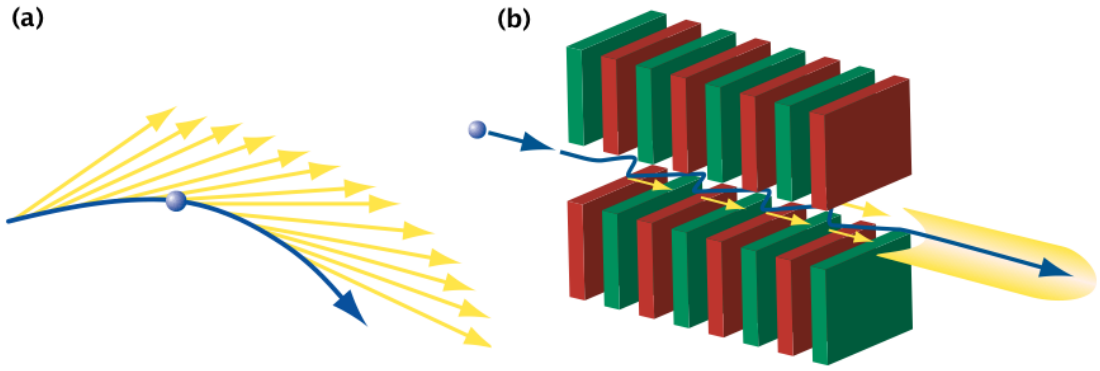

Figure 2-19: Insertion devices used at the Synchrotron [69]

Third generation light sources; such as the Swiss Light Source (SLS) and the European Synchrotron Research Facility (ESRF) use insertion devices (typically 'undulators' and 'wigglers') to generate the desired X-ray beam for a given experiment type. Insertion devices, Figure 2-19, can be thought of as many magnetic beam deflectors installed next to each other [70]. A very narrow cone beam and an increase of intensity/ brightness of roughly 1000 times the intensity of radiation due to the curvature of the storage ring is the result [64].

2.2.8 Advantages of Using SRCT

Substantial differences in terms of image quality (spatial resolution, signal to noise, beam hardening) and acquisition time (temporal resolution) exist between the use of laboratory sources and synchrotron sources. The beam achievable using a laboratory device is typically polychromatic and divergent (cone beam), while the beam generated by a synchrotron source is parallel, monochromatic, coherent and orders of magnitude brighter, Figure 2-20 [70].

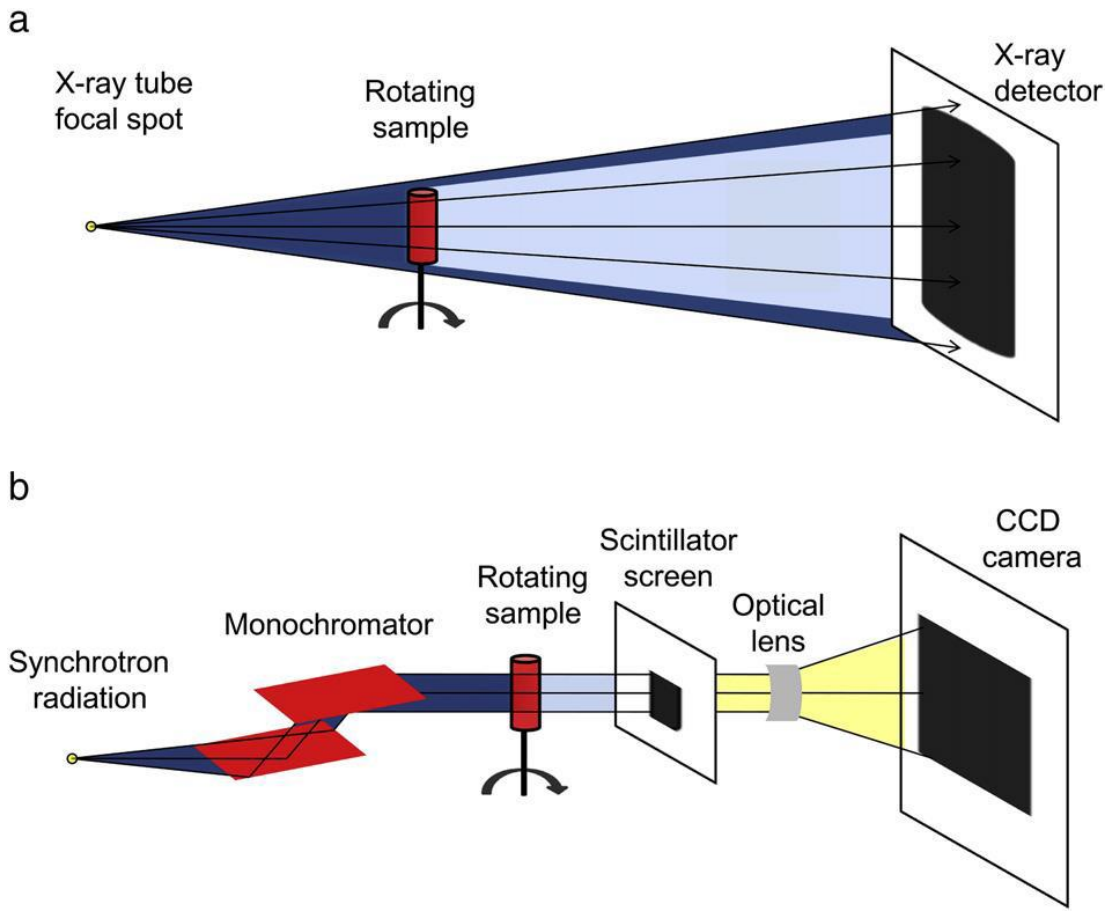

Figure 2-20: Conical beam at a lab based CT system compared to the parallel beam at a synchrotron [69]

The advantages associated with synchrotron radiation computed tomography are:

- High spatial resolution (the result of a high brightness source) which allows phenomena such as crack nucleation and resolving narrow damage to be examined.
- High temporal resolution, which is fundamental for in situ experiments.
- Enhancement of the signal to noise ratio due to the available flux.
- Phase-contrast

Modern laboratory-based CT systems can achieve comparable spatial resolutions to synchrotron sources in the order of one micrometre and below. However, the signal to noise ratio and scan duration remains high compared to synchrotron facilities [70].

2.2.9 Section summary

The signal to noise ratio and scan duration advantages that SRCT has over laboratory-based CT systems justify the use of the technique in this work as the likelihood of movement artefacts associated with stress relaxation (among others) are minimised. The chosen scan resolution (650 nm) allows enough detail in the images but is large enough to maximise chances of capturing crack initiation.

2.3 Digital Volume Correlation

2.3.1 Introduction

Stress, strain and second order tensors vary over complex geometries; meaning that although reasonably accurate, traditional tools such as strain gauges can only describe the strain state at a few discrete points, (for the components of strain parallel to the surface). The ability to measure full-field strains in order to verify predictions experimentally is a potentially key step in failure model validation. Improvements in modelling tools, such as FEA, have meant that the capability to predict has outgrown the ability to verify [17]. Early methods of full field measurement, such as photoelasticity made valuable contributions to the field but were ultimately limited in use by practical limitations, eg: a) requires that a model of the actual part be made (unless photo elastic coatings are used), b) requires rather tedious calculations in order to separate the values of principal stresses at a general interior point, c) is time-consuming for three-dimensional work and d) data processing limitations [17].

Advances in computing power and the introduction of digital imaging in the 1970's allowed the emergence of digital image correlation (DIC) which has since grown into an established and refined measuring tool [32, 71]. The technique involves applying a speckle pattern to the surface of an area of interest and capturing digital images as the loading and subsequent deformation takes place. The deformed images are compared to the initial unloaded image and the resulting displacements are mapped. The technique is limited in its application to surface strain measurements on relatively flat surfaces as speckle application and lighting are inconsistent on uneven surfaces. It is possible in a number of situations to use the naturally occurring texture of the material as a basis for image correlation [72]. This process, termed texture correlation (TC) has for example been applied to investigations on trabecular bone loaded in plane [73-76].

The growth in the availability of high-resolution X-ray computed tomography has allowed researchers to investigate intricate internal material microstructures with a view to understanding material morphology and relating that to macroscopic material properties, and to the development of intensive finite element analysis based on direct micro architectural models [16, 77]. When considered in the context of surface strain mapping and texture correlation, further applications of the volumetric data became evident. Image and texture correlation essentially use images captured before and after manipulation of the material under investigation has occurred, to track the displacements of small regions of interest. DIC and TC use a speckle pattern or material texture to map the displacements at the surface, and while a speckle pattern is generally not present within the interior of a material, texture often is [72]. Recent work by Schoberl *et al [78]*, show that by applying a metallic powder to the matrix material of CFRP, a speckle pattern can be introduced to the interior.

The digital volume correlation (DVC) process is the extension of area pixel subsets into volume voxel subsets (subvolumes). Figure 2-21 highlights the

difference between the pixel and the voxel. DVC software tracks displacements of the subvolumes with correlation procedures if an appropriate material texture is present. True three-dimensional displacement and strain mapping of the interior of a sample under load is possible [17].

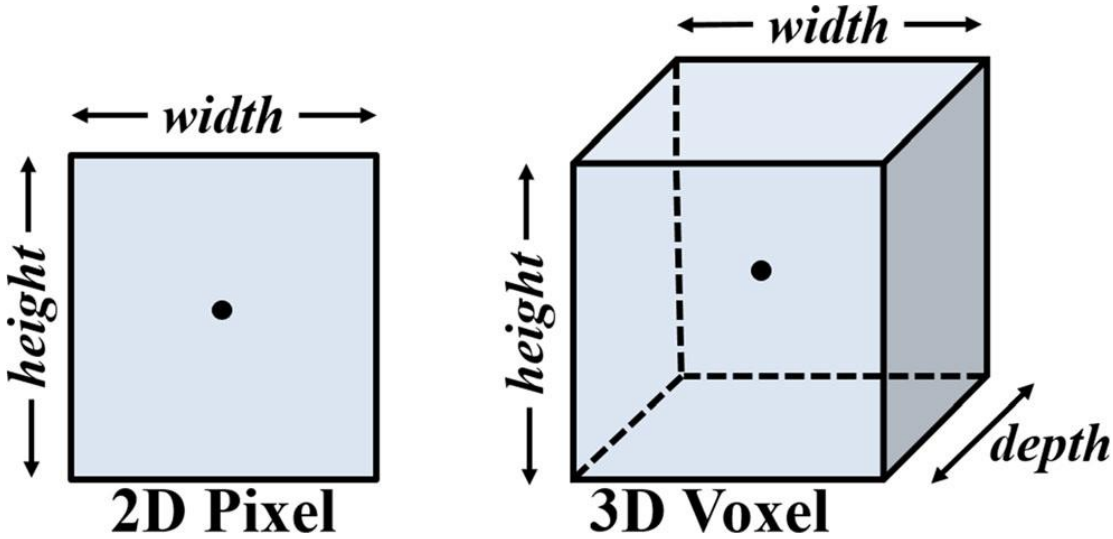

Figure 2-21: The pixel vs the voxel [17]

Initially introduced in 1999 as a means to measure continuum-level displacement in trabecular bone, DVC has seen a number of technical refinements and an increase in its application [17]. Initial work by Bay *et al* [17, 18] followed the methods of DIC in which an objective function is used to track displacements in regions of image data. Very simple objective functions were used due to the available computing power and large volumetric datasets [18]. This resulted in limiting degrees of freedom to the three components of displacement. The search algorithm used initially was also taken from DIC; starting point determination, a coarse – fine search strategy and cubic spline interpolation for subvoxel precision. More recent work has focussed on technique development, measurement accuracy quantification and adaptation to specific applications. The addition of rotational degrees of freedom [79] improves accuracy when local subvolume rotations occur during sample loading. Algorithms have been further adapted to include uniform subvolume strains [80]. This progression from displacement only to displacement-rotation-strain increases the parameter space from three to twelve making the technique more resource intensive but more informative (potentially). Using frequency domain approaches to correlation can offset the additional cost, although spatial domain processing remains the preferred method of choice for comparison accuracy [81].

2.3.2 Technique description

Variations of the DVC technique exist, although the framework on which it is built is consistent [81]. The global spatial domain is made up of a number of voxels rendered for visual display but in reality, is a three-dimensional array of discrete values representing material-energy interaction averaged over a voxel. DVC uses the voxel value by associating it with a discrete point at its centre and

the values between the points are estimated using an approximation scheme. The DVC process starts with choosing a region of interest over which displacement values are required. The correlation of a reference image volume with a deformed image volume is the next and most critical step in calculating the displacement vector [17].

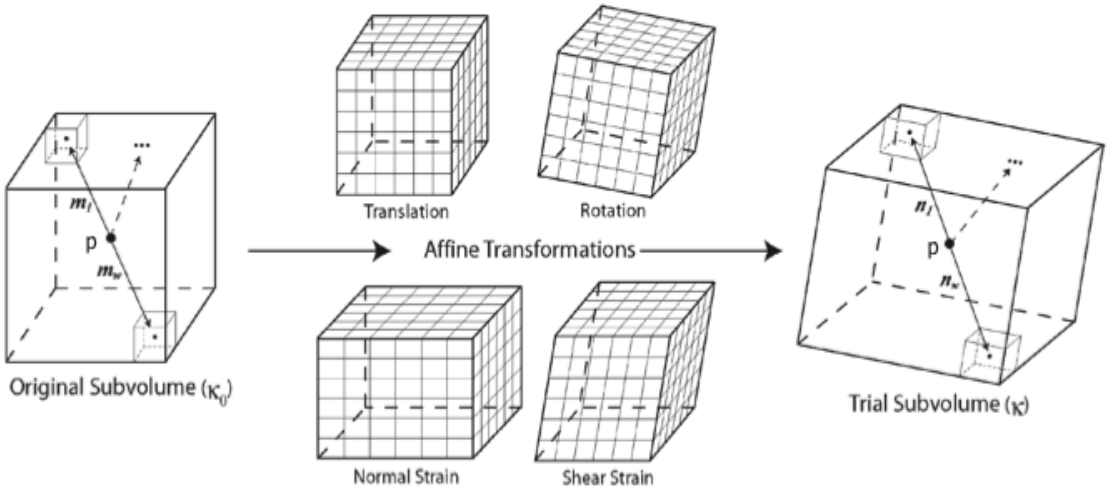

Figure 2-22: Shape functions used to determine displacement vectors [17]

Figure 2-22 illustrates the process for analysing a point P. A cubic subvolume of voxels, k_0, whose centre, the point P, is extracted from the reference volume [17].

The typically cubic subvolume, is defined as a set of ω vectors centred at the measurement location, typically the voxel centre, and pointing to the centre of each subvolume element, $\{m^{\alpha} : \alpha = 1, 2, 3, 4 \ldots., \omega\}$. Values of each voxel within a subvolume, at the location of the m vectors, are determined from the reference volume. The correlation process involves subjecting the original subvolume k_0 to affine transformations (known as the shape function) [17], in order to determine the deformation required to best map the displacements between reference and deformed volumes, producing a trial subvolume, k. This trial subvolume is also defined as a set of ω vectors, $\{n^{\alpha} : \alpha = 1, 2, 3, 4 \ldots., \omega\}$, whose values are extracted from the deformed volume [17]. Translation is the primary transformation of interest, providing an estimate of displacement vector "t". Rotation, normal strain and shear strain are used to improve correlation accuracy when the associated modes are significant over the subvolume. The advantage of defining the above transformation as affine is that they can be selected or deselected from the correlation process in any order to manage computation time and the minimization process, important as each transformation adds three degrees of freedom [17]. The definition of an objective function used to determine the degree of match between subvolumes k_0 and k is the next stage of the DVC process. The sum-of-squares correlation coefficient (SSCC) is a typical approach [17]:

7

$$C(g) = \frac{1}{2}\sum_{\propto=1}^{\omega}[B(p + x^{\propto}) - A(p + m^{\propto})]^2$$

where $x^{\propto} = t + n^{\propto}$
A and B represent the reference volume and the target volume respectively. Vector g contains the active degrees of freedom for the problem: displacements that define t, the rotation and the strain parameters that define the affine transformations of the subvolume.

When the image volume does not exhibit substantial brightness and/or contrast differences, sum of square correlation offers a good compromise between correlation accuracy and computational burden. A normalised cross-correlation coefficient (NCCC), equation 8, is more appropriate when the aforementioned conditions are not met [17].

8

$$C(g) = 1 - \frac{\sum_{\propto=1}^{\omega} B(p + x^{\propto})\ A(p + m^{\propto})}{\sum_{\propto=1}^{\omega} A(p + m^{\propto})^2\ \sum_{\propto=1}^{\omega} B(p + x^{\propto})^2}$$

The normalized coefficient makes the monitoring of the convergence process and the detection of failed minimisations easier.

where $x^{\propto} = t + n^{\propto}$

In order to estimate the displacement vector t at the point p the global minimum of the function C with respect to g must be found. Bay *et al* [17] describe an effective three-stage process. The procedure begins with an initial estimate for the displacement determined from information from points that have been successfully located. This is known as the starting point specification. A coarse search, with translation-only degrees of-freedom active is then undertaken as the second stage with steps limited to integer voxels.

In order to prevent entrapment in local minima a global search over a reasonable domain is best. Subvoxel gradient-based minimisation with all degrees-of-freedom active is the final stage [17]. As in DIC, the minimization algorithm is performed to evaluate internal displacement field by minimising the image intensity difference in small subsets between the undeformed and deformed images [82].

Interpolation is required in order to estimate image data between voxel locations since the n vectors will typically not point to voxel centres as a result of the affine transformations resulting in subvoxel deformations [83]. The minimisation process is carefully monitored in order to flag points at which special handling is required as a result of a failure to meet some convergence criteria or that converge to physically unrealistic displacement values [17].

Strains are estimated at all measurement locations from the displacement vector field. A least squares fit to a second-order Taylor series expansion may be used to estimate the strain tensor at each point “p” from a cloud of neighbouring points [17].

Carefully chosen DVC parameters must be implemented in order to ensure accuracy and the resolution of strain gradients. Subvolume size, correlation grid spacing and shape function must be chosen carefully. The underlying deformation being investigated and image pattern, e.g., size and density of speckles, image contrast and noise, influence the choice of parameters [83].

2.3.3 The influence of choice of parameters and DVC accuracy

DIC has been widely studied and has developed into a reliable and repeatable measurement tool in the mechanics community [32, 71, 84-86]. The parameters that ensure the accuracy and precision of DIC, have been studied, refined and well documented [32, 71, 84-88]. Due to the more recent emergence of DVC, the technique and the influence of the choice of parameters has not received the scrutiny that DIC has [89]. Many of the results determined for DIC are applicable to DVC, however issues specific to DVC such as scaling and image noise need more attention to better understand their influence [89].

2.3.4 Influence of subvolume size.

Possibly the most influential parameter in terms of measurement precision, it is essential that the selected subvolume size be large enough so that during the correlation process, there is a sufficiently unique intensity pattern, which can be distinguished from other subvolumes [83]. Jandejsek *et al* [90] determined that above a certain subvolume size, significant improvements in displacement measurement where not observed but that spatial resolution of strain decreases. Smaller subsets, however, resulted in larger displacement measurement errors and higher spatial resolution.

2.3.5 Influence of subvolume grid spacing

Considering correlation grid spacing, it is common practice to overlap subsets by half the subset size, so a subset of 61 voxels, for example, yields a grid spacing of 30 voxels between correlation points [80, 91, 92]. The computational cost of DVC with a subvolume size s, grid spacing h and region size R is $O(8R^3)$ where $O = s\,h$. The factor 8 occurs because, with the exception of voxels near the region boundary, every voxel is part of 8 overlapping subvolumes. Strain gradients that occur over a small region require a sufficient number of samples, meaning smaller correlation grid spacing. The cost of DVC grows cubically with the inverse of grid spacing [82] when a fixed subset size is used.

2.3.6 Influence of Correlation Coefficient Function

Smith *et al* [79] compared the measurement accuracy of two correlation coefficients namely SSCC and NCCC. They found that the NCCC provided consistently more accurate displacements throughout the range of rotations applied to each sample. Although more computationally expensive than SSCC, the NCCC algorithm produced an error fifty times smaller than SSCC when applied to low contrast images. Liu and Morgan [20] report lower error in displacement using a SSCC algorithm, which they identified as the maximum likelihood

estimation (MLE), when compared to NCCC and cross correlation (CC) techniques. The MLE algorithm represents a global approach to DVC, which has been shown to reduce displacement error compared with local techniques. Continuity requirements are imposed so that mapping a single subset depends on the mapping of adjacent regions. Aberrant displacement measurements are minimised using this approach, when compared with algorithms that map subsets independently, as is the case with local approaches [84]. With subset based DVC algorithms, SSCC is less computationally expensive but is identified as less accurate than NCCC in particular when images exhibit low grey levels [83].

2.3.7 Influence of shape function

It was observed in early work by Smith *et al* [79] that when non-translational deformation such as rigid body rotations are present within the volume of interest, errors in accuracy and precision of displacement measurement are relatively high when a three degree of freedom shape function is used in DVC when compared to algorithms using the additional affine transformations (rotation, normal strain and shear strain). When a 15° uniaxial rotation about the z-axis was applied, Smith *et al*, reported a displacement accuracy of 3.328 voxels using only translational transformations, while adding the additional rotational degrees of freedom resulted in displacements with an accuracy of 0.0057 voxels. The additional DOF are computationally expensive but mean that accuracy and precision are improved.

2.3.8 Influence of image voxel size and sample microstructure

Verhulp *et al* [93] studied the influence of voxel size of error in DVC. They utilised a subvolume of constant size (250 x 250 x 250 μm^3) and increased the voxel size from 12 to 20 and then to 36 μm. The results of their study showed that an increase in voxel size had little effect and recorded an increase in the error of less that 1 μm. Liu and Morgan [20] reported similar findings when they studied the effect of a change of voxel size stating that changes in voxel size at high resolution has minimal effect on error values. Conversely, imaging structures at low spatial resolutions may introduce errors due to the inability to accurately resolve small internal features [94]. Liu and Morgan [20], show in a study on trabecular bone that size, volume and spacing of the porosity used to track displacements influences the accuracy of the measurement. They observe that the greater the number of well-spaced features greatly improves the strain accuracy error.

2.3.9 Influence of parameters on error

There have been several studies examining the relationship between error, subset size, shape function and image pattern for DIC [71, 84, 85, 87, 88]. Wang and co-workers [95] derive an estimate for the standard deviation of error in displacement, which suggests that by increasing the subset size, the standard deviation of the error is reduced. It is to be assumed from their work that a good distribution of speckles in the image, good image contrast and low image noise has been accounted for. Estimates described in [71] and [85] reinforce the concept that increasing the subset size reduces the standard deviation of the

error, assuming the shape function accurately represents the displacement. When the underlying displacement does not match the shape function, DIC measures a systematic bias error, as described in [85]. They derive an equation to calculate the bias error measured when a linear shape function is used to fit a quadratic displacement field. The implication of their work is that smaller subsets are required to achieve accurate DIC results when using linear shape functions. When a quadratic shape function is used, the bias error is eliminated since it can fit the quadratic displacement field. The shape function is a Taylor approximation to the displacement field; so a quadratic shape function fits a general displacement field more accurately than a linear shape function [85]. The extra quadratic term allows for more flexibility in matching displacement but means that the standard deviation is also larger. In a linear field, for instance, all quadratic terms should be zero, but experimental noise will be a small, but non-zero value, which in turn introduces more variability into the results.

When considering standard deviation, bias error and the cost of grid refinement together, there is no optimal combination of subset size, grid spacing and shape function even for a single image [82]. To reduce computational noise and cost, in regions of linear strain, it is preferable to use a large subvolume and a correspondingly large grid spacing with linear shape function, while a smaller grid spacing and smaller subvolumes or a quadratic shape function are required to measure accurately the displacements where strain is changing over the region of interest (e.g., a quadratic displacement field).

2.3.10 Measurement Uncertainty Quantification

Where finite element modelling can often be verified against experimental work, and vice versa, there is limited opportunity to accomplish this verification with DVC due to the unavailability of alternative techniques to measure internal strains [81]. As has been demonstrated there are a number parameter choices that can affect error, other factors such as mechanical and electrical noise of the imaging system, scanning parameters and the choice of CT reconstruction algorithm can add additional levels of uncertainty.

The quantification of individual errors occurring from system noise, scanning parameters and correlation strategies in DVC is potentially complicated and time consuming. It is however important to understand the measurement uncertainty of the system in order to validate and expand on findings [81]. Roberts et at [83] quantify measurement errors in DVC by considering the parameters chosen to affect the strain measurements. The authors of a number of studies [19, 20, 96-98], recommend that the strain uncertainties be calculated by comparing repeat scans of an unloaded specimen (i.e zero displacement should be recorded by the system) and measure the standard deviation of the strain over a range of subvolume sizes to determine system noise and to optimise subvolume size. Madi *et al* [25] virtually displaced the volume of interest and use the DVC software to track and return a value, which can be compared with the known displacement.

Palanca *et al* [81] recognised, in their work, that different correlation and strain calculations (i.e local vs global approaches) employed in DVC software will yield different uncertainty values and argue that it is important to compare two or more methodologies using the same image dataset when attempting to quantify these uncertainties. Their study compared three approaches. Both DVC strategies, fast fourier transform (DaVis-FFT) and direct coupling (DaVis-DC), offered by the commercial DaVis 8.2.1 code (LaVision Ltd., Goettingen, Germany) are interrogated against a in house software – ShIRT-FE. DaVis-FFT and DaVis-DC both employ a piecewise linear shape function and a normalised cross-correlation coefficient. The main difference between Davis-FFT and DaVis-DC is the interpolation calculation: DaVis-FFT using trilinear interpolation, whereas DaVis-DC makes use of a third-order spline. Both processes compute the three-dimensional displacement field using a multipass approach that allows subvoxel precision. The multipass approach is also known as a predictor-corrector and uses decreasing subvolume sizes and an intensity interpolation Gaussian algorithm fitted to the correlation peak to calculate displacements from the predictor step to be used to inform the corrector step. This process is iterated as the subvolume size decreases to its final defined size. From the resultant displacement vectors at each subvolume centre, the strain field is computed using a centred finite difference (CFD) scheme.

ShIRT-FE combines an elastic registration software with a finite element simulation [96]. An homogenous cubic grid with a certain nodal spacing (subvolume) is superimposed to the images to be compared in order to recognise identical features between the volumes. Nodal displacements that map each point in the first image into the second image are computed by the software solving equations in the nodes of the grid [96].

The first step in their study was to investigate and compare the influence of the subvolume size on the different approaches. Subvoxel sizes between 5 and 50 voxels were used. The metrics used to quantify the accuracy and precisions of the approaches were: Scalar comparison and comparison by component. Scalar comparison makes use of the average and standard deviation of the average of the absolute values of the six strain components to quantify accuracy and precision. Comparison by component is used to investigate the presence of preferential strain in the algorithms; accuracy and precision were reported for each strain component. The trends were analysed, plotting the errors as a function of subvolume sizes. Computational costs were also included in their evaluation.

The results of their study show that while computing displacements were highly accurate and precise, larger errors were found in the computed strain distributions, although these errors decreased with larger subvolumes. The integration of DVC with an FE code (which imposes a continuum mechanics assumption on the structure) provided the most accurate and precise results. The DaVis software performed well as a single software package. The errors from the repeated static scan study were similar for the different components for all three methods. They conclude by reminding the reader that a sufficiently large subvolume should be used to achieve reasonable accuracy and precision

and that further work should be conducted to determine the influence of imaging techniques and microstructure.

2.3.11 The use of DIC and DVC techniques on Fibre Reinforced Polymers

Digital image correlation has been used in a number of studies to investigate damage mechanisms in composite materials e.g. [32, 38].

(DIC) has been used in a study to determine the strains in an unidirectional glass fibre laminate loaded in compression. Canal *et al* [32] used DIC in conjunction with *in situ* testing using a scanning electron microscope (SEM) to observe the response of the laminate to loading at 250x, 2000x and 6000x magnification. The low magnification study was conducted to evaluate the strain response of the material as a whole. The higher magnification was used to assess the strains at the fibre matrix interface and to compare the results to modelling. The fibres themselves were used as the reference pattern used to track displacements in the lower magnification study and an alumina powder was applied to the surface for the high magnification setting. Once they had determined an appropriate subset and strain window size, they applied the DIC technique to the captured scans.

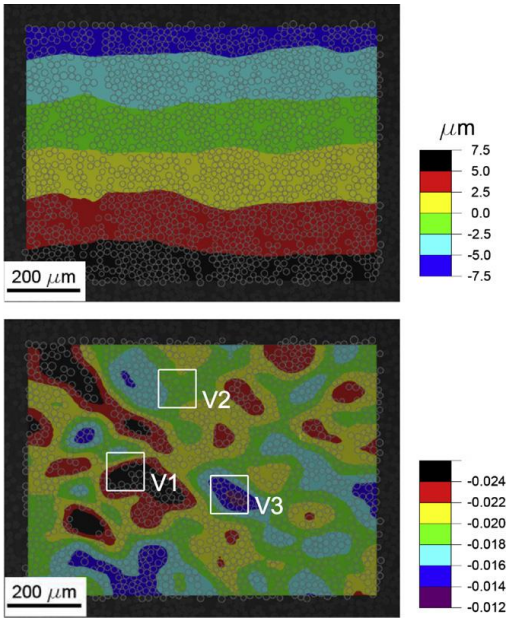

Figure 2-23: DIC displacement and strain in glass fibre reinforced polymer loaded in compression

At low magnification they were able to observe the material response to loading as seen in Figure 2-23 and demonstrated that the largest compressive strains (shown in black) were located at matrix rich regions. The pattern of the strains is of particular interest as the strain state changes quite noticeably between regions adjacent to each other. As well as being able to identify strain regions, an average of the strains across the entire area yielded a value within the expected range for the material in compression. They use the DIC images to validate a cohesive zone modelling technique (the strain maps of each technique showed

good agreement) and were able to extract strain data at the fibre matrix interface.

Literature on the DVC technique as applied to composite materials is less extensive, however two papers were found that have relevance to this work.

Firstly Lecomte-Grosbas *et al* [21] used DVC to investigate free-edge effects in laminate composites. They acknowledged that a complicated three-dimensional stress state exists at the edge of the laminate. Property mismatches lead to early delamination at the material edge and can speed up failure. Lecomte-Grobas used volumes captured using X-ray computed tomography at a resolution of 4.5 μm to compare the loaded and unloaded strain states using DIC and DVC. The two techniques were shown to have comparable results and were able to identify strains corresponding to irreversible deformation of the material at the edge. The cracks at the interlaminar interface that initially developed as a result of loading were found using optical microscopy to be on the order of 0.5 μm which is far below the resolution of the CT system used. Regardless of this both the DVC and DIC techniques were able to track the progression of damage as the crack opened. The DVC technique allowed the author to track the interlaminar delamination from the free edge to the interior. This paper highlights the usefulness of the DVC technique in its ability to track internal delamination. It also demonstrates the limitation of the technique, as there is a reliance on the resolution of the CT system used.

Borstnar *et al* [16] used DVC to determine the strains ahead of mode I delamination tips and to assess the accuracy and validity of the DVC technique. Scans were conducted using Synchrotron Radiation Computed Tomography (SRCT) at a 325 nm resolution. The testing took place *in situ*, Figure 2-24 is a schematic of the coupon under mode I loading.

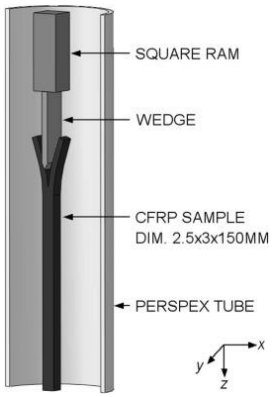

Figure 2-24: *In situ* mode I loading [16]

The first objective of the study was to determine the strain resolution and optimal sub-volume parameters. Two scans of the stationary coupon were captured followed by scans in which a pre-determined displacement was applied. Under ideal conditions a comparison of the two stationary scans should yield a displacement of zero. The effects of systematic noise or artefacts can be misinterpreted as strain measurements and so the comparison between the two

scans is used to determine the strain resolution. Strain measurements above this value can be considered the result of material/test behaviour. The scans captured after the displacements were applied were used to determine the accuracy of the displacement measurements. The known displacement was compared with the measurement achieved by the software. DVC was performed using DaVis 8.1.3 software via a proprietary Fast Fourier Transform (FFT) approach with a 50% overlap between neighbouring sub-volumes.

In order to assess the error brought about by noise, Borstnar calculated the standard deviations of all the measured strain components within the volume and recorded the normal distribution with a mean of zero. In so doing all stochastic noise in the imaging system and biases in the correlation algorithm are captured. Figure 2-25 was produced by the author to illustrate the influence of changing the sub-volume size on the strain resolution.

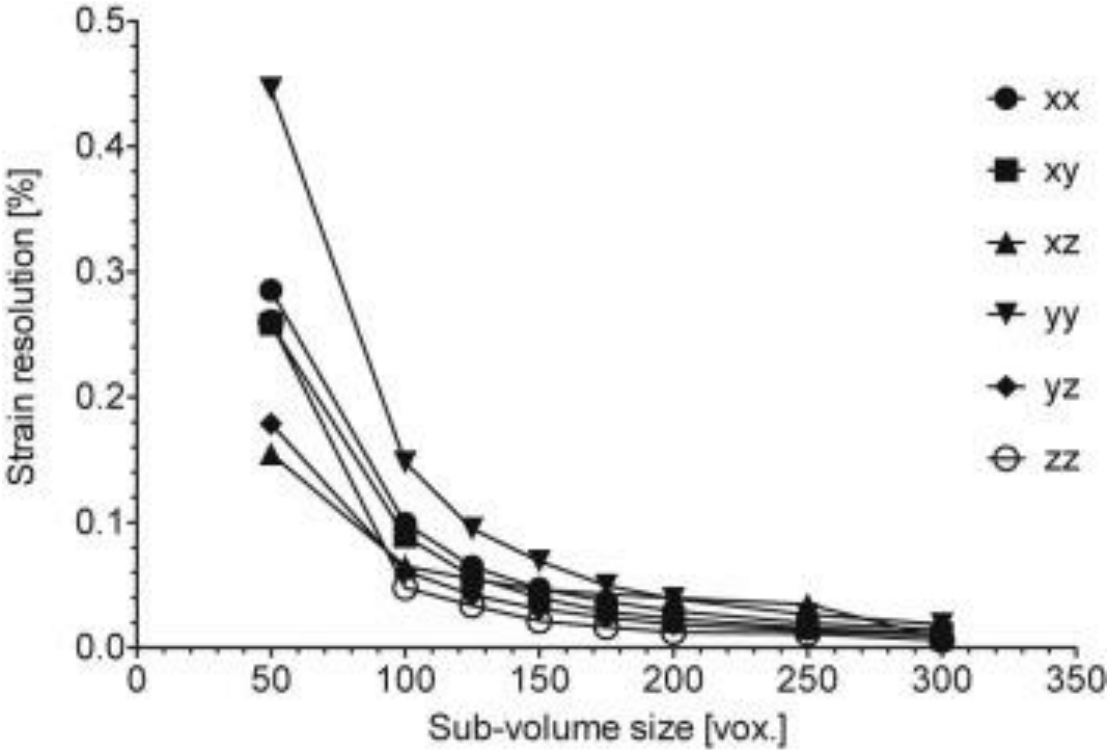

Figure 2-25: The results of the noise study conducted by Borstnar *et al* [16]

This graph illustrates the compromise between strain and spatial resolution. Borstnar *et al* decided to proceed with a sub-volume size of 150 voxels. The results of the rigid body motion study reveal that the displacement was tracked accurately when moved perpendicular to the fibre direction but that when the displacement occurred along the direction of fibres the software was not able to make an accurate measurement. This finding reinforces the known limitation of the DVC technique, in which the tracking of movement along the fibre direction is compromised by the lack of distinct features due to their cylindrical nature, although the displacement in the fibre direction was trackable using the toughening particles present in the material under investigation [16].

The author went on to identify strains ahead of the crack propagation in a number of different planes. These findings are relevant to the current work as identifying strains before, during and after initiation will be a particular focus of the DVC work to be conducted. In the paper presented by Gamstedt *et al* [42], it is acknowledged that capturing debonds ahead of a propagating crack is difficult. Using the DVC approach these areas of increased strain should be identifiable. These important measurements will be used to inform and develop modelling by predicting the crack path. It is further expected that DVC will yield interesting information about the *in situ* material properties of the lamina, as discussed in the paper by Sebaey *et al* [41]. Determining the strain, Poisson's strain, stiffness and strength of the material should be possible using this technique.

2.3.12 DVC displacement values as boundary conditions for finite element analysis

Microstructural finite element models generated from high resolution micro-CT images have proven to be a powerful tool to simulate the mechanical behaviour of cellular materials such as polymeric foams [99-101], metallic foams [102, 103], scaffolds [104]and trabecular bone [105]. The studies presented here show that there has been significant modelling progress but also highlight that the accuracy of the approach for predicting material constitutive behaviour could still be improved. Amongst the limitations reported in the studies, the boundary conditions are cited as a possible source of error. The comparison of DVC results with finite element analysis (FEA), in order to validate the strain predictions, was attempted by Zauel *et al* [24] whose study was focussed on cancellous bone. Good agreement was obtained in the loading direction, but less accuracy was achieved in the transverse directions. They went on to hypothesise that the accuracy was affected by the lateral and vertical boundary conditions.

Madi *et al* [25] aimed to test the above hypothesis in a study of the local strain fields in a polymer foam implant loaded in compression. They suggested that by using the displacement values determined by DVC as boundary conditions for an FEA model, more accurate predictions of strain would be achievable, as would the extraction of more precise strain values at the area of interest. They used two approaches to DVC; an FFT based local and a mesh based global approach. After an appropriate subvolume size was chosen, the reliability and accuracy of the displacement measurements was investigated. They were able to do this by determining the Young's modulus of the material by extracting DVC strain measurements over a range of load increments and comparing them with the documented Young's modulus for the material. The displacement measurements between the two DVC approaches were in good agreement. Micro-CT volumes of the area of interest were then imported into Avizo software (Avizo Standard Edition, 6.3.0, VSG, an FEI company, Burlington, USA) and an unstructured tetrahedral mesh was generated. Following an optimisation study of element size the experimental displacements obtained by the two DVC methods are applied as boundary conditions on the external faces of the FE model.

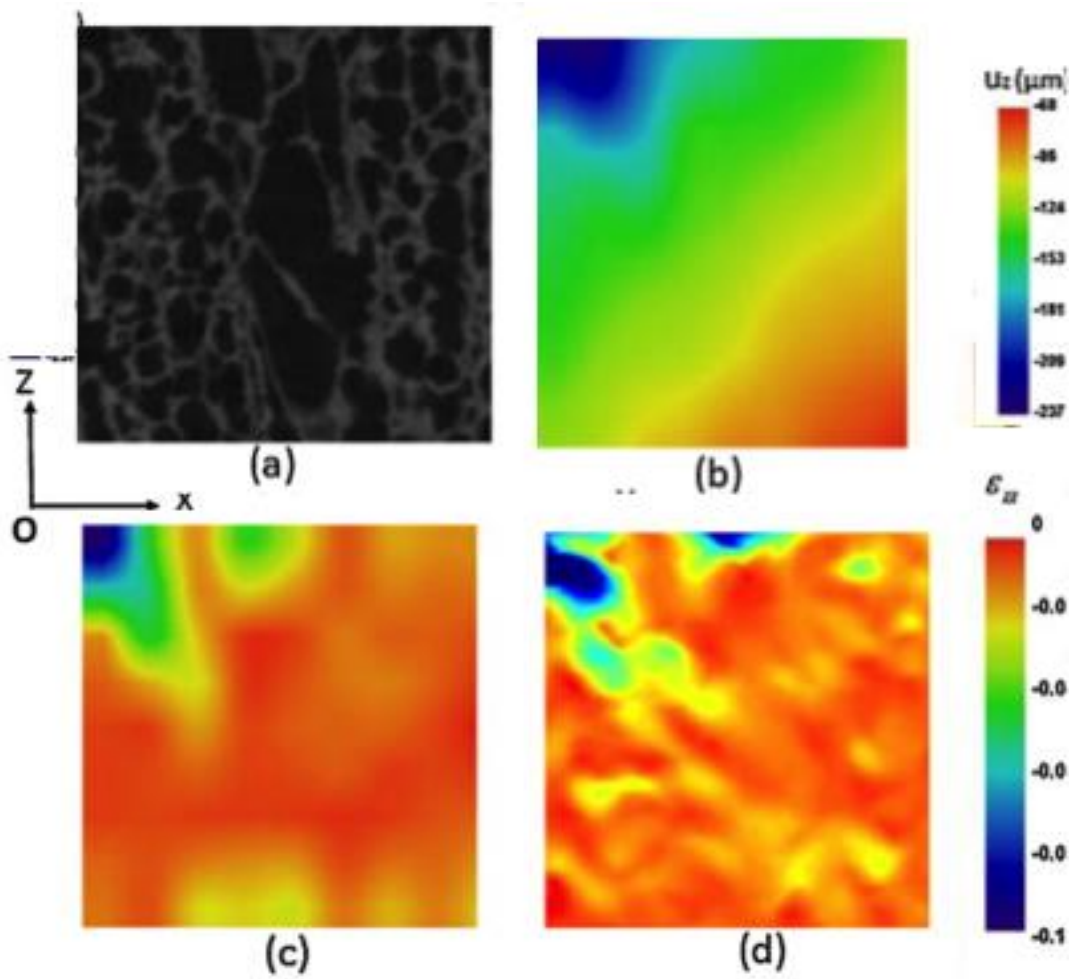

Figure 2-26: The results of the displacement and strain values [25]

Figure 2-26 shows the results of the study. Figure 2-26 a is the microstructure of the region of interest. The compressive load was applied in the z direction. Figure 2-26 b is the displacement values which were used as boundary conditions and Figure 2-26 c and d are a comparison of the strain measured in the z direction between the DVC approach and FEA model respectively. The two methods are shown to be in good agreement.

Lachambre *et al* [60] employed a similar approach as they investigated the use of micro-CT in conjunction with DVC displacement measurements to inform the extraction of stress intensity factors from notched nodular cast iron coupons subjected to fatigue loading. The displacements that they measured were used in an adapted Williams' series to extract the stress intensity factors. The stress intensity factors that they obtained were in good agreement with analytical values. They went on to acknowledge that the limitation of the approach is the comparably large size of the microstructure with regards to the physically small size of the crack.

It is clear that the approach of using the DVC displacement measurements to be used as boundary conditions for FEA modelling of the microstructure imported from micro-CT scans improves accuracy of the model. The strain information from the resulting FEA models can be compared to the DVC strain map and more

precise localised strains may be extracted to verify and inform modelling strategies such as the Onset theory which predicts damage initiation based on strain invariants. The development and use of the Onset theory is explained in the following section.

2.3.13 Section Summary

The studies reviewed show the potential of the DVC technique to determine volumetric strains in materials under load, scanned using CT and the use of the displacement values as boundary conditions for modelling. Although it has been used for a number of studies in composite materials, it has not been used (to the best of the author's knowledge) to determine strains associated with damage initiation.

2.4 Classical modelling approaches and the development of Onset Theory

2.4.1 Introduction

In order to assess and optimise composite structural design, it is necessary to predict the different failure mechanisms.

Whilst there are many theories dealing with damage initiation, most are built around and develop existing damage prediction theories [106]. Current failure theories can be split into two categories: failure theories with (interactive) or without (non-interactive) failure modes. Failure theories with failure modes account for the interaction between different stress components [106]. Theories in this category usually combine all stress and strength components into a single quadratic equation. Failure theories without failure modes do not account for this interaction [106]. The following subsections 2.4.2 – 2.4.4 is a review of the theories upon which many contemporary theories, including onset theory, are based.

2.4.2 Failure theories without failure modes

In this category, failure theories are envelopes that describe the strength of a single unit ply under combined stresses or strains [107]. The predictions made are typically compared with five experimentally obtained strength measurements [107]:

1. Tensile strength along the fibre.
2. Tensile strength transverse to the fibre.
3. Compressive strength along the fibre.
4. Compressive strength transverse to the fibre.
5. Longitudinal shear failure.

2.4.2.1 The Tsai-Hill criterion

Developed by applying Hill's theory of yield in anisotropic materials to heterogeneous composite materials, this criterion has been adapted from the von Mises criterion in that it considers the distortion energy measurement of the total strain energy stored due to loading [108]. Distortion energy is responsible for the shape change in a material. The Tsai-Hill criteria can be expressed as:

9

$$\frac{\sigma_1^2}{x^2} - \frac{\sigma_1\sigma_2}{x^2} + \frac{\sigma_2^2}{y^2} + \frac{\tau_{12}^2}{s_{12}^2} \geq 1$$

Where σ_1, σ_2 τ_{12} are longitudinal, transverse and shear stresses respectively and X, Y and S_{12} are longitudinal, transverse and shear strengths. In addition:

$$X = XT \; if \; \sigma 1 > 0$$

$$X = XC \; if \; \sigma 1 < 0$$

$$Y = YT \; if \; \sigma 2 > 0$$

$$\text{And } Y = YC \; if \; \sigma 2 < 0$$

where T and C denote tensile and compressive strengths respectively.

Since the Tsai-Hill criterion considers the interaction between different stress components, as indicated in equation 1, it is an interactive failure theory. Stress interaction is taken into account to reflect the fact that failure loads of a structure or component subjected to multiaxial stress state may differ from those subjected to uniaxial stress [108]. The Tsai-Hill criterion is limited in that it cannot predict nominal failure modes including fibre failure, matrix failure and fibre-matrix interface failure.

2.4.2.2 The Tsai-Wu criterion

A simplification of the Gol'denblat and Kapnov's generalised failure theory [109] for anisotropic materials, the Tsai-Wu failure criterion is claimed to be the most comprehensive of the polynomial failure criteria [110]. The total strain energy, distortional and dilatational energy, are considered for predicting failure. It is proposed to be more general than the Tsai-Hill failure criterion because it distinguishes between compressive and tensile failure strengths:

10

$$f_1\sigma_1 + f_2\sigma_2 + f_{11}\sigma_1^2 + f_{22}\sigma_2^2 + f_{66}\tau_{12}^2 + 2f_{12}\sigma_1\sigma_2 \geq 1$$

The constants represent the following:

- Longitudinal tensile and compressive tests:

$$f_1 = \frac{1}{X_T} - \frac{1}{X_C} \text{ and } f_{11} = \frac{1}{X_T X_C}$$

- Transverse tensile and compressive tests:

$$f_2 = \frac{1}{Y_T} - \frac{1}{Y_C} \text{ and } f_{22} = \frac{1}{Y_T Y_C}$$

- Shear tests:

$$f_{66} = \frac{1}{S_{12}^2}$$

- Interactive coefficients:

$$f_{12} = -\frac{1}{2}\sqrt{\frac{1}{X_T X_C Y_T Y_C}}$$

Where σ_1, σ_2 τ_{12} are longitudinal, transverse and shear stresses respectively and X, Y and S_{12} are longitudinal, transverse and shear strengths and T and C denote tensile and compressive strengths respectively.

Like the Tsai-Hill criterion, the Tsai-Wu criterion is limited in that it cannot predict different failure modes.

2.4.2.3 Comments on failure criteria without failure modes

Treated as homogeneous anisotropic material, the actual physical mechanisms of failure at the micromechanical level of the composites are not considered in these criteria. Formulation of these criteria is based on empirical data and a curve fitting process that has no analytical foundation [108]. Researchers that recognise that fibre reinforced composites are heterogeneous in their nature [9, 110-112] have proposed that failure criteria for composites predict failure of each constituent separately.

2.4.3 Failure criteria with failure modes without a dehomogenisation process

By separating the failure modes for the fibre and matrix and assigning each a separate failure equation, the criteria in this category attempt to capture the true failure mechanisms of fibre reinforced composites and attempt to predict fibre and matrix failure separately based on strains observed at the macromechanical level. Unlike interactive failure criteria, failure modes in these criteria do not take interaction between multiaxial stresses into account. This separation of

failure modes and non-interaction between stress components have been supported by a number of authors [110, 113].

2.4.3.1 Maximum stress criteria

The maximum stress criterion predicts failure to occur when the stress in one of the principal material directions exceeds the strength in that direction. For a state of plane stress (2D assumption) in a lamina the failure index is computed as follows:

11

$$Max\left(\frac{\sigma_1}{X}, \frac{\sigma_2}{Y}, \left|\frac{\tau_{12}}{S_{12}}\right|\right) \geq 1$$

Where σ_1, σ_2 τ_{12} are longitudinal, transverse and shear stresses respectively and X, Y and S_{12} are longitudinal, transverse and in-plane shear strengths.

Each failure indices in Equation 11 predicts a certain failure mode as follows:

- If $\frac{\sigma_1}{X} \geq 1$, fibre failure occurs
- If $\frac{\sigma_2}{Y} \geq 1$, transverse matrix failure occurs
- If $\left|\frac{\tau_{12}}{S_{12}}\right| \geq 1$, shear matrix failure occurs

The maximum stress criteria does not consider the interactions between different stress components.

2.4.3.2 Maximum strain criteria

The maximum strain criterion predicts that failure of a material will occur when the critical strain is exceeded. Three failure modes are considered:

12

$$Max\left(\frac{\varepsilon_1}{\varepsilon_1^{crit}}, \frac{\varepsilon_2}{\varepsilon_2^{crit}}, \left|\frac{\gamma_{12}}{\gamma_{12}^{crit}}\right|\right) \geq 1$$

Where ε_1, ε_2 and γ_{12} are longitudinal, transverse and shear strains and ε_1^{crit}, ε_2^{crit} and γ_{12}^{crit} are corresponding critical strains.

Each failure indices in Equation 5 predicts a certain failure mode as follows:

- If $\frac{\varepsilon_1}{\varepsilon_1^{crit}} \geq 1$, fibre failure occurs
- If $\frac{\varepsilon_2}{\varepsilon_2^{crit}} \geq 1$, transverse matrix failure occurs
- If $\left|\frac{\gamma_{12}}{\gamma_{12}^{crit}}\right| \geq 1$, shear matrix failure occurs.

The maximum strain criterion does not take the interaction of different strain components into account.

2.4.3.3 The Hashin-Rotem criteria

The criteria in this predictive theory can be used for tensile or compressive stresses. The corresponding strengths chosen depend upon the sign of the applied stresses. The criteria are given as:

- Fibre failure

13

$$\frac{\sigma_1}{X_T} \geq 1$$

- Matrix failure

14

$$\left(\frac{\sigma_2}{\gamma_T}\right)^2 + \left(\frac{\tau_{12}}{S_{12}}\right)^2 \geq 1$$

Where σ_1, σ_2 τ_{12} are longitudinal, transverse and shear stresses respectively and *X, Y* and S_{12} are longitudinal, transverse and in-plane shear strengths respectively. By comparing the ratios $\frac{\sigma_2}{\gamma_T}$ and $\frac{\tau_{12}}{S_{12}}$ the mode of matrix failure can be determined [114].

2.4.3.4 The Hashin criteria

Based on the second-degree polynomial expansion from the general polynomial criteria (similar to Tsai-Wu criteria), the Hashin criteria separates the failure modes into matrix and fibre dominated depending on which stress components act on the parallel and perpendicular failure planes. Although there are no interaction terms, failure due to tension or compression is distinguished. The four failure modes are given as [115]:

- Fibre failure in tension ($\sigma_1 > 0$)

15

$$\left(\frac{\sigma_1}{X_T}\right)^2 + \left(\frac{\tau_{12}}{S_{12}}\right)^2 \geq 1$$

- Fibre failure in compression

16

$$\left(\frac{\sigma_1}{X_C}\right)^2 \geq 1$$

- Matrix failure in tension ($\sigma_2 > 0$)

17

$$\left(\frac{\sigma_2}{Y_T}\right)^2 + \left(\frac{\tau_{12}}{S_{12}}\right)^2 \geq 1$$

- Matrix failure in compression

18

$$\left(\frac{\sigma_2}{2S_T}\right)^2 + \left[\left(\frac{Y_C}{2S_T}\right)^2 - 1\right]\frac{\sigma_2}{Y_C} + \left(\frac{\tau_{12}}{S_{12}}\right)^2 \geq 1$$

Where σ_1, σ_2 τ_{12} are longitudinal, transverse and shear stresses respectively and X_T, Y_T and S_{12} are longitudinal, transverse and in-plane shear strengths. S_T is the transverse shear strength.

2.4.3.5 The Puck criteria

Puck proposed that fibre (ff) and interfibre failure (iff) should be treated by separate and independent failure criteria. The criteria for failure are as follows:

- $\sigma_{\parallel}$ (tension and compression)
- $\sigma_{\perp}$(tension and compression)
- $\tau_{\perp\perp}$ and $\tau_{\perp\parallel}$ (shear)

Figure 2-27 shows these stress components schematically. Where stress is applied parallel to the direction of the fibres, failure is said to occur in the fibre. The other remaining stresses are said to cause matrix failure.

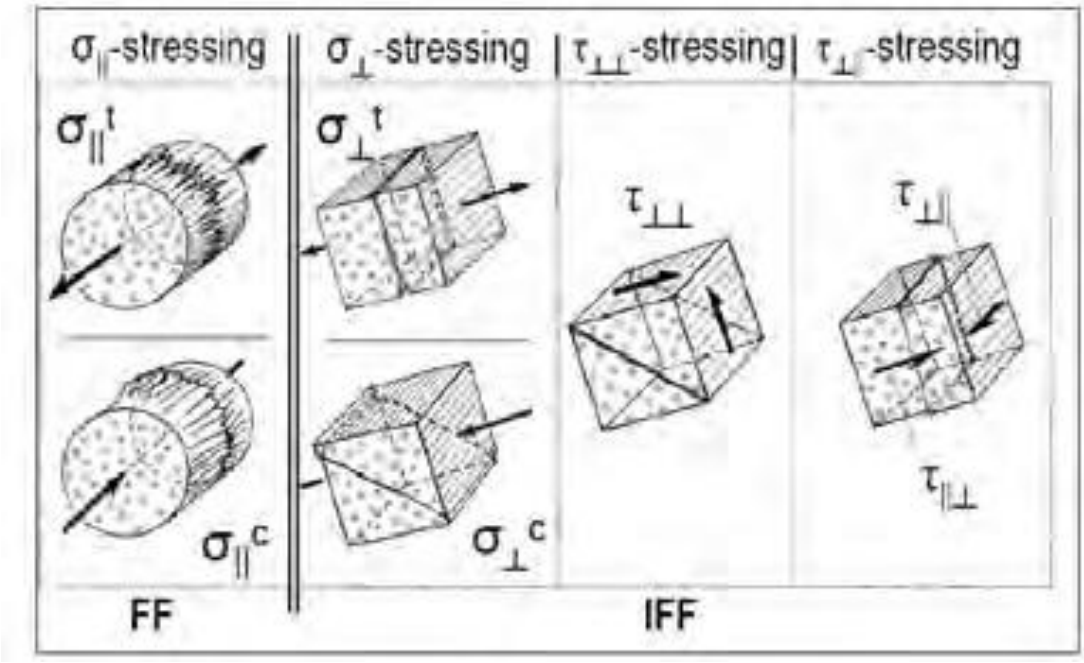

Figure 2-27: Shows the stress components of the Puck criteria [116]

The inclusion of separate fibre and matrix failure modes in this category of methods to predict failure acknowledges the heterogeneous nature of the material and attempts to predict failure in each of the constituent materials. The formulation of these methods at the macromechanical level means that the materials are considered as homogeneous solids and a pronounced distinction between fibre and matrix is ignored.

2.4.4 Failure criteria with failure modes with a dehomogenisation process

Failure criteria in this classification are based on the physical mechanics of damage initiation. They overcome the disadvantages introduced in the previous subsections by treating the fibre and matrix separately at the micro scale.

2.4.4.1 Onset Theory

Formerly known as the Strain Invariant Failure Theory, the Onset theory is a micromechanics damage theory for composites proposed by Gosse and Chistensen [9] and Hart-Smith [117]. Mainly applicable to glassy polymers constrained by fibres in structural composites, the authors argue that the failure of the matrix can only occur in two non-interactive modes: distortion and dilatation. As a result, the Onset theory uses two strain invariants, the distortion invariant and the dilatational invariant to predict the onset of irreversible polymer deformation in composite structures.

The equations, which govern the Onset theory, are:

Dilatation:

19

$$J_1 = \varepsilon_1 + \varepsilon_2 + \varepsilon_3$$

Distortion:

20

$$J_2 = \sqrt{\frac{1}{6}[(\varepsilon_1 - \varepsilon_2)^2] + [(\varepsilon_1 - \varepsilon_3)^2] + [(\varepsilon_2 - \varepsilon_3)^2]}$$

Strain invariants are calculated by dehomogenising the constituent fibre and matrix strains from analysis conducted on the strain state at the structural level. In contrast to purely empirical failure criteria, the aim of dehomogenisation is to assign failure mechanisms according to a physical basis. Gosse *et al* used a multiscale modelling approach to determine the microscale deformation in the fibre and matrix phases from deformation observed at the structural level [9, 118]. The strain enhancements, obtained from square and or hexagonal unit cell models (described in 2.4.5), are used to scale strains at the macroscopic level before the strain invariants can be calculated. The onset theory is claimed to be applicable to the general case as it is based on the use of strain invariants. The

theory has been validated within the research and industry community [111, 119] and is being applied to a broadening range of problems, which cannot be analysed by stress- based failure theories.

As with the other failure theories onset theory requires appropriate scrutiny and challenge. Firstly, little work has been conducted on its use for toughened systems. Polymeric resins are usually brittle and notch sensitive. This leads to poor crack initiation and propagation resistance [110]. The toughening of polymer resins has received considerable attention and research in terms of their effect on the application of failure theories. The incorporation of dispersed rubber particles has proven to be a successful method for improving toughness [120, 121]. The basis of particle toughening is the cavitation of rubber particles followed by plastic deformation of the matrix. This is considered to be the major contribution of particle toughening [59]. The second considerable limitation is that to date the theory has only been used to predict the onset of damage in unidirectional components.

2.4.4.2 Micro-mechanics of failure (MMF)

Proposed by Ha *et al* [122], the micromechanics of failure (MMF) criteria further advances the micromechanical amplification concepts originally proposed in the development of the Onset theory, but develops a new criterion based on micromechanically enhanced stresses. Further differing from the Onset theory which assumes the interfacial effect to be subsumed into the bulk behaviour of the phases, the MMF criteria considers the effect separately. Unit cell models with boundary conditions are used to obtain micromechanical and thermal amplification factors which are then used to predict fibre failure, matrix failure and interfacial failure.

The MME has had some success, as reported in [122], however the theory is limited in that obtaining the stress amplification by mechanical testing, requires time and considerable effort.

2.4.4.3 Multicontinuum theory (MCT)

Proposed by Mayes and Hansen [123], the stress-based criteria for this approach are applied at the micromechanical level. A multiscale modelling approach is used to determine a continuum-based (phase-averaged) constituent stress and strain field from a composite structure, Figure 2-28. The stresses are then used to predict fibre or matrix failure.

2.4.5 Multiscale modelling for failure of composites

Aimed at calculating macroscale material properties or modelling structural behaviour using information or models from different finer levels, multiscale modelling is particularly useful since the mechanisms of damage occur over multiple length scales [28]. More robust computational methods and larger computer processing power mean that models no longer have to be constrained to the macrolevel at which the interaction between fibres and matrix are ignored. Recent work [10, 28, 29, 48, 112] has shown that these local effects are

significant and that it is necessary to be able to model at the micromechanical level to predict damage and failure.

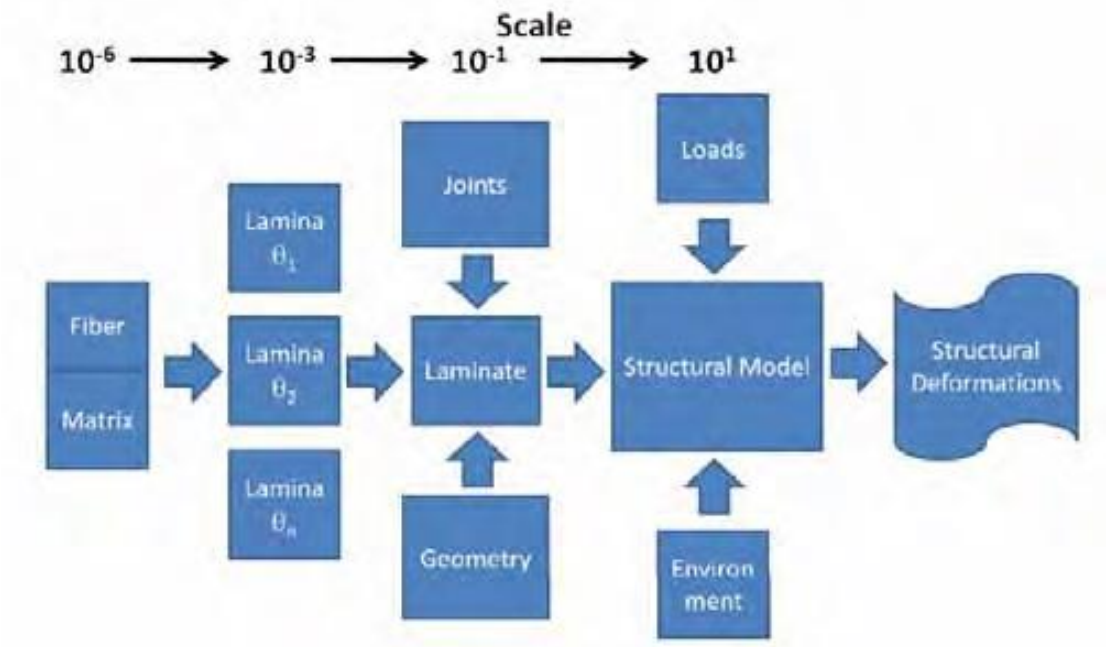

Figure 2-28: Scales (m) of composite material analysis [28]

The onset of irreversible deformation in composite material begins at the constituent phase and the prediction of damage at this scale can only be achieved when the deformation state for each heterogeneous composite has been determined [118]. To fully realise a stress or strain state for each constituent in a composite structure is not an easy task, so a multi scale modelling method is one feasible approach. Multiscale modelling is normally conducted considering at least two length scales; macro (structural) and microscopic (fibre/ matrix) levels.

Early significant multiscale modelling work was conducted by Gosse *et al* [9, 118], the creators of the onset theory. The approach they developed makes use of micromechanical strain amplification factors to determine strains in the fibre and resin from the strains observed in a continuum model. The amplification factors the authors use are derived from unit cell finite element analysis that assume an arrangement of fibre and resin shown in Figure 2-29: Square and hexagonal array representative volume elements (RVE)[110].

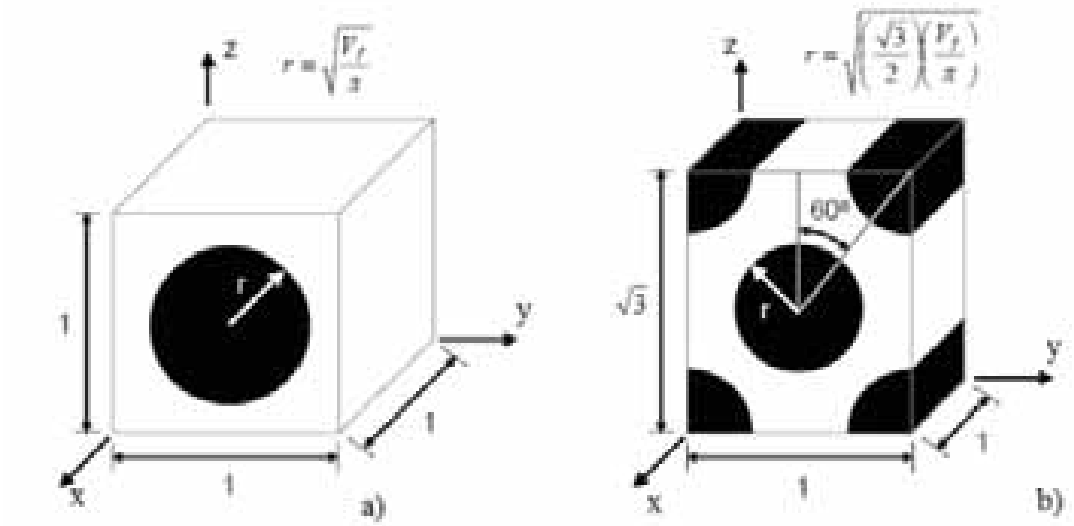

Figure 2-29: Square and hexagonal array representative volume elements (RVE)[110]

The square and hexagonal fibre packing arrays have been shown to provide bounding magnification factors on all of the possible random arrays [112]. Laminate strains are determined using finite element analysis and scaled down by magnification factors before the strain invariants are calculated and compared to the critical values used to predict failure. Dehomogenised strain fields at the micromechanical level are achieved and failure criteria can be established for fibre and matrix separately.

Ha *et al* [122] extended the method to formulate a multiscale model based on stress. They use the same mechanical enhancement concepts but stress between the fibre and matrix is taken into account. Their work considered the effects of random fibre packing and compared it to regular, square and hexagonal fibre packing arrays proposed in the work by Gosse. Ha concluded by acknowledging that strength predictions based on random packing arrays are very close to regular arrays, so that using the regular arrays is valid and sufficient.

The calculation of strain invariants is a time-consuming process requiring multiple experiments to determine the critical values. Recent work to develop the onset theory by Tran *et al* [106] has simplified the process by developing a dehomogenisation code, which significantly speeds up the calculation of strain invariants and reduces computer-processing time.

2.4.6 Section summary

It is evident from the damage theories presented that no universally accepted modelling theory for damage initiation exists. Until there is a body of work that can adequately describe the three-dimensional mechanisms of damage initiation (potentially using volumetric techniques such as CT), prediction of damage occurrence and validation of theories is made difficult. It is hoped that the techniques developed in this work will be built on and used to improve our understanding and lead to an accepted prediction model.

3 Materials and Methods

3.1 Overview

This chapter describes:

- The materials used in the study
  - Material description and lamina properties
  - Composite laminate theory is used to calculate material properties of the layups used.
  - Fibre volume fraction determination.
  - Preparation of coupons for testing – coupon geometry, cutting polishing and tab attachment.
  - Mechanical testing – Determine average coupon tensile failure strength for each layup and location of fracture.
- Synchrotron Radiation Computed Tomography testing
  - *In-Situ* testing – a description of experimental setup
  - Specimen tilt
  - Scan parameters used at ESRF
  - Crack identification and segmentation – post processing method

3.2 Material

Boeing, supplied carbon fibre reinforced polymer (CFRP) plates 400mm x 300mm x 1.6mm of Toray T800S/3900-2 particle toughened CFRP, which the manufacturer states has 60% fibre volume fraction, a fibre diameter of 5 μm and a ply thickness of 0.2 mm [69]. This material is widely used in aerospace structures [124]. Three layups $[0,90]_{2s}$, $[\pm10]_{2s}$ and $[90]_8$ were supplied (axis defined in section 2.1.2). The $[90]_8$, and the $[\pm10]_{2s}$ were supplied to interrogate dilatational and distortional strain effects on damage initiation, as described in section 2.4.4.1. The lamina properties of the material are given in Table 3-1[106].

3.2.1 Properties

Table 3-1: The lamina properties of the material [106]

Property	Value
E_1	152 GPa
E_2	8 GPa
E_3	8 GPa
G_{12}	4 GPa
G_{23}	2.75 GPa
G_{13}	4 GPa
ν_{12}	0.34
ν_{23}	0.45
ν_{13}	0.34

Using composite laminate theory, described in section 2.1.2, the material properties for each lay-up were calculated. Table 3-2, Table 3-3 and Table 3-4 show the calculated material properties for each layup.

Table 3-2: Laminate properties for the $[\pm 10]_{2s}$ material

[±10]2s Material Properties	Value
E_z	138.9 GPa
E_x	8.16 GPa
ν_{zx}	0.818
ν_{yx}	0.047

Table 3-3: Laminate properties for the $[0,90]_{2s}$ material

$[0,90]_{2s}$ Material Properties	Value
E_z	80.93 GPa
E_x	80.93 GPa
ν_{zx}	0.34
ν_{yx}	0.34

Table 3-4: Laminate properties for the $[90]_8$ material

[0,90]2s Material Properties	Value
E_z	8 GPa
E_x	152 GPa
ν_{zx}	0.018
ν_{yx}	0.34

Fibre volume fraction and fibre diameter were assessed directly: three coupons of the $[0,90]_{2s}$ material were set in resin and were then polished The resin containing the coupons was subject to a fine grind using grain sizes of 15, 9 and 6 μm grinding paper, and then polished with diamond paste, as per the techniques described in [69], and viewed under an optical microscope, Figure 3-1. The fibre volume fraction was found, using point grid counting, to be 65% (±3%), the average fibre diameter 5.2 μm (range 5.1 -5.4 μm) and the ply thickness 0.2 mm (±0.005mm).

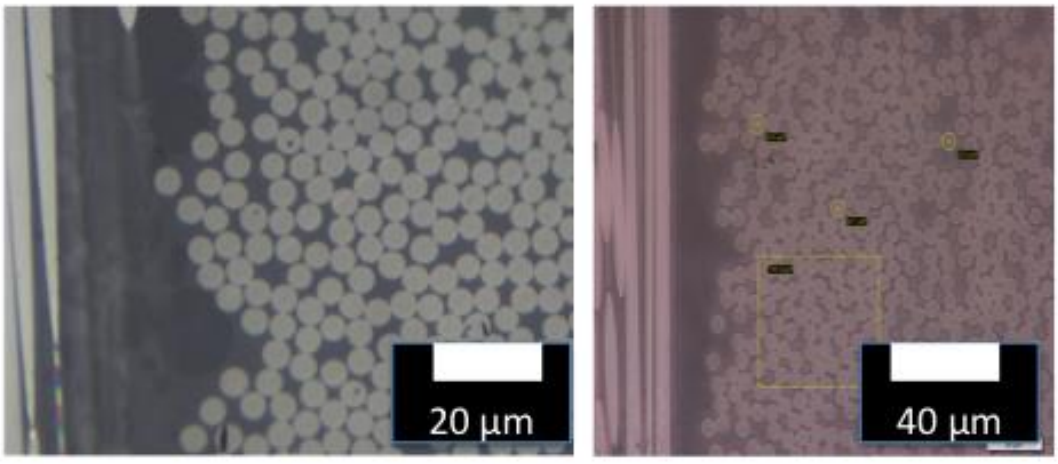

Figure 3-1: The polished coupon used to determine fibre volume fraction and fibre diameter – fibre volume fraction was found to be 65% and fibre diameter 5.2 μm

3.2.2 Preparation

A double notched coupon geometry chosen for SRCT *in situ* tensile testing was 66mm x 4mm x 1.6mm with semi-circular notch sections of radius 1.5mm either side of the centre of the coupon, as described in previous studies [62], Figure 3-2: Coupon geometry used for this study. Load was applied in the z direction. This notch creates a nominal width at the centre of ~1mm. Given the thickness of 1.6mm, the cross-sectional area at the centre of the notch is $1.6x10^{-6}m^2$.

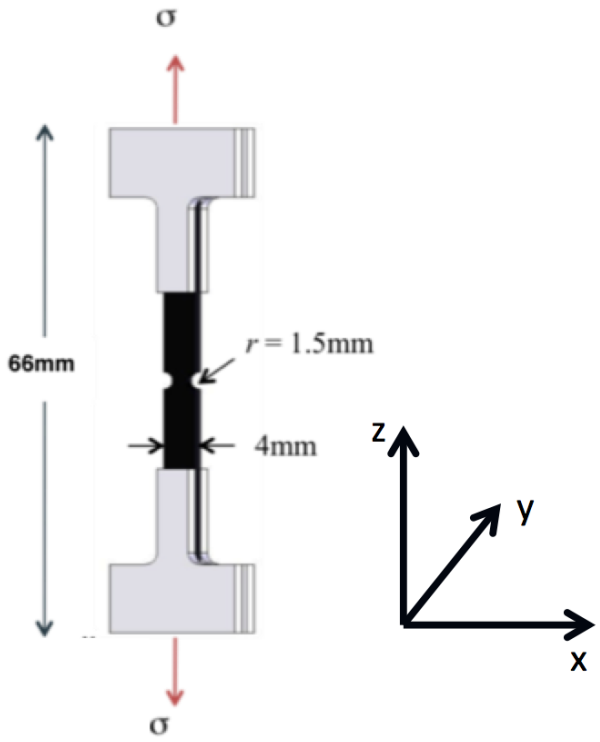

Figure 3-2: Coupon geometry used for this study. Load was applied in the z direction

Suitable cutting methods for this coupon geometry potentially include waterjet cutting [125, 126] and machining [127]. Laser cutting was also investigated and rejected due to the possible change of material properties as a result of heating. Considering images of water jet cut coupons (from historical tests within the research group), it was decided that the surface finish of the notch needed to be improved to reduce the crack initiation stress raisers associated with edge defects. As such it was decided that the material would be waterjet cut to the required dimensions. The notch surface was subject to a similar polishing regime as described in 3.2.1. Once polished, aluminum end tabs were attached to both sides at both ends of the coupon using a two-part epoxy in accordance with the method described in [12] whereby the surfaces of both the CFRP and the aluminium end tabs was keyed to allow for better adhesion when glued. Figure 4.3 illustrates the position of the tabs. Care was taken to align the tabs so that the horizontal load-bearing inner shoulders of the tabs were perpendicular to the centreline of the composite specimen.

3.3 Tensile testing

Average tensile strength was determined for each layup using an Instron servo mechanical 50 kN test machine. Un-tabbed specimens were loaded in the wedge grips of the test machine: care was taken to align the specimen perpendicular to the direction of loading to minimise axis forces (using a Rion Mini Digital inclinometer). A load rate of 5mm/min was used for the testing. Once tested to failure, the coupon was examined to ascertain where, with respect to the centre of the notch, final failure occurred so that an area of interest could be focused on when conducting CT scans. Three specimens of each layup were measured to determine the tensile strength variability. All coupons failed in the notch region. Table 3-5 reports the findings of the tensile testing. These values were then used to determine the load used and the location at which the beam should be focused when at the synchrotron.

Table 3-5: The results of the tensile testing

Layup	Average Tensile Strength (MPa)	Range (MPa)	Fracture Location
$[\pm 10]_{2s}$	1663	1624.3 – 1692.1	Centre
$[0,90]_{2s}$	1241	1208.8 – 1260.9	2/3 of the way along notch
$[90]_{8}$	39	31.9 – 49.2	Centre

3.4 Synchrotron Radiation Computed Tomography

3.4.1 *In Situ* loading and Scanning

The coupons were tested *in situ* at the ID19 beamline (ESRF, France), using a Deben CT5000 load rig (capable of loads up to 5 kN). This beamline was chosen due to: 1) Prior experience (2) known compatibility with custom designed fixtures (3) robust rotation stage capable of accepting off-axis loads (4) sufficient height available between the rotation stage and X-ray beam to allow room for tilting (see section 3.4.2.

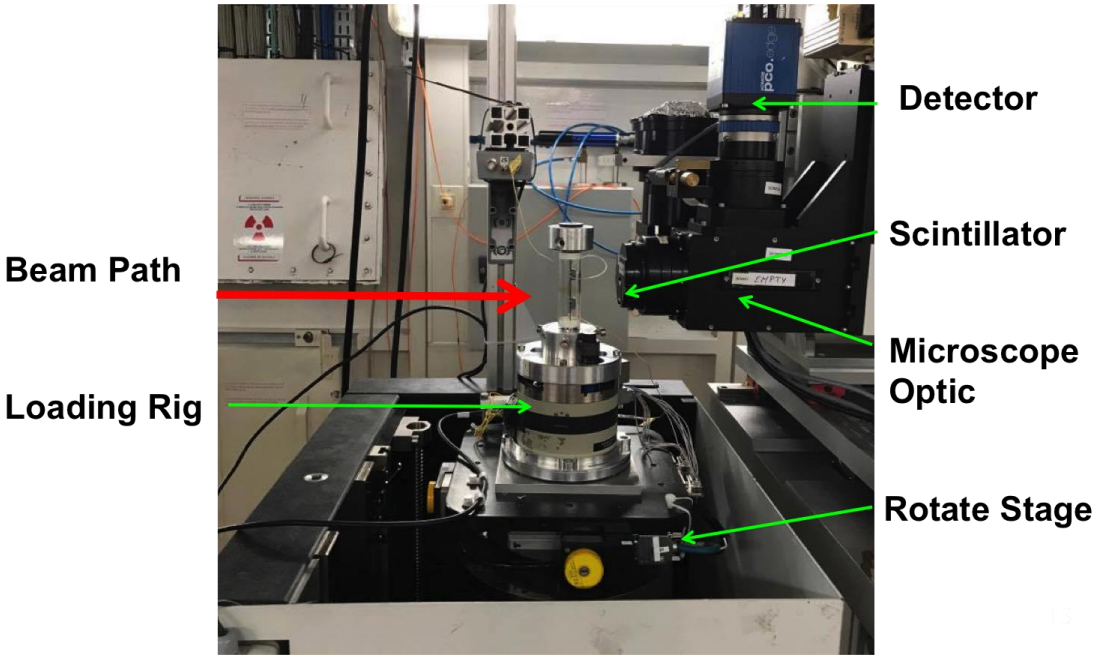

Figure 3-3: The experimental setup at the ESRF

Figure 3-3 shows the experimental setup used at the ESRF. A wired connection was run from the Deben rig to the control room via a slip ring. To avoid image artefacts caused from fibres lying in the same plane as the X-ray beam, the load rig was tilted so that the 90° fibres of the coupon at ~ 20° relative to the path of the beam, Figure 3-4, and uniaxial loading could be applied.

3.4.2 Specimen Tilt

In order to avoid image artefacts caused from fibres lying in the same plane as the X-ray beam, the whole load rig was tilted so that the 90° fibres of the coupon were 20° relative to the path of the beam, see Figure 3-4.

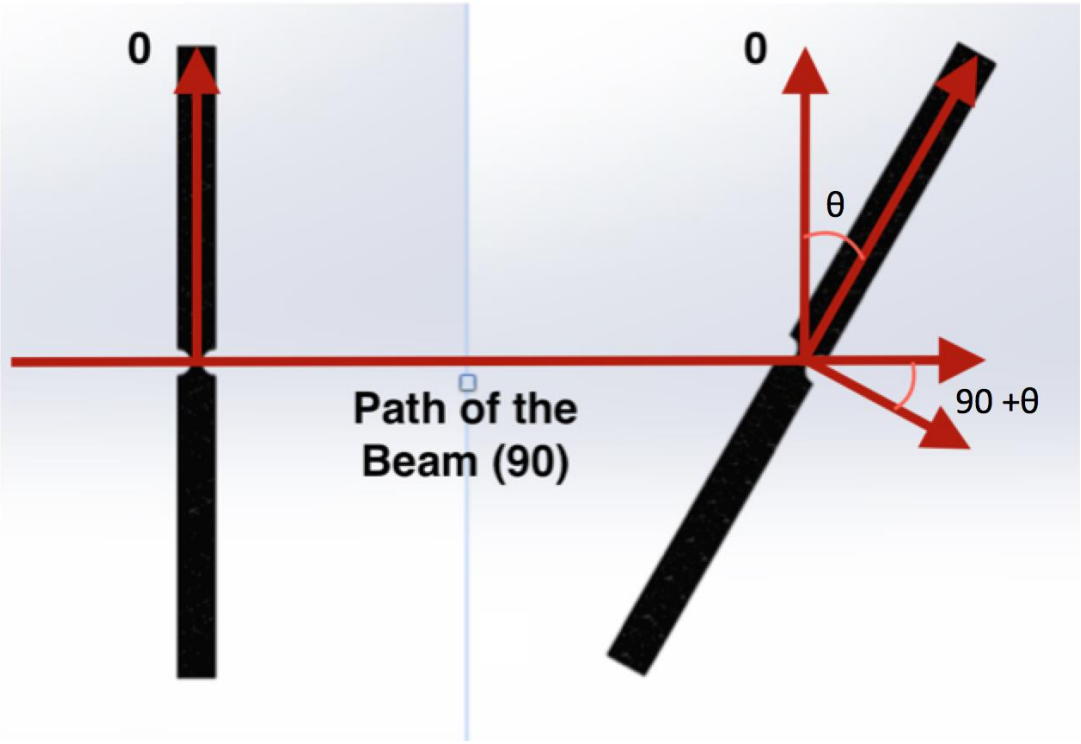

Figure 3-4: The coupon was tilted to 20° to avoid the imaging artefact

The coupon was tilted as a solution to a suspected phase artefact identified when the 90° plies are parallel to the path of the beam, as shown in Figure 3-5.

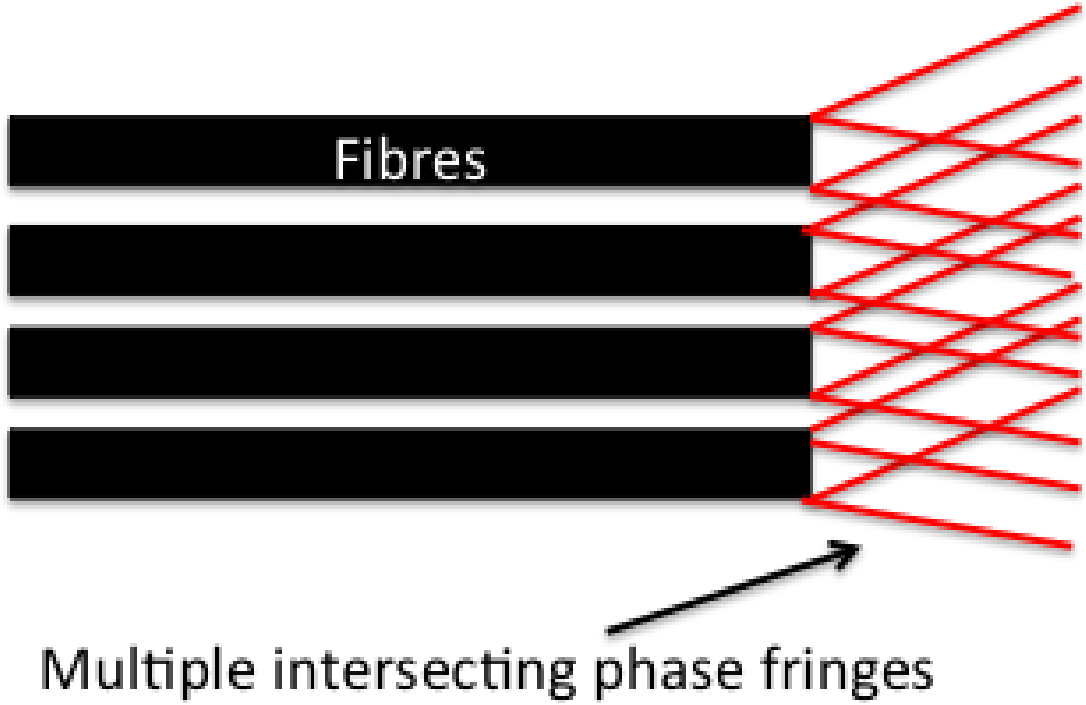

Figure 3-5: The close packed nature of the fibres means that phase fringes caused by the multiple fibre edges lead to many intersecting phase effects in fibres parallel to the path of the beam, which may lead to the blurring artefact

Figure 3-6 a and b: Shows the effects of the phase artefact when the fibres are parallel and tilted relative to the path of the beam respectively. Figure 3-6 a, shows the artefact in the 90° plies in a $[0,90]_{2s}$ coupon scanned at the Swiss Light

Source (Figure 3-6 b, is the 90° plies resulting from a scan in which the coupon is tilted relative to the path of the beam. A comparison between the two Figure 3-6 a and b, highlights the improvement in the resolution. The $[0,90]_{2s}$ and $[90]_8$ were scanned in the tilted loading rig. The $[\pm10]_{2s}$ coupon was scanned with no tilt applied as no plies lay in the plane of the incident beam.

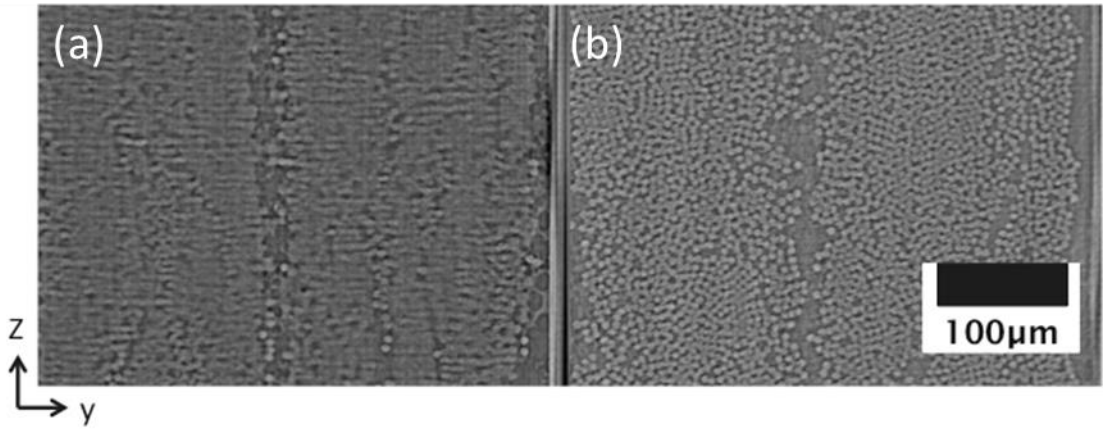

Figure 3-6 a and b: Shows the effects of the phase artefact when the fibres are parallel and tilted relative to the path of the beam respectively. Figure 3-6 shows the artefact in the 90° plies in a $[0,90]_{2s}$ coupon scanned at the Swiss Light Source. Figure 3-6 b, is the 90° plies resulting from a scan in which the coupon is tilted relative to the path of the beam. A comparison between the two Figure 3-6 a and b, highlights the improvement in the resolution

3.4.3 Scanning Parameters

Table 3-6 shows the scanning parameters used to capture each of the scans, these are similar to the scan settings used in [59-60]. Table 3-7shows the number of scans conducted for each layup.

Table 3-6: Scanning parameters used at the ESRF

Parameter	Setting
Voxel resolution	625 nm
Field of view	1.6 mm x 1.4 mm
Energy	21 keV
Exposure	5 ms
Projections	2996
Propagation distance	51mm

Table 3-7 Number of scans conducted at the ESRF

Layup	Stage tilt	DVC noise trial	Number of load steps	Number of coupons tested	Total number of scans
$[\pm10]_{2s}$	✔	✔	5	2	13
$[0,90]_{2s}$	✔	✔	7	3	25
$[90]_8$	✔	✔	1	1	1

To assess the level of noise that could influence the DVC analysis, a study was conducted whereby two identical scans of the unloaded coupon and a rigid body

motion scan, in which the coupon was displaced by 5 µm in the z direction were performed. The coupons were then loaded incrementally and scanned. Three $[0,90]_{2s}$ coupons were loaded and scanned at 0, 15, 20, 22.5, 25, 27.5 and 30% of the UTS, Table 3-8. Two $[\pm10]_{2s}$ coupons were loaded and scanned at 0, 20, 30, 40 and 50% UTS. The $[90]_8$ coupons broke before loading could be advanced beyond an initial scan.

Table 3-8: The load steps conducted on each layup

Layup	UTS (MPa)	Load step 1	Load step 2	Load step 3	Load step 4	Load step 5	Load step 6
[0,90]2s	1241	185	250	280	310	340	380
[±10]2s	1663	330	500	665	830		

3.4.4 Crack identification and segmentation

The results of the scans were reconstructed using filter back projection techniques, described in section 2.2.4. The reconstructed scans were initially processed using Fiji™ [128]. In order to align the scan volumes such that the 90° fibres could be viewed in cross-section, the volume was first rotated by 20°, Figure 3-7 a and b. The volume was then resliced from the right, as shown by the yellow line in Figure 3-7 c, resulting in Figure 3-7 d. The individual plies can be seen including the fully resolved transverse plies. In order to reduce the file size, this volume was then cropped to include only the ROI.

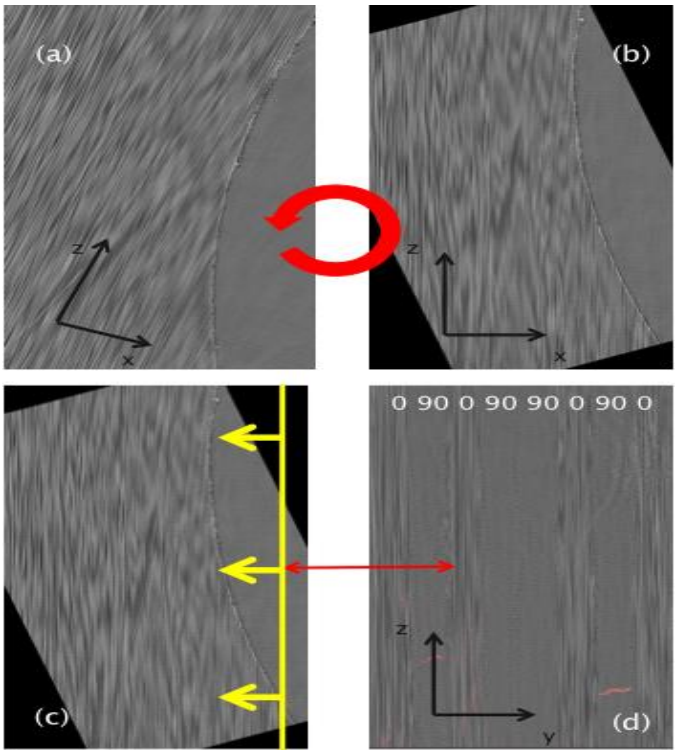

Figure 3-7 a-d: The realignment process conducted on the reconstructed volume of the tilted coupon. The volume was first rotated 20° images a and b the volume was then resliced from the right, as shown by the yellow line in Figure 3-7 c, resulting in the 90° fibres visible in Figure 3-7 d.

4 Method Paper

The following chapter was submitted to the journal of composite materials (Composites A) and serves as the method and validation for the use of DVC in identifying damage initiation events. There is limited discussion as to the nature of damage, this will be covered in more detail in Chapter 5. It was deemed that whilst the paper was well written, additional work was required in order for it to be including in the publication.

The measurement of transverse strains by digital volume correlation in a carbon fibre composite

4.1 Abstract

Digital volume correlation has been assessed as a tool to measure sub-ply level strains within laminated carbon fibre composites. Specimens of carbon fibre epoxy composite, produced from prepreg and by autoclave processing in a $[0,90]_{2s}$ lay-up were loaded *in situ* while being imaged by synchrotron radiation computed tomography. The use of DVC in unidirectional (UD) long fibre-reinforced polymers (FRPs) has not been well documented; this is due to a number of technical difficulties that arise from the highly anisotropic and somewhat regular nature of the underlying microstructure. The work presented in this study is a first of its kind investigation (to the best of the author's knowledge) of the technique in an industrial carbon-epoxy FRP, the results of which aim to demonstrate the capability of the technique and corresponding results.

4.2 Introduction

It has been well documented over the past twenty years that there is a deficiency in reliable predictive models for the failure of composite materials under multi-axial loading [129]. This restricts the ability to exploit fully the properties of the materials, as well as adding cost and time to the design process in order to develop designs, which meet the requirements for structural integrity. The ability to measure full-field strains while conducting loading experiments in order to verify model predictions is potentially a key step in failure model validation. Improvements in numerical tools, such as finite element analysis, have meant that the capability to model stresses and strains and pin principles down to very fine levels of microstructural detail has surpassed the ability to verify the predictions [17]. Stress and strain, as second order tensors, vary with position and orientation, over length scales determined by microstructural features, as well as at the structural level. Traditional tools such as strain gauges, although very useful, can only describe the strain state at a few discrete points, and at scales well above those of the material microstructure, and only for the components of strain parallel to the surfaces. In order to understand the role of material microstructure in determining failure, new techniques are of interest.

The use of Digital Image Correlation (DIC) for the identification and magnitude of full-field strains has been well documented [32, 71, 85, 88, 93]. This technique is however fundamentally surface-based. Digital Volume Correlation (DVC) in conjunction with volumetric imaging techniques such as computed tomography (CT), confocal microscopy (CM) and magnetic resonance imaging (MRI) potentially allow the user to quantify the volumetric strains in an otherwise opaque material, and in principle, to obtain all components of the strain tensor at a particular point [18]. Since its adaption from the two-dimensional DIC technique in the late 1990s, the DVC technique has seen a number of technical refinements and an increase in its applications [17, 18, 73]. Recent work has focussed on technique development, measurement accuracy quantification and adaptation to specific applications such as bone, concrete, metallic foams and soil/plant roots [19, 80, 83, 92, 97]. DIC and DVC have been used in a number of studies to investigate damage mechanisms at the microstructural level in composite materials [32] [16, 22, 60]. For instance Canal *et al* [32] used DIC in conjunction with *in situ* testing and scanning electron microscopy (SEM) on glass fibre reinforced polymer loaded in compression to validate and inform their modelling technique results. Borstnar *et al* [16] identified a number of limitations when using DVC to analyse UD carbon-epoxy materials, particularly along the fibre direction. As described in the following section, DVC requires two volumes; one reference undeformed volume and one deformed volume in order to quantify the 3-D displacement field, which ensues as a result of loading and/or damage development. Matching and cropping these volumes of interest from the bulk volume requires careful selection and relies on internal features and microstructural patterns which can be correlated between images at different loading steps. In contrast to DIC, where a separate speckle pattern is usually applied to the surface, DVC ideally exploits contrast present due to the microstructure. In the case of aligned continuous fibre composites there is a relative lack of unique features as a result of the fibre uniformity and alignment, meaning that it is possible to mismatch a volume selection in the fibre direction. The DVC approach relies on unique, consistently identifiable features to track displacement and the lack thereof introduces measurement uncertainty.

Figure 4-1 illustrates the anisotropic structure of a conventional UD composite. The fibres, which are nominally straight (to within a few degrees at least), create a unique pattern, in the y-z plane shown in this diagram, which may be anticipated to make displacements in those directions measurable by DVC (notwithstanding a degree of regularity that may arise at high packing densities of uniform circles/cylinders). The lack of unique features in the fibre (x) direction, means that displacements are more problematic to track and may therefore lead to anomalous strain values being recorded, as well as causing difficulty in registering a particular y-z plane.

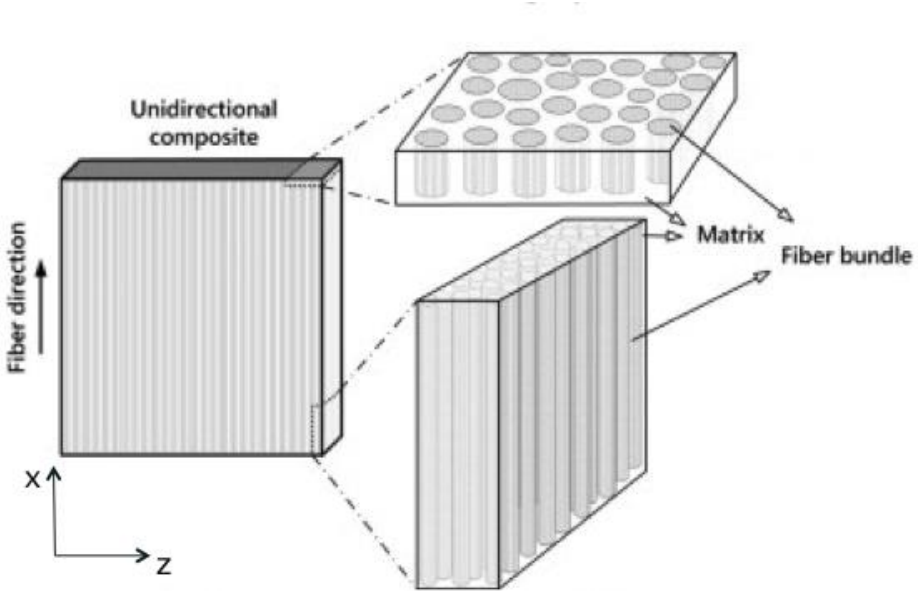

Figure 4-1: The anisotropic nature of long fibre reinforced polymer showing the lack of features in the fibre direction [130].

In the work conducted by Borstnar *et al,* the authors were able to use existing particles at the ply interfaces in a particle-toughened system to provide a trackable pattern. This allowed reasonably accurate selection of volumes and calculation of displacements and hence local strains at the interfaces. Borstnar *et al.* were largely unconcerned with the displacements and strains in the fibre direction within the plies themselves. At the time of writing no other work appears to have attempted to use DVC techniques to measure strains in unidirectional plies within laminated composites.

The aim of the present work is thus to explore the feasibility of measuring strains within the plies of laminated continuous fibre composites via DVC, using the patterns of fibre distribution in the transverse planes to provide comparative volumes. This study is part of a research project into the effects of local strain and microstructure on the initiation of damage in the off-axis plies in CFRP. The validity of DVC to identify strains, and hence potentially damage initiation processes, was assessed in terms of system noise studies, comparison to quasi 2D-analysis and DVC sub-volume anisotropy.

4.3 DVC technique description

The DVC technique tracks displacement between pairs of digital image volumes (comprising a reference and a deformed volume) and relies on the identification of a unique pattern in the material, which can be correlated between the two volumes [18]. Figure 4-2 is a schematic representation of the process in 2D. Within the reference volume each subvolume can be represented by the grey-level function $f(x, y, z)$ and the corresponding deformed state by the function $g(x + u, y + v, z + w)$, where (u, v, w) are the displacements mapping the reference volume to the deformed volume. The objective is to calculate the

displacement vector, which maps the reference and deformed subvolume. Continuity of grey-levels is assumed, such that:

$$\boldsymbol{f(x,y,z) = g(x+u, y+v, z+w)} \quad \textbf{(21)}$$

Figure 4-2 illustrates the technical process for subvolume matching between the reference and deformed image and subsequent displacement mapping. Each subvolume is commonly subjected to affine transformations (translation, rotation, shear) and a correlation algorithm is used to determine the peak subvolume match. The accuracy of the algorithm can be improved by employing an iterative multi-pass (also known as predictor-corrector) approach; from this the displacement vectors, and by differentiating with respect to position across the overall imaging volume, strain values can be calculated [131].

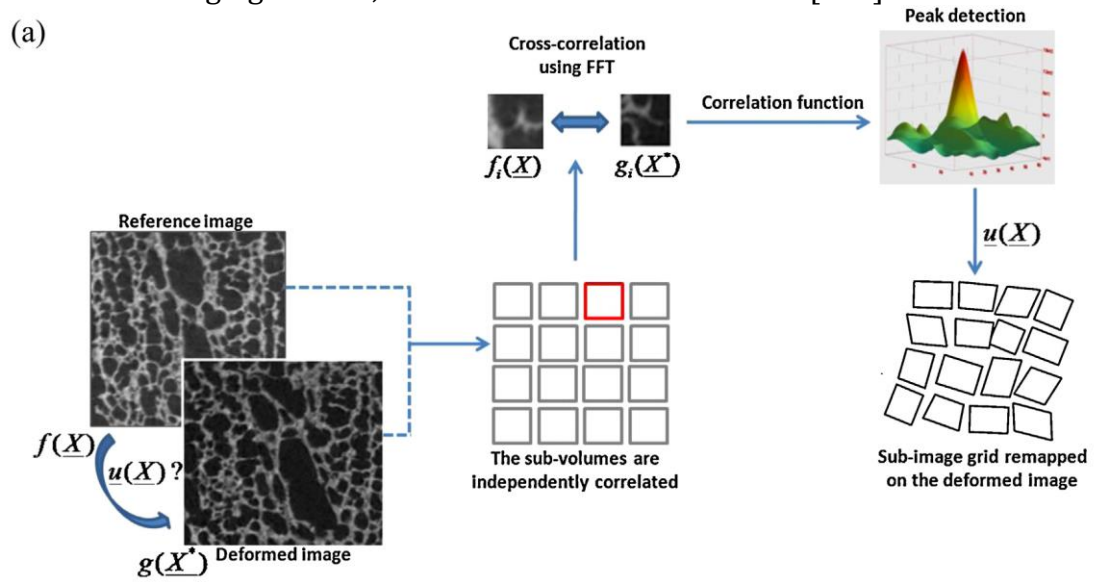

Figure 4-2: The image correlation subvolume mapping process which compares reference and deformed images [25].

The assumption in equation 1 makes no allowance for measurement uncertainty, which arises from inherent system noise and data acquisition/ reconstruction artefacts. Measurement uncertainty can be affected by the parameters chosen by the user. Subvolume size is possibly the most influential parameter in terms of measurement precision; it is essential that the selected subvolume size be large enough so that during the correlation process, there is a sufficiently unique intensity pattern, which can be distinguished from other subvolumes [83]. Jandejsek *et al.* [90] determined that above a certain subvolume size, significant improvements in displacement measurement where not observed but that strain resolution decreases. Smaller subsets, however, result in larger displacement measurement errors and a loss of displacement resolution. Other factors such as grid spacing [80, 91], correlation coefficient [20, 79], shape function [79, 81], voxel size and sample microstructure [20, 93] can all influence measurement error. Variations in the details of the implementation of DVC exist, although the framework on which it is built is consistent [18]. Correlation coefficients, shape functions and interpolation choices yield different uncertainty values and hence affect displacement and subsequent strain measurement. As introduced earlier,

when using DVC for the evaluation of localised strains in highly aligned FRP, the underlying anisotropy must be taken into consideration

4.4 Materials & Methods

4.4.1 Materials

A particle-toughened carbon fibre reinforced polymer was used for this study. The material was laid up in a $[0,90]_{2s}$ configuration and a double notched coupon geometry chosen for *in situ* tensile testing with corresponding dimensions: 66mm x 4mm x 1.6mm with semi-circular notch sections of radius 1.5mm either side of the centre of the coupon, as described in previous studies [62], and illustrated in Figure 4-3. This notch creates a nominal width at the specimen centre of ~1mm. Aluminium tabs were attached to allow uniaxial loading of the coupon which was carried out using a Deben CT5000 loading rig capable of applying loads up to 5 kN.

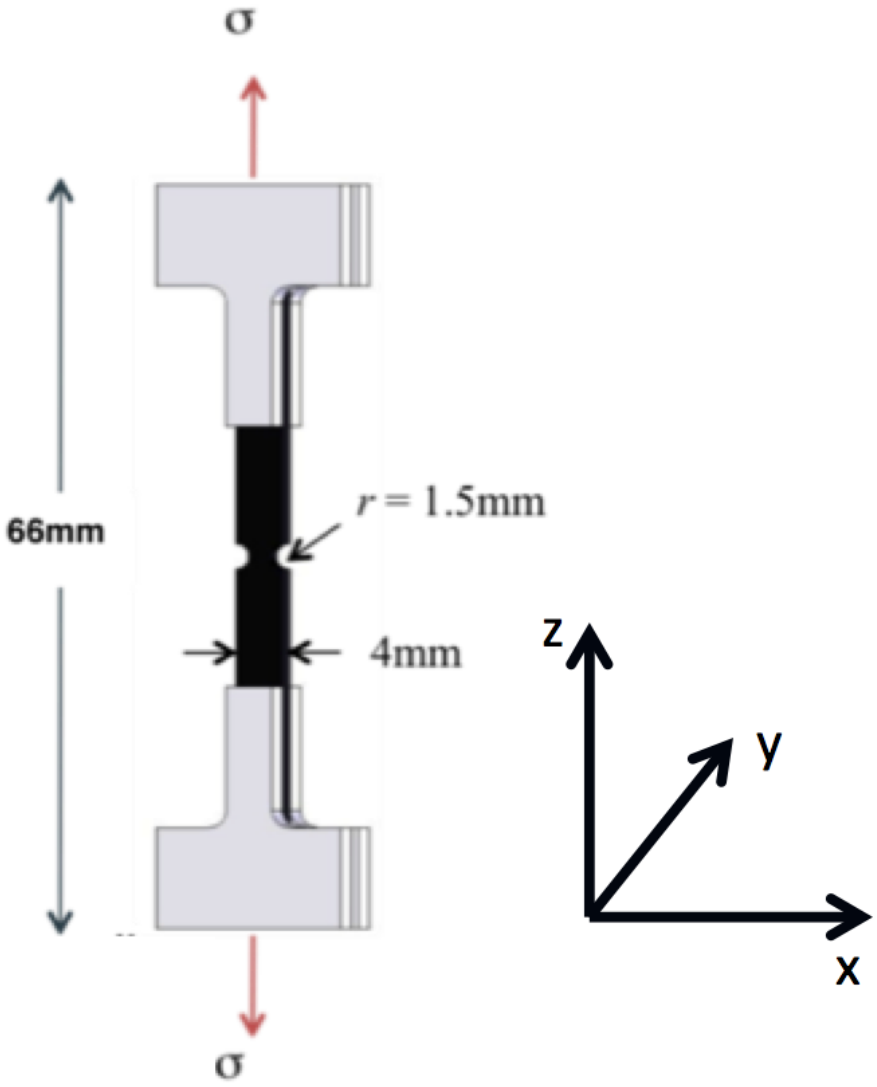

Figure 4-3: Coupon geometry and axis definition. Aluminium tabs are attached to the coupon to enable uniaxial loading.

4.4.2 Volumetric Scans

Volumetric scans of the particle toughened carbon-epoxy FRP used in this study were captured using synchrotron radiation computed tomography (SRCT) at the ID19 beam line of the European Synchrotron Research Facility (ESRF) in Grenoble, France.

The Deben loading rig was tilted at an angle (θ) of 20° relative to the path of the beam as shown in Figure 4-4.

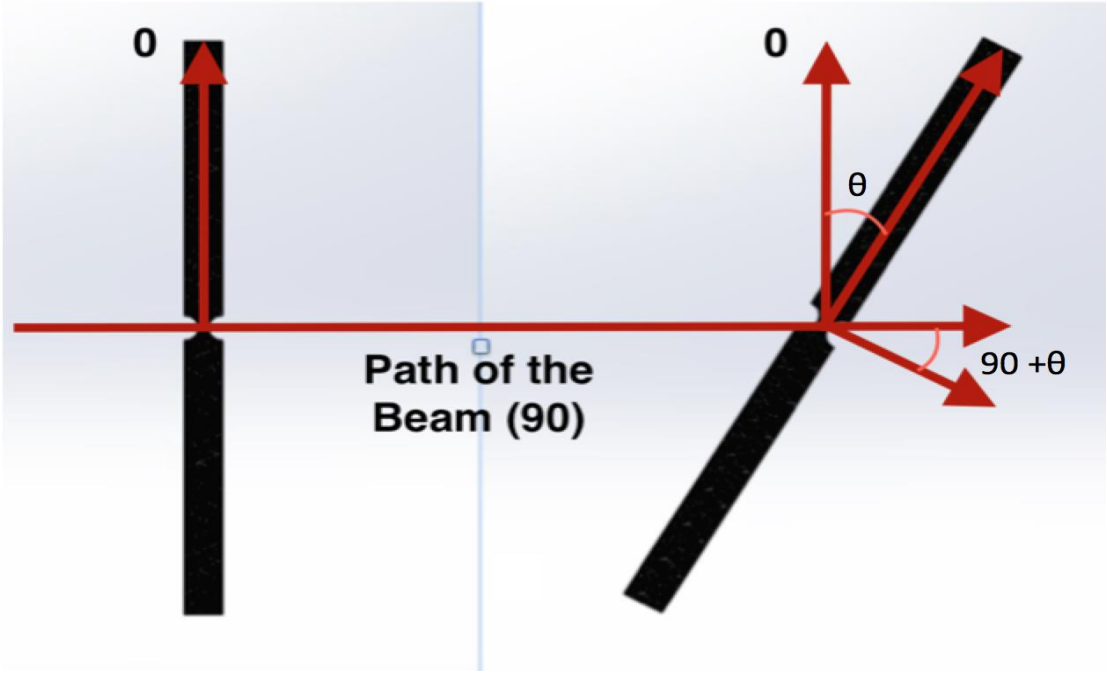

Figure 4-4:The coupon was tilted relative to the path of the beam to negate a phase artefact identified in the plies ordinarily parallel to the path of the beam

Previous work had identified a phase artefact in plies aligned parallel to the path of the beam (90° plies in the current work). It was shown that this could be countered by applying this tilt. Figure 4-5a shows the resolution of the fibre parallel to the path of the beam when the coupon is not tilted and Figure 4-5b shows the resolution when the fibres are tilted. It is clear that there is a significant improvement between the two images. The loading rig was tilted to ensure uniaxial loading was applied to the coupon.

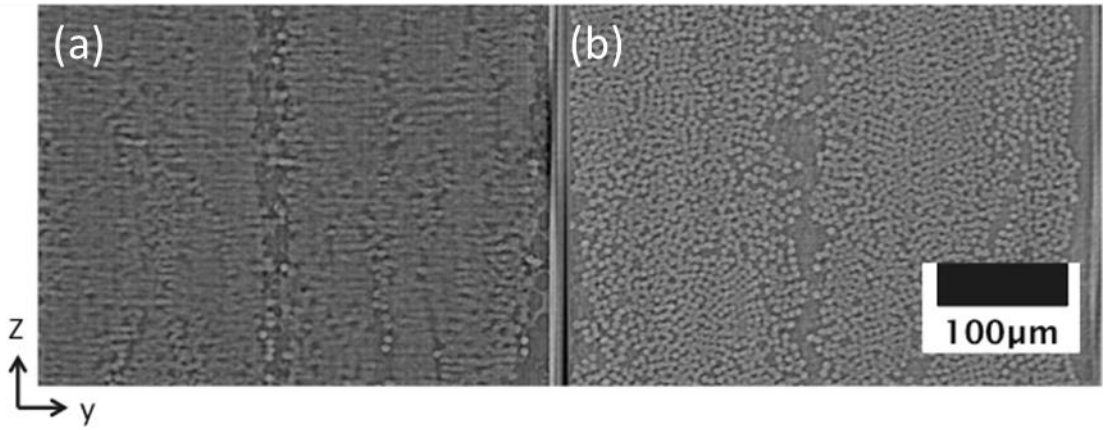

Figure 4-5: Comparison of the resolution of scans captured of the 90° plies in: a) the untilted coupon and b) the tilted coupon.

A detector size of 2560 x 2160 pixels was used, and scans were conducted at a beam energy of 19 keV and a voxel size of 0.65 µm. 2996 projections, with an exposure time of 20ms, were captured for each volumetric scan. After reconstruction, the bit depth of the volumes was reduced from a 32-bit to 8-bit format to facilitate faster DVC processing. As part of a larger study, coupons were subjected to incremental load steps to determine where damage might initiate in the 90° plies, see Table 4-1. At each load step a scan was captured.

Table 4-1: The load steps at which scans were conducted to capture early stage damage initiation events. The reference volume was captured at a small nominal holding load (10N) to ensure there was no sample movement.

UTS (MPa)	Load step 1 (%UTS)	Load step 2 (%UTS)	Load step 3 (%UTS)	Load step 4 (%UTS)	Load step 5 (%UTS)
1241	17.5	20	22.5	25	27.5

4.4.3 DVC

DVC analysis was conducted using DaVis LaVision software (LaVision Ltd., Goettingen, Germany). An initial study was conducted to assess the level of inherent noise by comparing two volumetric scans of the same unloaded, static coupon. The DVC algorithm is used to compare reference and deformed volumes with expected displacement & corresponding strain values of zero. Deviation away from zero is considered as being the result of system noise. As described in [79] and above, the subvolume size chosen to interrogate the Volumetric Region of Interest (VROI) has an effect on the uncertainty. As such, a subvolume size sensitivity analysis was conducted using subvolumes ranging from 20 voxels to 200 voxels using a 50% subvolume overlap with a multi-pass approach. Volumes were compared using each of the subvolume sizes and the standard deviation from a mean of zero was recorded for each of the six strain components. A volumetric map of the correlation coefficients obtained at this stage of the investigation indicates how well subvolumes are matched between the reference and deformed volumes. A rigid body motion study was furthermore conducted by comparing the volume captured for a simply displaced, but still unloaded coupon, with the prior reference volume. The fast Fourier transform (FFT) correlation approach was used, with tri-linear interpolation [81].

DIC was also assessed on single slice data (reference and deformed) taken from the volumetric scan of a region of interest, where slices were taken perpendicular to the fibre direction, and positions along the fibre matched manually to visible microstructural detailed; the results of this were then compared to DVC analysis.

The effect of mismatching volumes of interest along the fibre direction was investigated by assessing *apparent* strain measurements when a VROI is given a simple displacement (five-slice ~3.25μm) parallel to the fibre direction. Additionally, we have assessed potential improvements in DVC tracking of displacements along the fibre direction when sub-volumes have been specifically extended in the fibre direction (*i.e.* sub-volumes are themselves anisotropic), under the expectation that more structural variation may then be captured in this direction, facilitating improved displacement mapping.

Finally, as part of the validation, we present initial results on incremental damage progression: strain maps of the incremental load steps are presented to show the evolution of local strain under a series of load steps as transverse ply cracks initiate and grow.

4.5 Results

Using the FFT algorithm, correlation values of 0.92-0.97 between the two unloaded, static scans compared for the noise study, were recorded by the DVC algorithm. The results of the noise study are shown in Figure 4-6 with the components *xx*, *xy* and *xz* removed in the first instance, as the *x*-axis is the fibre direction and as previously discussed, measuring displacements along the fibre is made difficult by a lack of a unique pattern in planes containing this axis. On the basis of the behaviour in Figure 4-6, a sub-volume size of 80x80x80 voxels is identified as an 'optimum' for the purposes of this study. At this subvolume size the apparent strain resolution is of the order 0.045%. With a 50% overlap the spatial resolution is 26 μm.

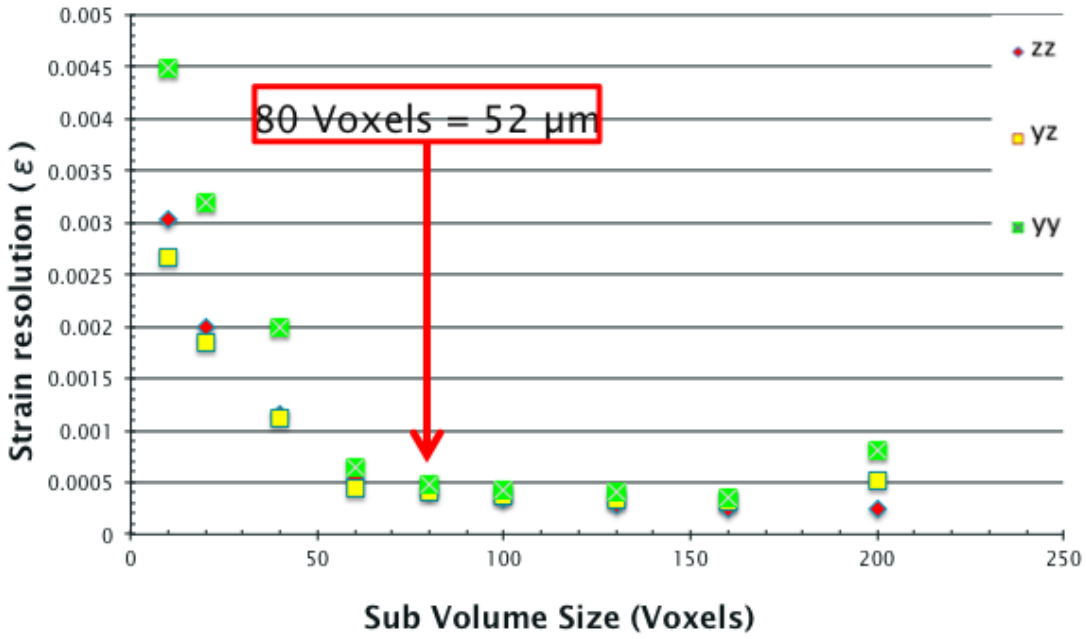

Figure 4-6: Results of the noise study, showing strain resolution vs subvolume size. A subvolume size of 80 voxels was chosen

Following the results of the rigid body motion study conducted, recorded in Table 4-2 it can be seen that the DVC algorithm is able to track displacements reasonably well in the direction orthogonal to the direction along the fibres: the apparent discrepancy in the measurement is consistent with error in the applied displacement due to mechanical variations, including an underestimation of the applied displacement due backlash of the actuator.

Table 4-2: The results of the rigid body motion body study

Displacement Direction	**Applied Nominal Displacement (µm)**	**DVC Displacement measurement (µm)**
z (Loading direction)	5	5.13±0.004
x (Fibre direction)	5	1.32±0.03

Using a subvolume size of 80x80x80 voxels, displacements in the fibre direction are not tracked accurately however, indicating a substantial under-representation of relative *x* direction displacements (by some 3.7µm for a 5µm applied displacement).

The results of the study conducted to compare the DVC and DIC technique, *i.e.* volumetric vs. single slice assessment of the same region of interest, are shown in Figure 4-7 a and b respectively. The magnitudes of the measured strain by the two techniques across the volume are comparable, (0.1%-0.8%). Similarities between the locations of higher strain exist but they are not in absolute agreement. Line 1-1 and 2-2, in Figure 4-7 a) and b) respectively, indicate the location of the interply region for reference. A grid has been placed over a

corresponding area of interest, and a bar graph, Figure 4-8, created to compare the strain values of the techniques over a small sample area. The strain values are taken from top to bottom and left to right of the grid.

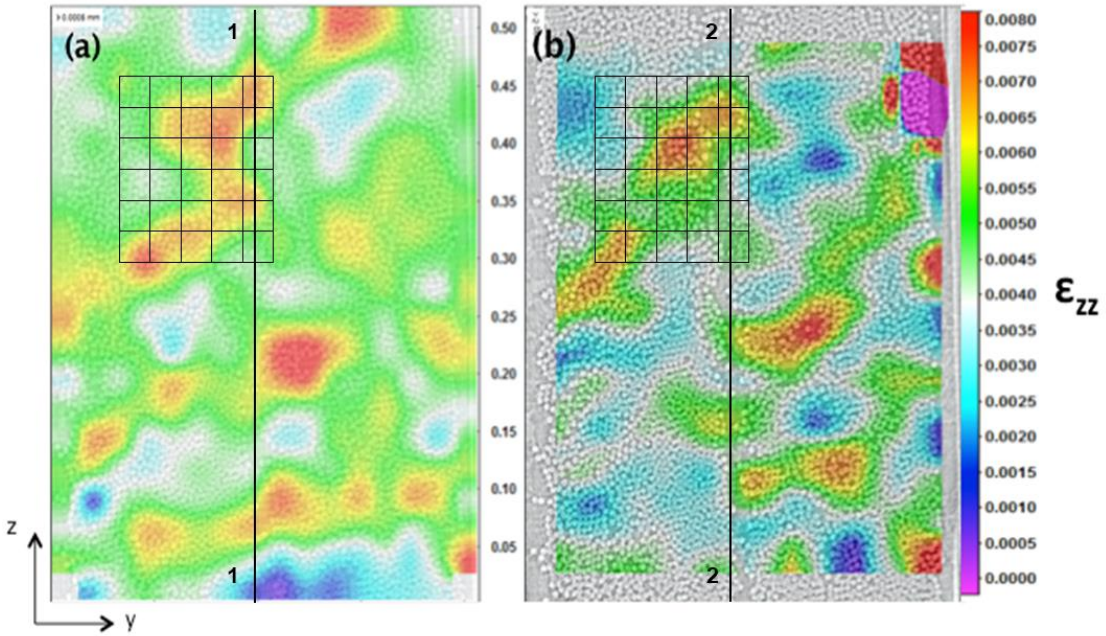

Figure 4-7 a) and b): The results of the comparison between the a) DVC and b) DIC approach in the 90° plies of a $[0,90]_{2s}$ coupon. The length scale is shown between images a) and b) (mm), the scale to the right of image b) is the key to strain the state over the images.

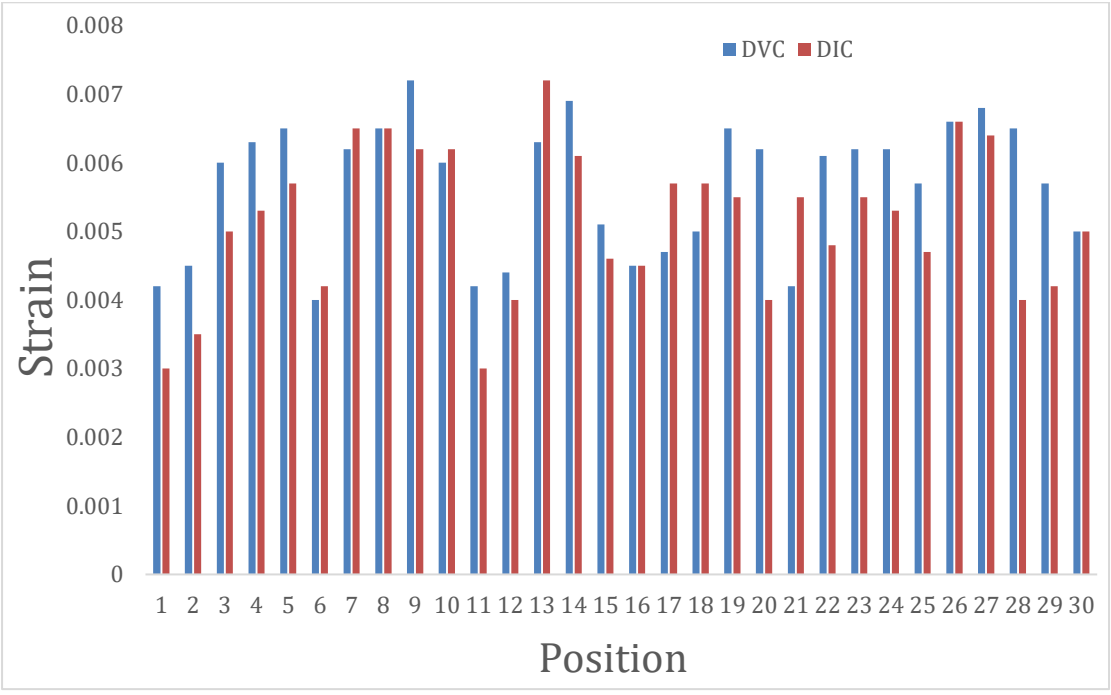

Figure 4-8: The comparison of strain over a small section of the DVC/ DIC comparison.

The comparison in Figure 4-8 highlights the difference in strain at each of the grid points for the three-dimensional and two-dimensional techniques. Bland Altman analysis of these results, Figure 4-9, reveal that the results of strains recorded by the DVC technique are systematically larger than those of the DIC technique.

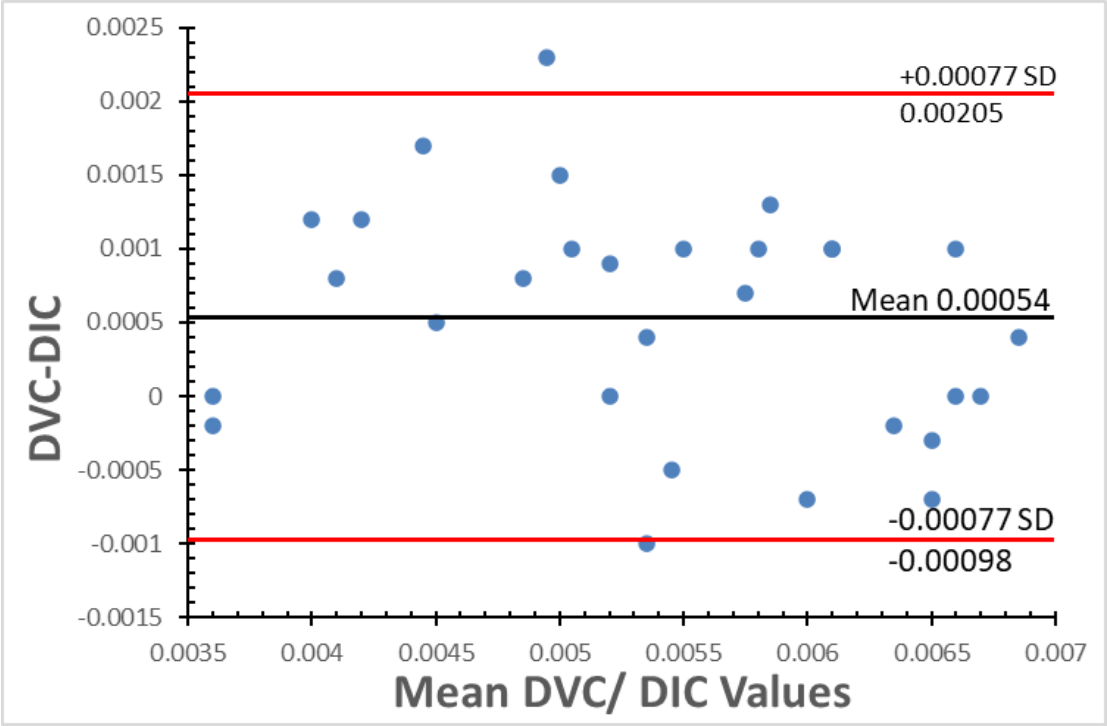

Figure 4-9: Bland Altman analysis of the DVC/ DIC technique comparison shows that DVC results are systematically larger than those of the DIC results.

This difference in the two techniques may be attributed to the strains determined using the DVC technique are based on additional information from a third dimension.

The results of the five-slice fibre-direction mismatch study are shown in Figure 4-10. Here the objective is to separate out the potential consequences of inaccurate sub-volume position determination in the fibre alignment direction (x) on *apparent* strains perpendicular to the fibres (i.e. z direction in this case). Here, the DVC analysis returned displacement values in all directions that were close to zero, *i.e.* correlation had not been achieved in the fibre direction.

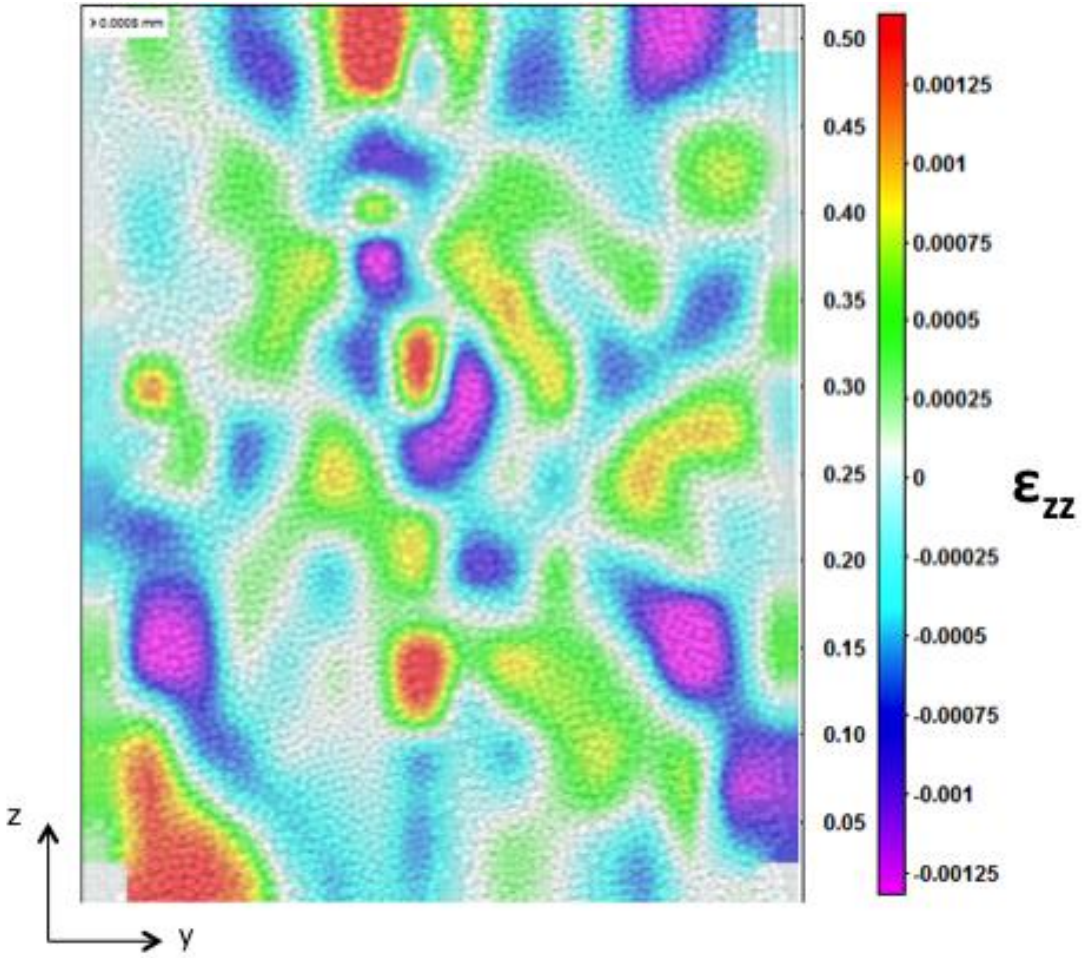

Figure 4-10: The results of the five-slice mismatch in the fibre direction (*x*) 90° plies in a $[0,90]_{2s}$ coupon. The length scale (mm) is shown to the immediate right of the image, the scale to the far right of the image is the key to strain state over the image.

From Figure 4-10 it is seen that for the selected isotropic sub-volume of 80x80x80 voxels, and the applied fibre-direction displacement of ~3.25µm (=5 voxels), strains are indicated that can only be attributed to poor correlation in the fibre direction (no other displacement or loading was taking place). For the imaging conditions here, the apparent strains in *z* direction yield peak values in the order of ±0.0012.

To illustrate the overall potential for strain measurement via DVC in conjunction with SRCT, Figure 4-11 shows the results of the SRCT investigation on a test specimen at three load steps. The volumetric region of interest (VROI) was cropped from the full scan and an edge detection algorithm was applied. The edge detection algorithm highlights image contrast, defined in [132]. Differentiation was used as this emphasises change. Once applied, adjusting the grey values highlights the edges in the volume. A median filter (noise reduction by replacing each pixel/ voxel with the median of the neighbouring voxel values – 3 voxel average in this case) was then used to remove outlier points. The result is a volume in which crack edges are highlighted; this volume of cracks can then be overlaid with the original volume thus identifying locations of initiation and propagation. Figure 4-11a, shows a SRCT cross section of a coupon loaded to 22.5% of the mean failure stress (UTS) for this material and specimen

configuration, with a small amount of damage evident. Figure 4-11 b and c are loaded to 25 and 27.5% of UTS respectively, highlighting a progression of damage as a fully developed transverse ply crack clearly appears between these load levels.

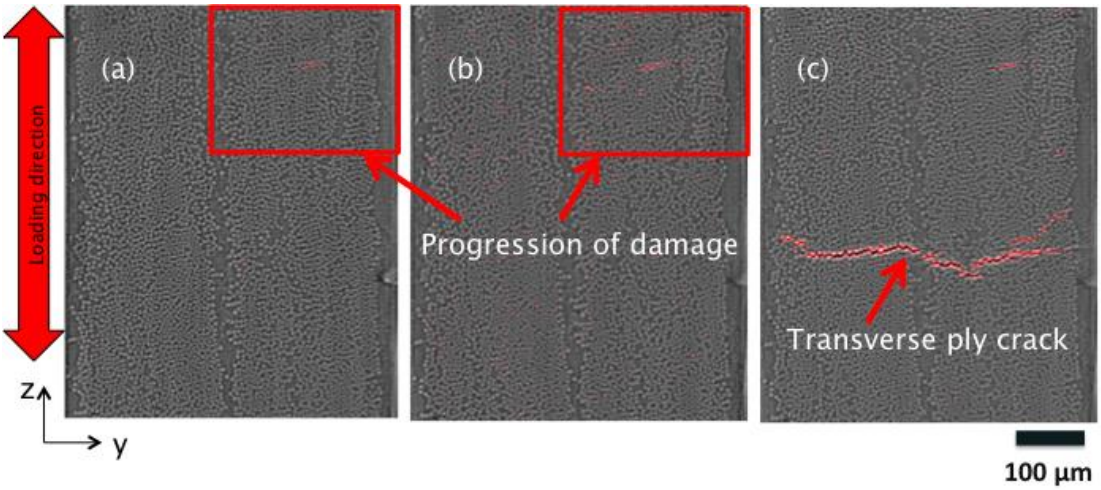

Figure 4-11: The progression of damage through load steps: a) 22.5% UTS, b) 25% UTS and c) 27.5% Damage is highlighted in red

Results of the DVC study near the surface of the notch where the cracks were identified are shown in Figure 4-12. Using the FFT algorithm with a subvolume size of 80x80x80, the progression of strains in the *z* (loading) direction, can be seen between the load steps a – c, at 15%, 22% and 25% of the UTS respectively.

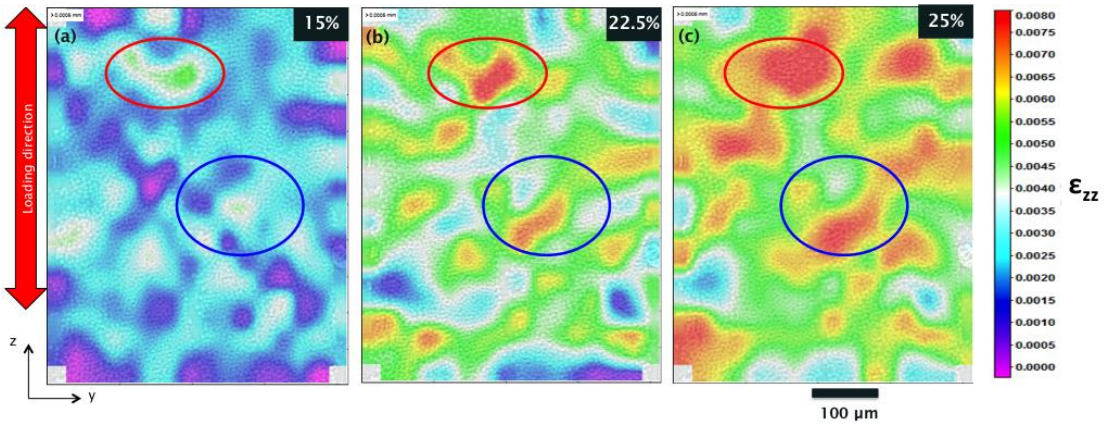

Figure 4-12: a-c. The progression of strain ahead of the fully developed transverse ply crack as measured using the DVC technique at increasing load steps. a) 15% UTS, b) 22.5% UTS, and c) 25% UTS which is the load step preceding a fully developed transverse ply crack.

It is seen that areas of higher strain identified in the earlier load steps are still prominent in the later load steps up to 25% UTS, two examples being highlighted in red and blue, the latter being the area in which the crack is found at the 27.5% UTS load step shown in Figure 4-11c. Interesting to note is the localised nature of the strains vary by a factor of ~ 3 between the highest and lowest strains in each of the load steps. The peak strains apparent at 25%UTS are significantly higher than the level of strain error due to fibre-direction mismatch indicated by Figure 4-10. Because this chapter is a validation of technique (images shown to demonstrate the DVC techniques ability to track strain as load steps progress),

no attempt to explain the reason behind the high strains in these regions is made. This will be handled in the next chapter.

4.6 Discussion

The ability of DVC to track the progression of strains at loads preceding fully developed crack damage is suggested by Figure 4-11. The strain peak magnitudes (of the order of 0.007 to 0.008) are significantly larger than the apparent strain artefacts from system noise (~0.00045) and induced fibre-direction mismatch (~0.0012). It is interesting to note the similarities in the strain maps generated by this study in Figure 4-10 and Figure 4-12 and those in the strain maps obtained by DIC on the surface of a transversely loaded glass fibre composite in the work of Canal *et al.* [32], see Figure 4-13. Canal *et al.* indicate that areas of higher compressive strain occur where the fibre volume fraction is lower. Areas of high strain (-0.026) such as that in the section the authors call "V1", are adjacent to areas of lower strain (-0.012), shown as V3, with a variation of strain between high and low that is just over a factor of two. Both studies show highly localised strains, over distances of ~20 μm equating to approximately 4-fibre diameters, and a factor in the order of two between the highest and lowest strains in the distribution. Canal *et al.* also suggest that areas of higher strain correlate with lower fibre volume fraction.

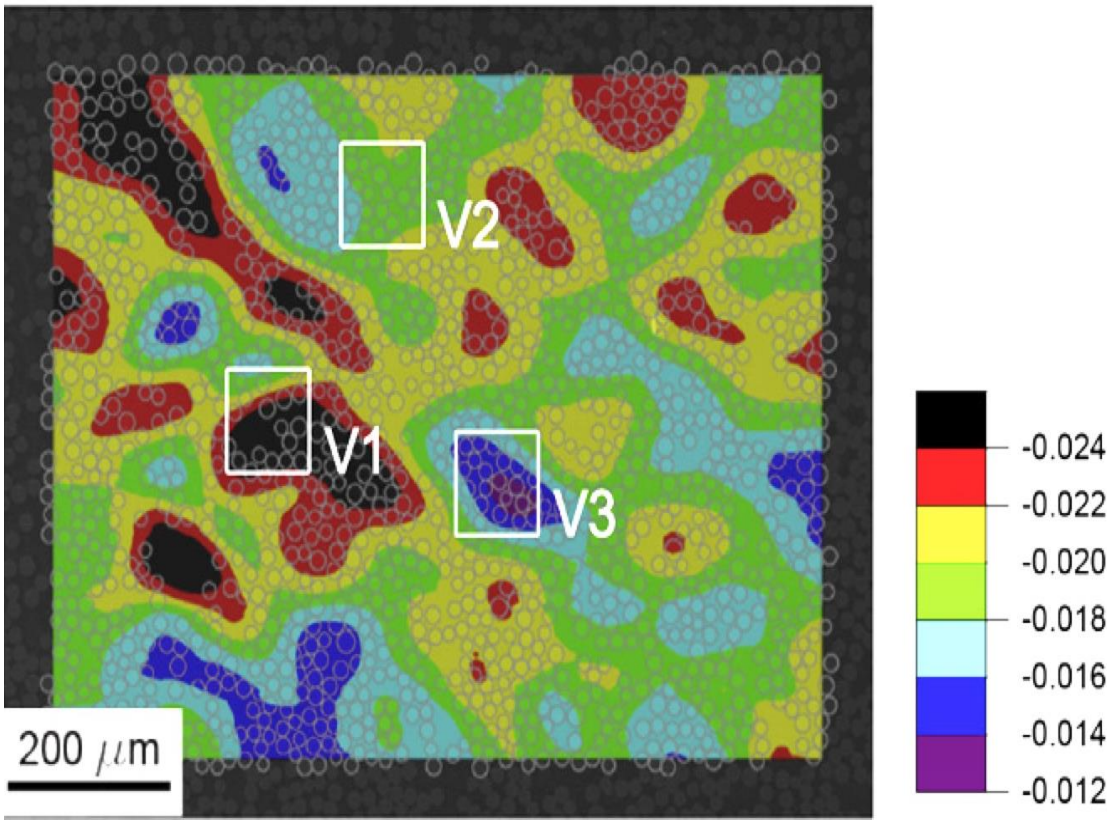

Figure 4-13:The results of an investigation conducted by Canal *et al* who use DIC on glass fibre reinforced polymer loaded in compression. "V1" represents an area of high strain in which the fibre volume fraction is lower to that in the surrounding areas such as "V2" and "V3" [32].

An important finding of the present work, observed in volumetric SRCT data and reinforced by the results of the induced fibre-direction mismatch analysis, is that although nominally straight, the fibres are, in fact slightly undulating along their

length; a result of the manufacturing process. Figure 4-14 is a schematic representation of the fibres in a unidirectional ply. Two cuboidal volumes, (a) and (b), whose *z* and *y* positions are nominally the same, represent volumes of interest to be cropped and used for DVC. The positions in the fibre direction (x) between the volumes are different (x and x+δ). The results of the two selections are shown in the figure depicting the *z* and *y* plane. The match between the two volumes appears to be fairly accurate, when viewed in this orientation, however where an individual wavy fibre has been included (shown in red), an apparent local displacement/strain arises between the volumes. In analysing induced fibre-direction displacements in otherwise identical volumes we identify apparent strains appreciably less than those measured up to the point of damage initiation. As such the load-induced strain mapping would appear to be reasonably meaningful. The fibre-direction displacements occurring under these load conditions are anticipated to be relatively small (*i.e.* uniaxial perpendicular to the fibres), however other loading modes (particularly shear) may be more problematic.

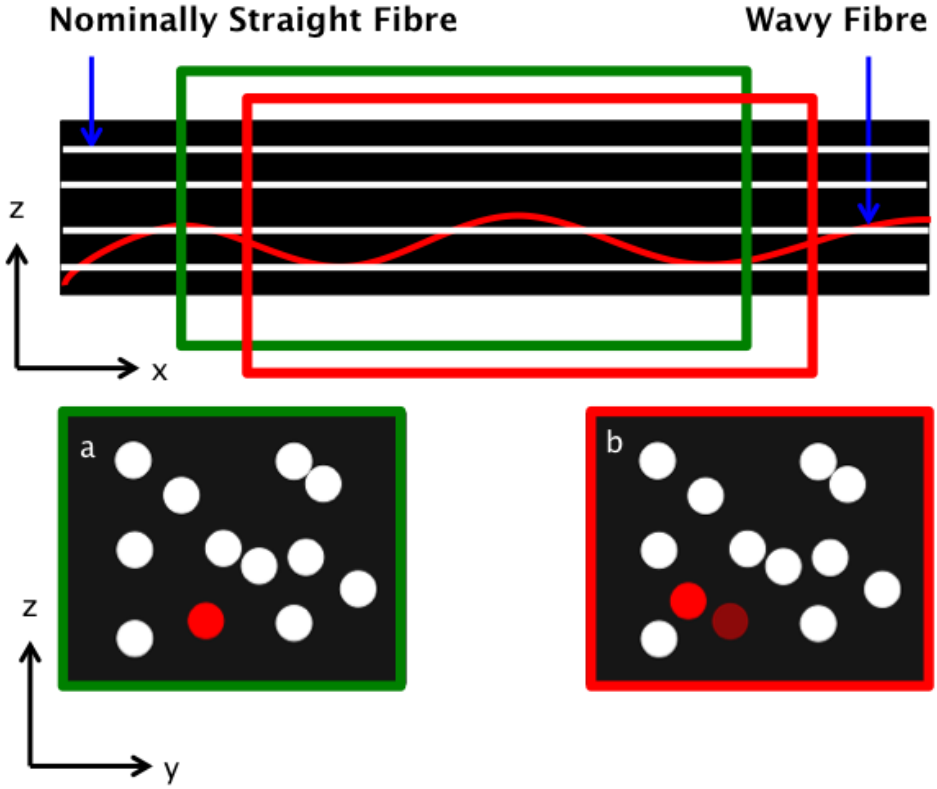

Figure 4-14: A representation of the fibres in a LFRP showing nominally straight fibres and a wavy fibre. Boxes a and b show the effect of mismatching volumes and fibre position. Boxes (a) in green and (b) in red shows end on fibres taken from the corresponding green and red boxes.

In considering fibre waviness, it can of course be envisaged as advantageous when comparing sub-volumes. Sufficient amounts of fibre waviness should provide contrast/structure along the nominal fibre direction to allow for accurate DVC correlation and reasonable displacement assessment in that direction. The results in Figure 4-10 show that the consequences of a five-pixel mismatch on the apparent *z* direction strain measurements are modest in this type of material. Given the presence of toughening particles, and other reference features, it is expected that z-direction registration of better than five pixels should be routinely achieved. However, to address this issue we identify that an

isotropic sub-volume size, extended in the fibre (x) direction may increase the number of unique identifiable features and assist the DVC displacement determination. To assess this, an artificial displacement of 6.5 µm has been tested along the fibre direction by selecting two volumes of the same size whose *z* and *y* coordinates were identical but whose *x* coordinate was chosen as ten slices along the fibre direction (*x*+10). The advantage of using an artificial displacement is that the effects of backlash in an unfamiliar actuator are removed. The study was conducted using an 80 x 80 subvolume in the *z* and y direction. The subvolume size in the *x* direction was then varied in increments of 80 voxels between 80 and 1200, see Figure 4-15.

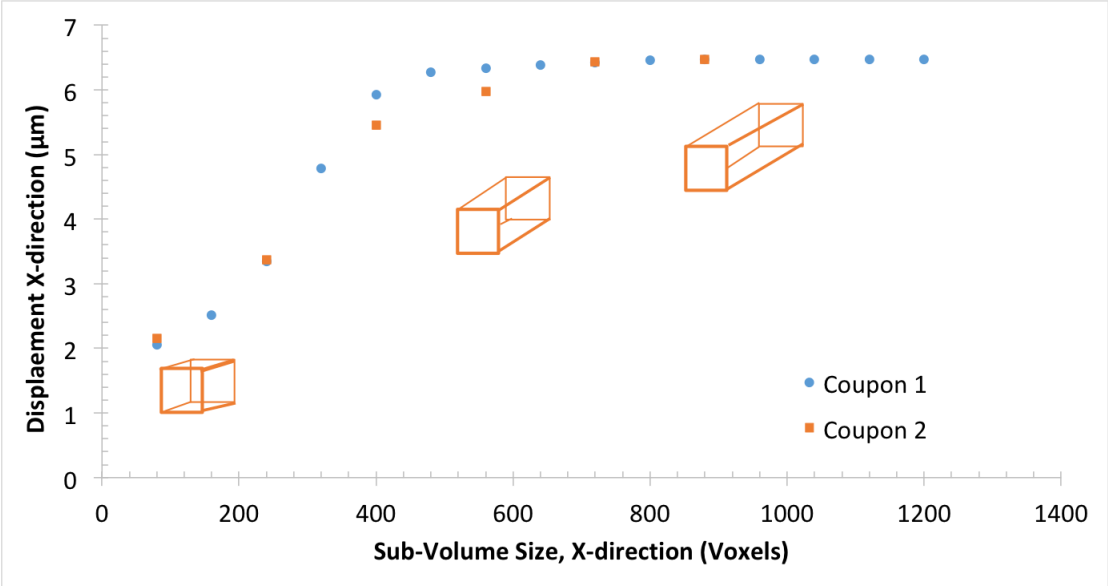

Figure 4-15: The results of the anisotropic sub-volume variation. At ~400 voxels in the x direction the DVC algorithm appears able to detect enough unique features to more accurately measure displacement along the fibre direction

From the graph, Figure 4-15, it can be observed that at a subvolume size of 80 voxels in the *x* direction, the actual displacement is indeed distinctly under-reported. The discrepancy is however ameliorated as the sub-volume size increases until a convergence at approximately 400 voxels, *i.e.* representing a sub-volume aspect ratio of ~5:1 in the fibre direction.

4.7 Conclusion

The work presented here represents a first development in the use of DVC for the identification of strains in the transverse plies of simple continuous fibre composites, using the only the native, sub-optimal microstructure. The verification studies conducted indicate that certain levels of confidence may be identified in detecting strain heterogeneity perpendicular to the fibres within a ply. The key to obtaining accurate results is accurate volume matching, especially in the fibre direction. However, allowance for degree of displacement mismatching in the fibre direction was not seen to compromise substantially the identification of transverse strain heterogeneity associated with crack initiation and propagation. Overall, the potential for this approach in obtaining volumetric strain distributions, at least in the planes transverse to the fibres appears to be

promising. Subsequent work will apply the technique to investigate damage initiation in composites under transverse loading.

5 Results Paper

The following was submitted to the journal of composites material (composites A) and form the results chapter of the current work. It was deemed that whilst the paper was well written, additional work was required in order for it to be including in the publication.

Local strain mapping and damage initiation identification by Synchrotron Radiation Computed Tomography and Digital Volume Correlation in a laminated carbon fibre polymer composite.

5.1 Abstract.

Synchrotron radiation computed tomography (SRCT) and digital volume correlation (DVC) are used in conjunction for the first time in an investigation of the strains preceding damage initiation in the form of transverse ply cracks in carbon fibre reinforced epoxy laminates. The formation of a transverse ply crack is shown to correlate with an extended region of elevated tensile strain, which exists at lower loads than that at which the transverse ply crack formed. The study indicates the value of the SRCT technique in determining where damage initiates and the relationship to local strain heterogeneity at initiation.

5.2 Introduction

The high specific stiffness and strength, manufacturing flexibility and customisable properties of fibre-reinforced composites means that they have evolved to become an increasingly common choice for weight-critical structural applications in aerospace applications, including for primary structures [1]. Most practical applications require a laminate with plies orientated in several orientations to reinforce against multi-axial primary loading and incidental transverse loads [2]. However, off-axis plies are susceptible to fibre/matrix debonding, matrix cracking and delamination, which contribute to failure of the lamina [3-6].

The growing use of carbon fibre composites has led to an inceased need for modelling techniques to predict performance. The validation of models for damage initiation is problematic due to the difficulties inherent in experimentally identifying and statistically quantifying small-scale damage events, such as scale, number and location/ environment of debonds and micro-cracks [47]. Furthermore, there is a major challenge to characterise the local stress or strain state that combines to cause damage initiation. As a result widely accepted models for damage initiation are yet to be established [7].

The use of high resolution computed tomography as a material investigation tool has seen widespread acceptance and growth over the last two decades with synchrotron radiation computed tomography ('SRCT') becoming instrumental in informing and developing modelling capabilities for composite materials [15, 16]. With achievable voxel resolutions now as low as a few tens of nanometres [64], the benefits of micro/nano-resolution SRCT as applied to CFRP include the

ability to test *in situ,* resolve individual fibres, toughening particles, microvoids and incipient damage processes [13, 15, 133-135].

In conjunction with direct three-dimensional visualisation and structural morphometry via SRCT, digital volume correlation (DVC), the three-dimensional extension of digital image correlation (DIC) has been shown to allow the measurement of displacements and strains at a microstructural scale in studies on a range of materials [16, 21, 136, 137]. By applying the DVC technique to CFRP's, the quantification of damage can be realised and measured displacement values may be used to define realistic boundary conditions for a region of interest. This, in combination with image-derived microstructural information, means that novel micromechanical models may be validated and realised at acceptable computational cost [25].

The aim of the current work is to combine SRCT with the DVC technique to identify initiation areas and the local strains in composite plies experiencing transverse loading. It builds on previous work [138] in which the DVC methodology itself was assessed.

5.3 DVC technique description

To recap on chapter 4, displacement is tracked between volume pairs (reference and deformed) by the DVC algorithm, the process is represented in Figure 5-1. The technique relies on a unique internal texture pattern within the material. The reference volume is divided into subvolumes, the sizes of which are user defined and depend on the volume and internal texture feature size. Each subvolume in the reference volume is represented by the grey level function $f(x, y, z)$ and in the corresponding deformed state by $g(x + u, y + v, z + w)$, where (u, v, w) are the displacements mapping the reference volume to the deformed volume. Comparison of the deformed and undeformed volumes enables calculation of the displacement vector, which maps the reference and deformed subvolume. Continuity of grey-levels is assumed, such that:

$$\boldsymbol{f(x, y, z) = g(x + u, y + v, z + w)} \quad \textbf{(22)}$$

The technical process for subvolume matching between the reference and deformed volumes and subsequent displacement mapping is shown in Figure 5-1

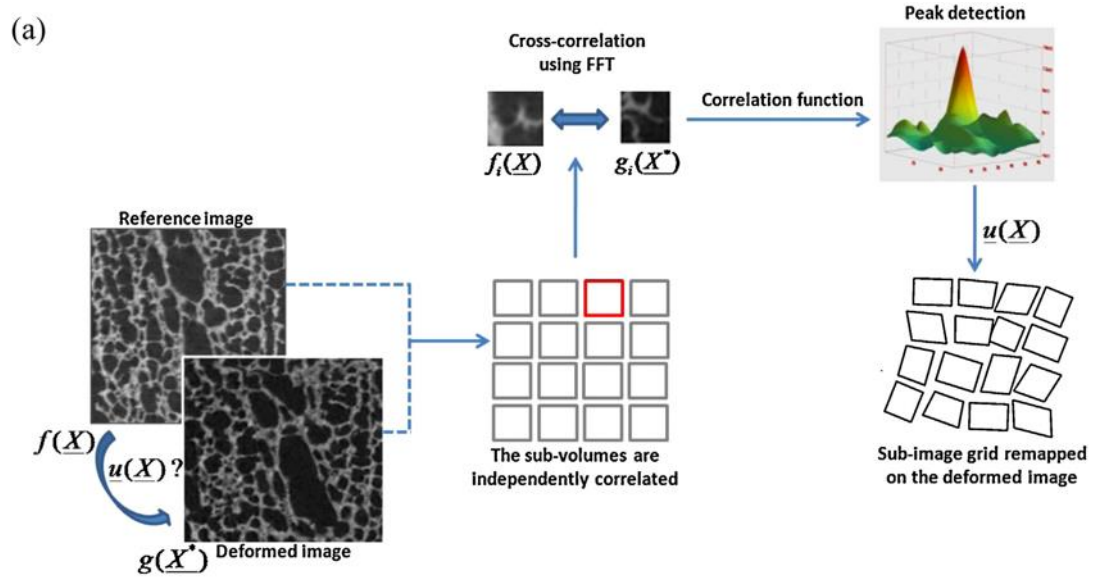

Figure 5-1: The DVC algorithm compares reference and deformed volumes in order to calculate displacement vectors [25].

Subvolumes are subjected to translation, rotation and shear movement and a correlation algorithm is used to determine peak subvolume match. The accuracy of the algorithm can be improved by employing an iterative multi-pass (predictor-corrector) approach; from this displacement vectors and subsequent strain values can be calculated.

5.4 Method

5.4.1 Materials

Two material systems were used in this study: particle toughened Toray T800s/3900-2 and the untoughened T800/3900 by the same manufacturer, both with a documented fibre volume fraction is 61% [65]. The materials were laid up in a $[0,90]_{2s}$ configuration and a double notched coupon geometry chosen for *in situ* tensile testing was 66mm x 4mm x 1.6mm with semi-circular notch section of radius 1.5mm either side of the centre of the coupon, as described in previous studies [62], and shown in Figure 5-2. This notch creates a nominal width at the centre of ~1mm. *Ex situ* tensile testing was conducted using a standard Instron electro-mechanical test machine with a 50 kN capacity load cell to determine the average failure load for this material and specimen configuration.

For the *in situ* testing, conducted using SRCT, aluminium tabs were attached to the coupons to allow loading in a Deben CT5000 loading rig capable of maintaining loads up to 5kN.

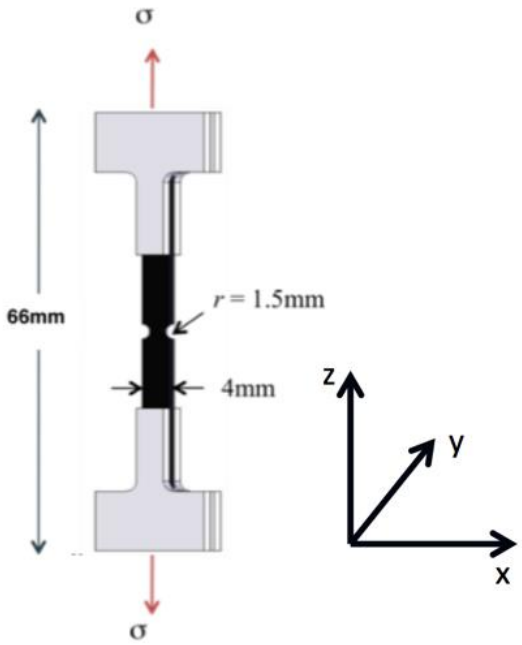

Figure 5-2: The coupon geometry including the aluminium tabs and axis definition [62].

5.4.2 Volumetric Scans

SRCT was used to obtain volumetric scans of the CFRP, captured at the ID19 beamline at the European Synchrotron Research Facility (ESRF) in Grenoble, France. A detector size of 2560 x 2160 pixels was used and scans were conducted at a beam energy of 19 keV and a voxel size of 0.65 μm. 2996 projections, with an exposure time of 20ms, were captured for each volumetric scan.

Coupons were subjected to six incremental load steps, calculated as a percentage of the specimen's nominal tensile strength, to determine where, and at what load damage initiation events occurred in the 90° plies. At each load step a CT scan was captured. After reconstruction, the bit depth of the volumes was reduced from a 32-bit format to 8-bit to improve DVC processing times.

Cracks were identified in the volumes captured at higher load steps and these locations became the volumetric region of interest (VROI) for investigation at the lower load steps – before crack initiation. The VROI was cropped from the full scan and an edge detection algorithm was applied. The edge detection algorithm highlights image contrast, defined in [132] , see Figure 5-3.

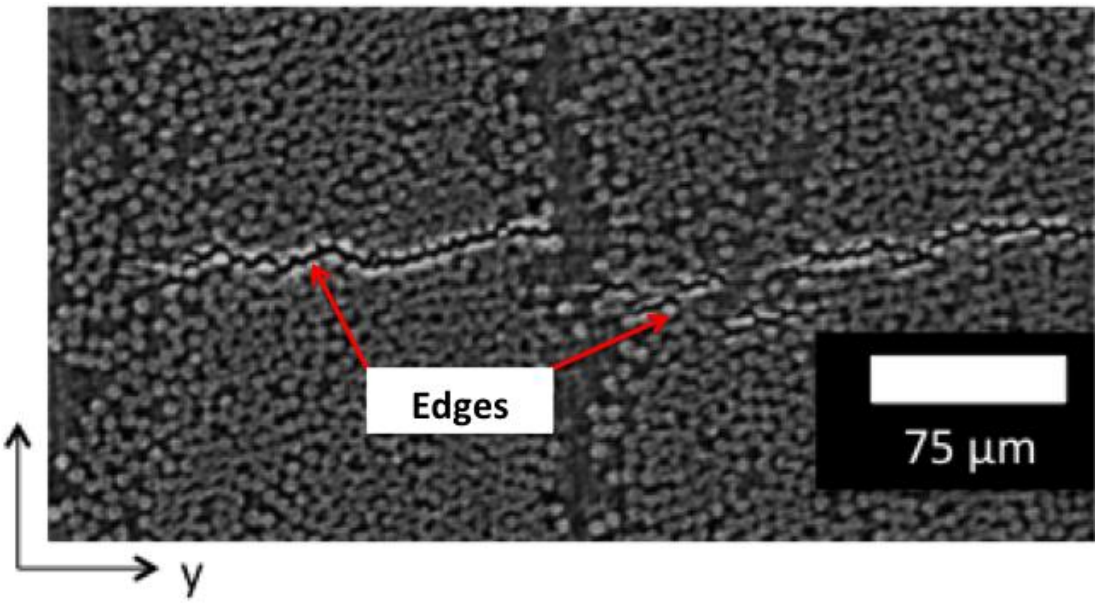

Figure 5-3: The difference in intensitydue to phase contrast (near-field Fresnel/edge detection regime) between the edge of the crack and surrounding material in the T800s/3900-2

Differentiation was used as this emphasises change. Once applied, adjusting the grey values highlights the edges in the volume. A median filter (noise reduction by replacing each pixel/ voxel with the median of the neighbouring voxel values) was then used to remove outlier points. The result is a volume in which crack edges are highlighted; this volume of cracks can then be overlaid with the original volume thus identifying locations of initiation and propagation.

5.4.3 DVC

DVC analysis was conducted using DaVis LaVision software (LaVision Ltd., Goettingen, Germany), implementing a Fast Fourier Transformation (FFT) approach to estimate local displacements. A DVC noise and validation study was conducted. An initial study was conducted to assess the level of inherent noise by comparing two nominally identical, repeated volumetric scans of the unloaded, static coupon. Details of the noise study and subsequent technique validation for the use in identifying strains in unidirectional CFRP is presented in [138]. In summary a subvolume size of 80x80x80 voxels is used with a 50% overlap. DVC was used to compare scans of loaded volumes with the unloaded volumes.

5.5 Results

Figure 5-4 shows the results of a full volumetric scan of a particle toughened coupon at 27.5% of the UTS. The data has undergone post-processing grey level manipulation, highlighting the fibres, so that the different plies are evident. The image shows the curved face created by the notch (right-hand side of image).

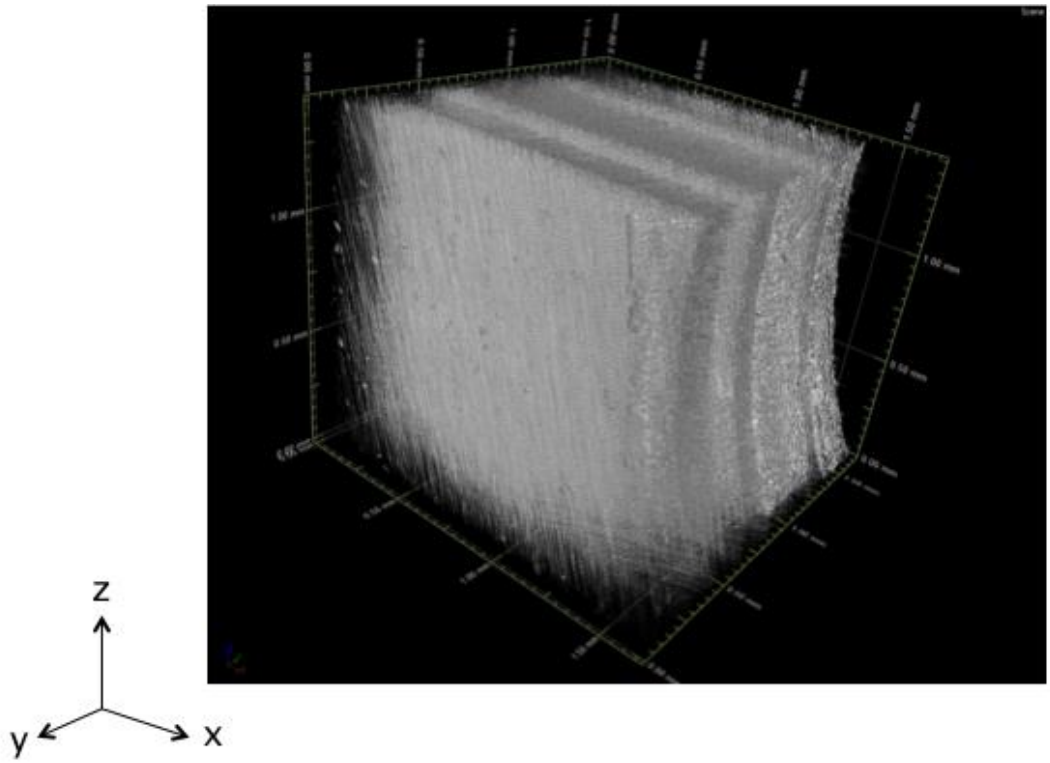

Figure 5-4: Segmented image of the T800s/3900-2 material showing the volumetric nature of the SRCT technique (notch surface seen on right-hand side). The volumetric scan has been segmented to show the fibres

Figure 5-5 the same volume after further manipulation to reveal the volumetric crack damage, which is well developed at this load step, occurring within several of the 90˚ plies.

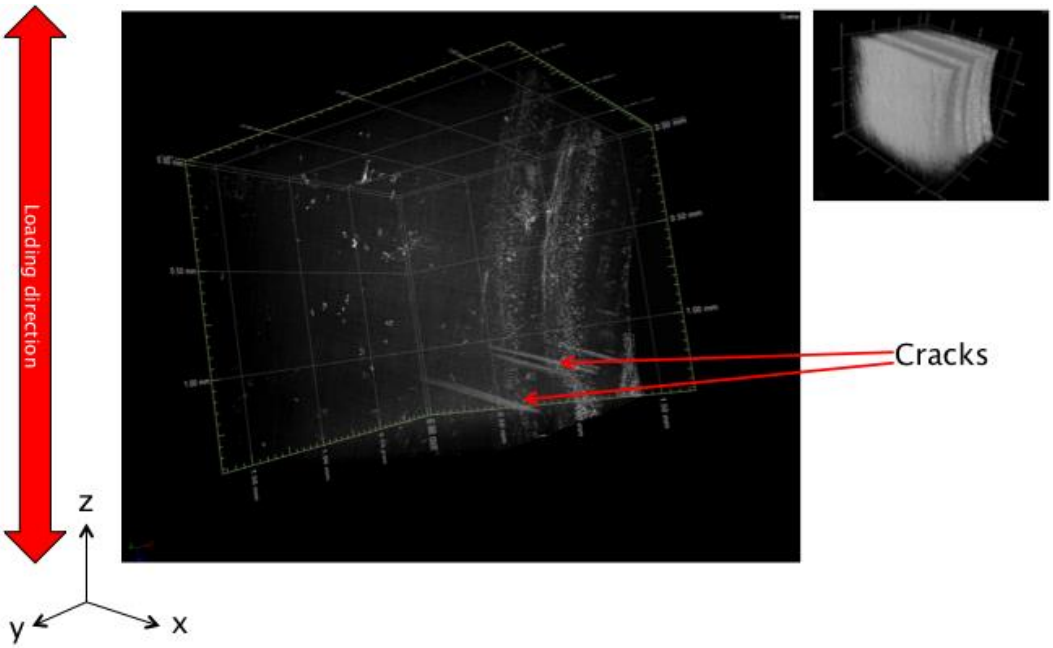

Figure 5-5: Further segmentation (of air gaps) of the volumetric image revealed cracks in the transverse plies

The edge detection algorithm described earlier highlighted cracks in the samples at the notch surface at 27.5% UTS. Figure 5-6 shows a region of interest in cross-section in which a complex crack initiated and developed across neighbouring transverse plies.

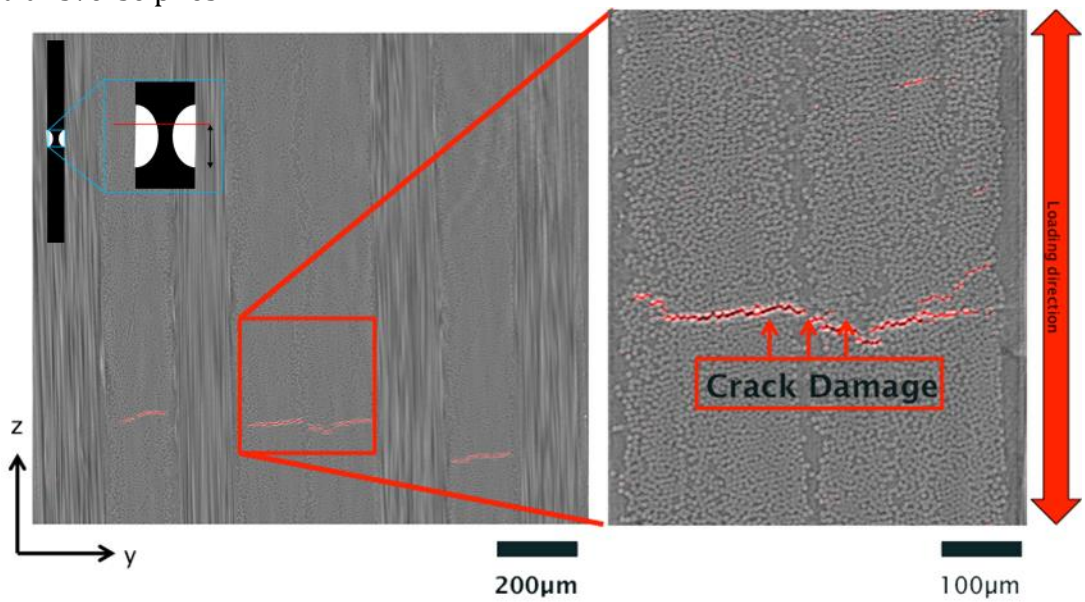

Figure 5-6: A transverse ply crack developed in the T800s/3900-2 at 27.5% load step, identified with the volume of interest for the lower load step, pre crack initiation. Damage occurred 2/3 of the way up the notch for this layup $[0,90]_{2s}$

Damage was found to occur 2/3 of the way up the notch for this layup $[0,90]_{2s}$ as indicated.

This region of interest was identified, retrospectively, in the lower load steps and the edge detection algorithm applied. Figure 5-7 c shows the fully developed transverse ply crack at 27.5 % UTS which has formed between 25 and 27.5% UTS. At the lower load steps, Figure 5-7 a and b, the large transverse ply crack is not evident. A small area of damage can be observed in the top right-hand corner of the images at these load steps.

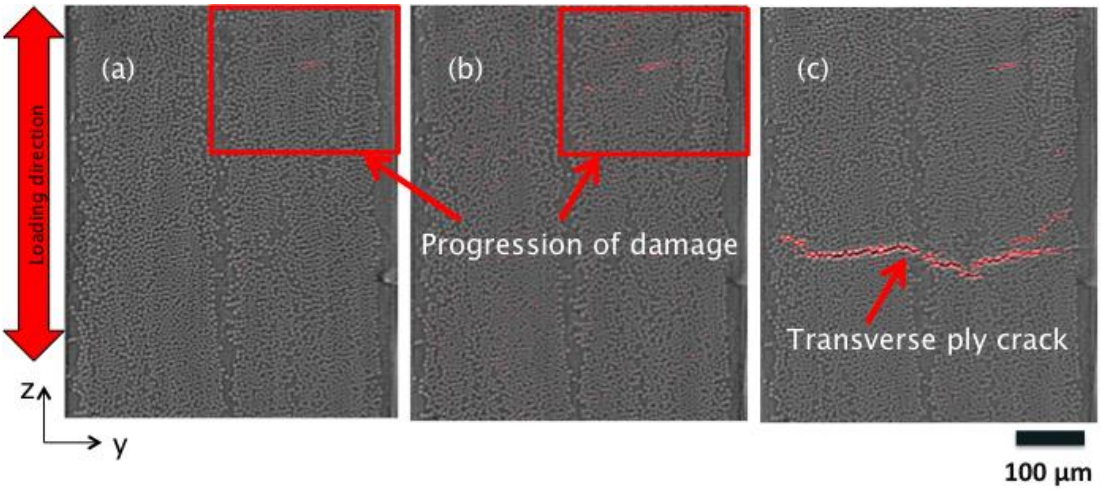

Figure 5-7 (a-c): The region of interest in the T800s/3900-2 material at (a) 15%, (b) 25% and (c) 27.5% of the measured tensile strength

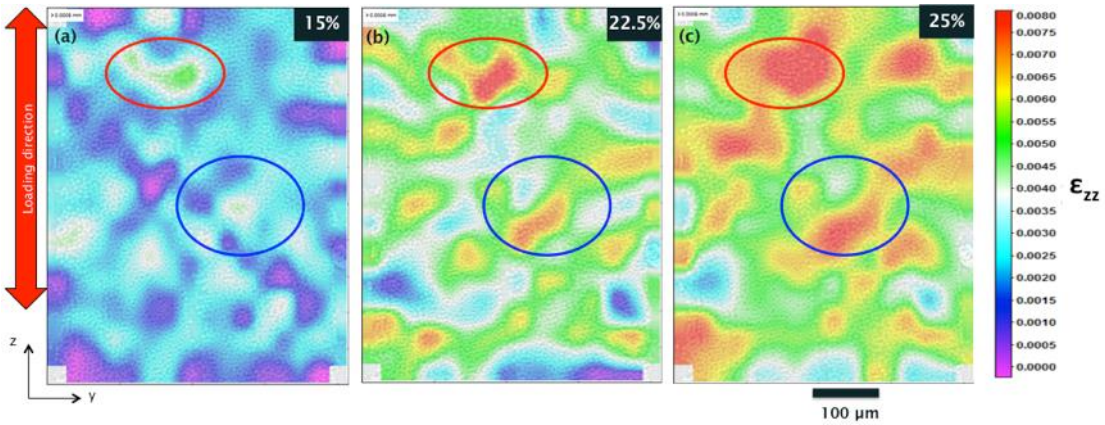

Figure 5-8 (a-c): The progression of damage in the toughened T800s/3900-2 material as measured by DVC as the load steps are increased. (a) 15%, (b) 22.5%, (c) 25% and (d) 27.5%. The VROI at each load step is compared to the corresponding unloaded volume to create the resulting strain map

Figure 5-8 a-c show DVC results at the notch surface for the toughened material, at the plane/region corresponding to Figure 5-7. Load step analysis from 15% to 25% UTS shows the progression of the distribution of strain. The areas of strain seen at the lower load steps are reasonably consistent across the higher load steps, indicated by red and blue ovals on the figure at each load step. The transverse ply crack was fully developed at 27.5% of the UTS.

Figure 5-9 a and b similarly show a region of an untoughened CFRP specimen loaded up to 20% UTS, at which point damage had fully developed. Load steps were obtained for 10, 12, 15 17 and 20% UTS, with Figure 5-9 showing the damaged state at 20%, and the representative undamaged state at 17%.

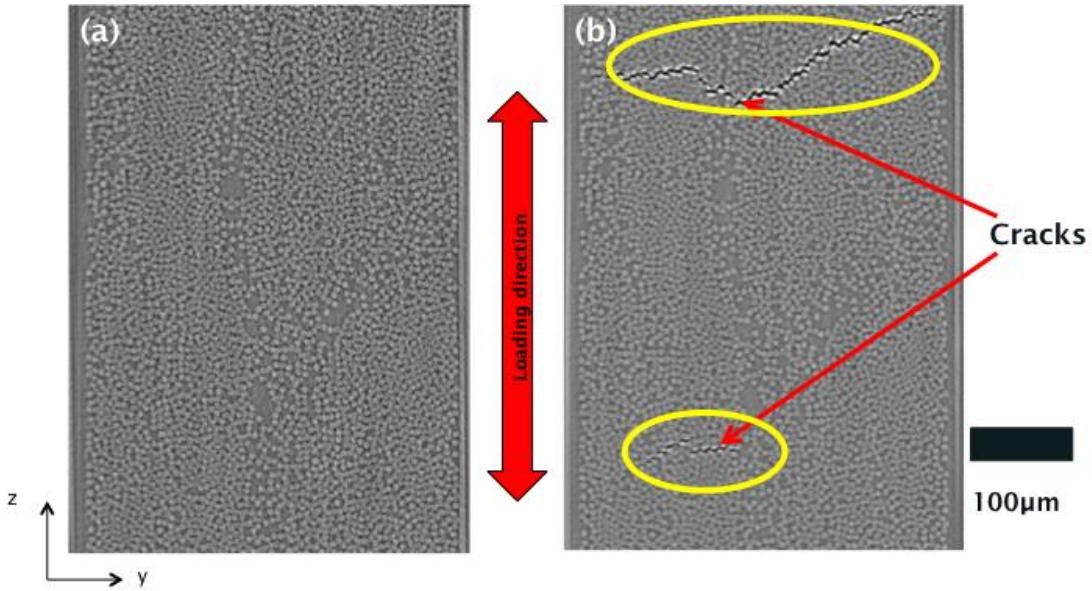

Figure 5-9 (a-b): The identification of damage in the untoughened T800s/3900 material, apparently undamaged (17% UTS loaded) and cracked at 20% UTS respectively.

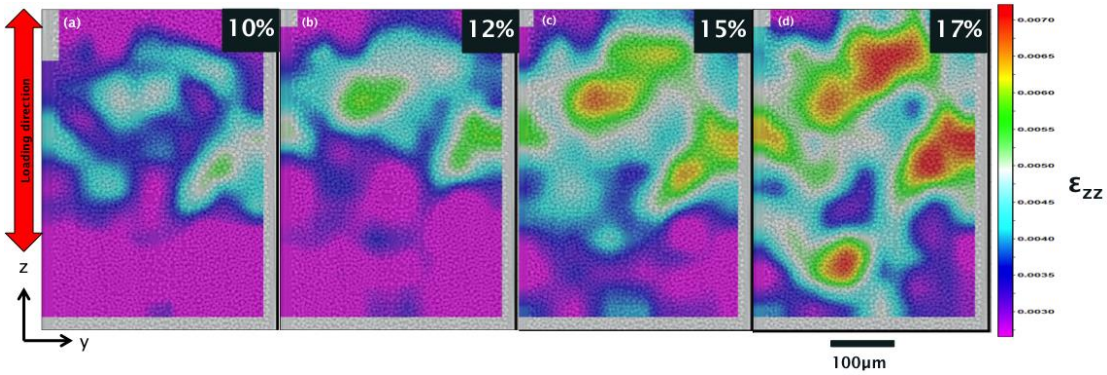

Figure 5-10 (a-d): The progression of damage as measured by DVC analysis in the untoughened T800s/3900 material from 10% UTS to 17% UTS.

Figure 5-10 (a-d) show the progression of the strain distribution as the load is applied to the untoughened system from 10%-17% of the UTS. At 20% the transverse ply crack shown in Figure 5-9 (b) was fully developed.

5.6 Discussion

Synchrotron Radiation Computed Tomography technique in conjunction with post processing imaging techniques has been shown to be effective in the identification of early stage damage formation in CFRP. Figure 5-11 further illustrates the 3-D morphology of cracks propagating into the material bulk, showing the toughened material, where a major transverse crack is apparently made up of several distinct sub-planes, presumably as damage tracks the local variations in fibre distribution and slight misorientations into the bulk. For the data available, it is evident, that damage initiates at a significantly lower percentage of UTS in the untoughened system. The DVC strain maps captured near the surface of the notch show a number of locations of high strain before the transverse ply cracks have developed - in Figure 5-10 for example two high strain region map to subsequent initiation sites, whilst in Figure 5-9 it is less definitive, with the one crack that fully traverses the ply being coincident with a

larger strain concentration site. The volumetric nature of DVC, combined with the 3-D imaging capability of SRCT, means that a subsurface investigation is possible and potentially useful in determining why damage occurs at one location over another. Figure 5-12 specifically shows the subsurface tensile strain, ε_{zz}, in the toughened material, at depths into the material 200 µm and 400 µm from the notch surface, at the load step before the major transverse ply crack is fully developed (at 25% of UTS).

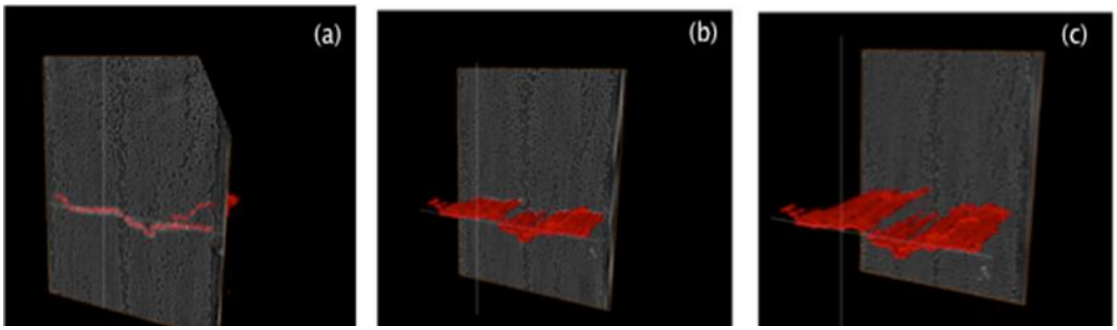

Figure 5-11 (a-c): A volumetric view of a fully developed transverse ply crack in the particle toughened T800s/3900-2 material.

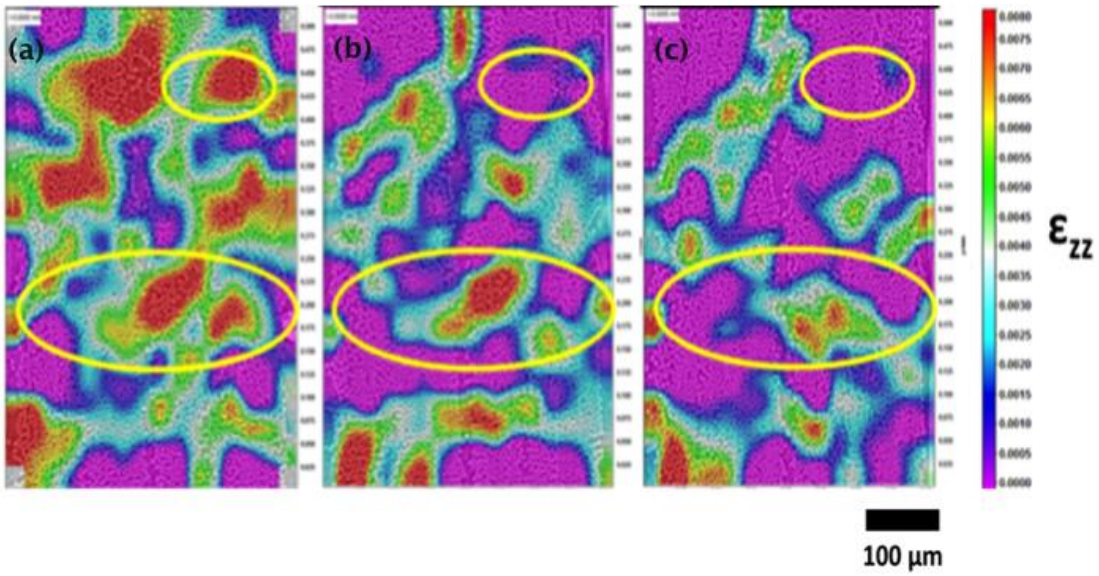

Figure 5-12 (a-c): The subsurface strain in the particle toughened T800s/3900-2 at 25% load, showing the local strains at (a) the surface, x=0 µm, (b) x=200 µm and (c) x=400 µm

Figure 5-12 a shows the strain in a toughened material specimen at the surface, x=0 at 25% UTS , Figure 5-12 b shows the comparable damage and strain at x=200 µm and Figure 5-12 c shows the damage and strain at x=400 µm. It is evident at x=200 µm and subsequently at x=400 µm that the area of relatively high strain, apparent at x=0 µm persists over the area/volume over which the major transverse ply crack subsequently occurs, although the magnitude and area decreases at distances further from the specimen surface. It is implied that significant crack initiation sites are controlled by micromechanical processes at these length scales, *viz* high strain regions in the order 50-100µm in the plane perpendicular to the fibres, and several 100's of µm in the direction of the fibres,

with the crack path correlating with the extended regions of apparent higher volumetric strain.

Whilst Figure 5-12 shows some indication that a DVC-determined high strain region penetrating into the sample bulk correlated with sites of major transverse damage, the situation is indeed complicated by a complex pattern of apparent local strain distribution. Figure 5-13 below illustrates similar findings for a second coupon of the same material, where a single main cracking event is seen (in slice images), appearing at 22% of UTS.

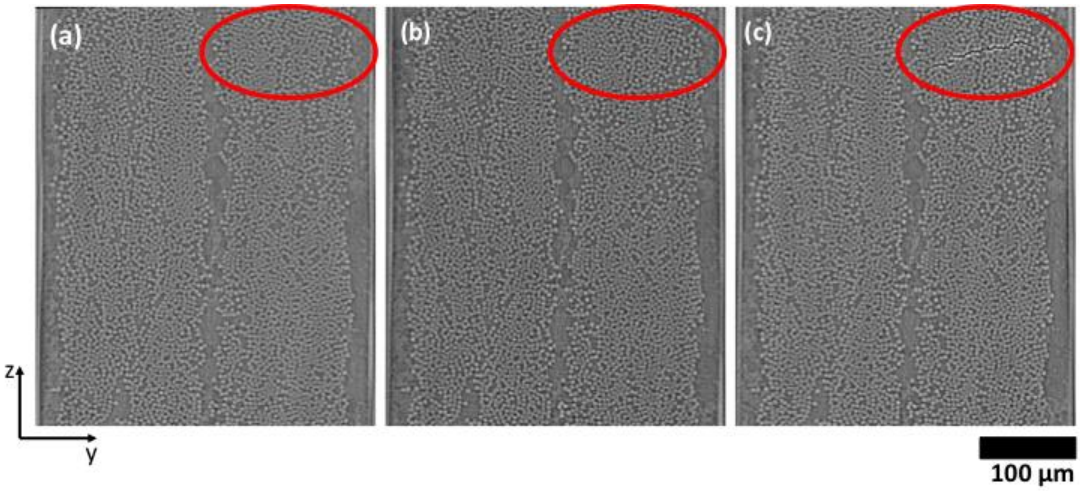

Figure 5-13 (a-c): Example two taken from the toughened material shows the CT images of damage progression through load steps from 17.5, 20 and 22% UTS.

The corresponding strain maps Figure 5-14 indicate that in this case there was a more distinct dominant large peak in strain that penetrated into the sample bulk, coincident with the site where crack initiation subsequently occurred.

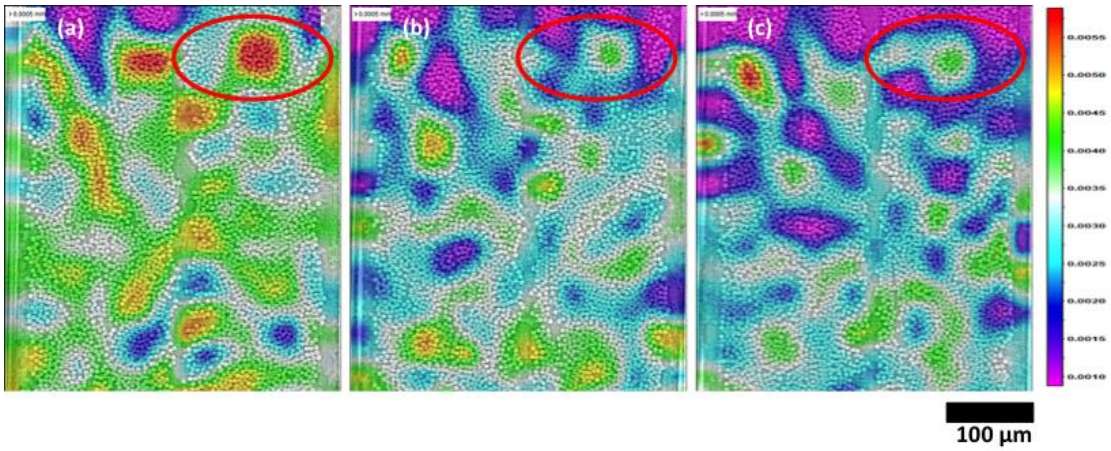

Figure 5-14 (a-c): DVC analysis of the coupon at 20% UTS at the surface x=0 µm, x=200 µm and x=400 µm respectively.

Figure 5-15 illustrates a further cracking event in the toughened material, where a singular initiation event is absent at 23% of UTS Figure 5-15 (a), and is clearly formed at 24% of UTS Figure 5-15 (b)..

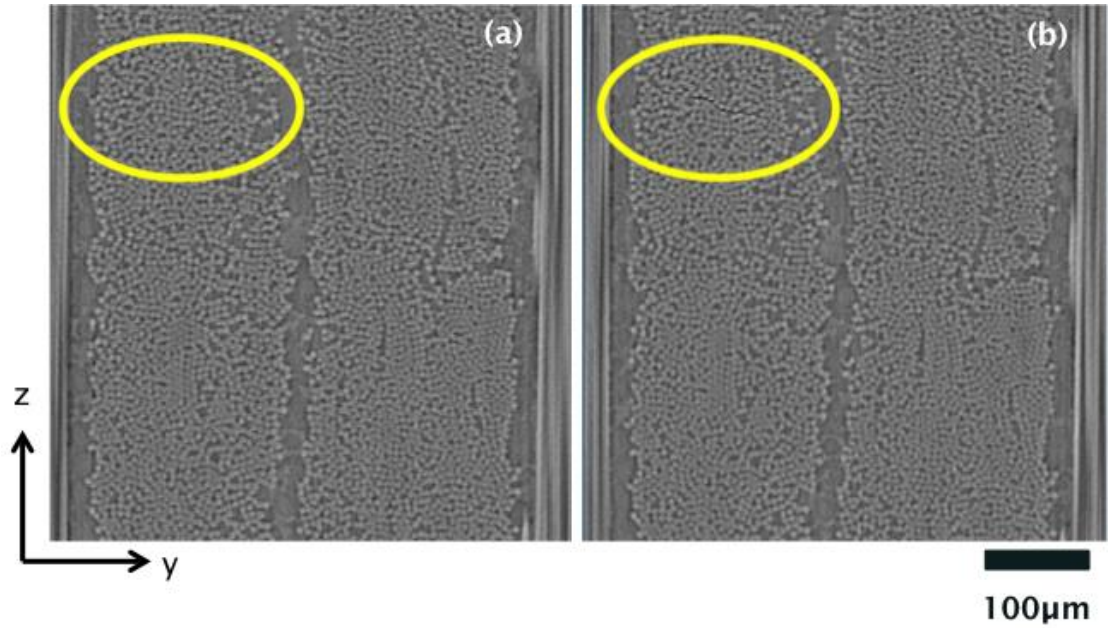

Figure 5-15: (a –b) Damage in this example occurs at 24% UTS (b), at the previous load step, shown in (a), 23% UTS the damage is not yet observable by visible inspection.

Corresponding DVC assessment at 23% of UTS shows a local strain peak (at x=0 µm) that penetrates into the bulk (at x=200 µm), coincident with the apparent initiation site, Figure 5-16 a and b respectively.

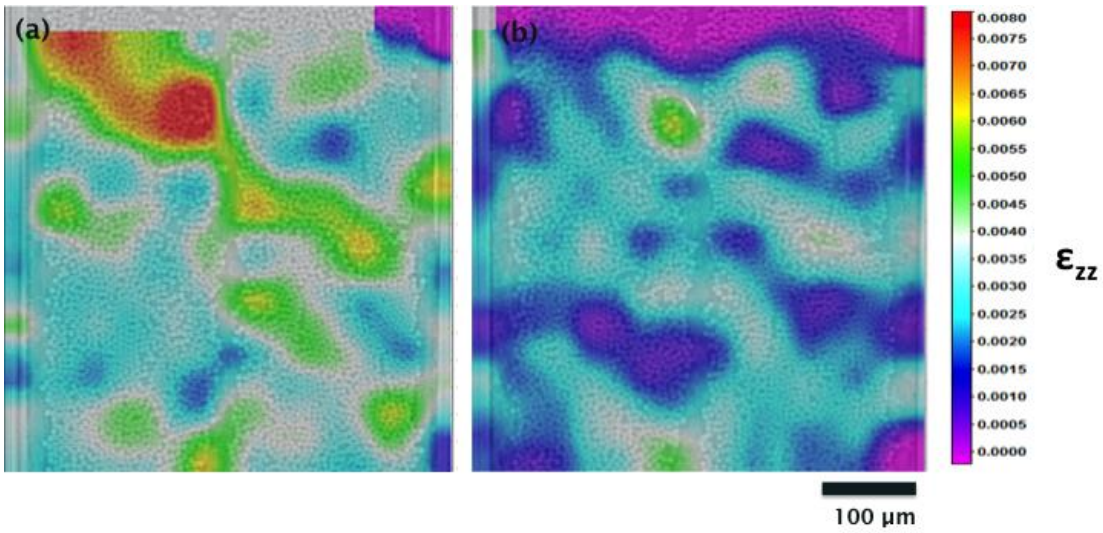

Figure 5-16 (a-b): DVC assessment at 23% UTS shows peak strain (a at x=0 µm) which penetrates into the bulk (b at x=200 µm) at the area of damage identified by SRCT.

The DVC algorithm calculates strain values from displacement measurements by comparing two volumes (reference and deformed). Any damage that occurs in the composite material; fibre matrix debond, microcracking and crazing for example, may be interpreted by the algorithm as displacement and hence strain. As a result, the strain values recorded by the DVC algorithm are open to interpretation. The resolution used for this study was chosen as it afforded a larger field of view than would have been achieved with a smaller voxel size, incorporating a large volumetric section of the notch, thus ensuring that transverse ply cracks could be captured. The limitation to this approach is that it is difficult to fully examine the damage to determine what form it takes. It is clear

from the SRCT and the DVC results that damage is increasing at each load step. In Figure 5-7 the damage in the right hand corner and highlighted in the red box evidently increases until the transverse ply crack forms, at which point the damage in the corner diminishes as the strain in the region is released.

5.7 Conclusion

The work presented here represents to the best of our knowledge the first use of synchrotron computed tomography and DVC for the identification of strains in three dimensions ahead of the formation of transverse ply cracks in LFRP, at microstructural scales of ~50-100μm perpendicular to the fibre, and several 100's of μm parallel to the fibres. As such, it is indicated that similar length-scales may be necessary to capture a representative volume element (RVE) for modelling purposes. Whilst some damage sites were associated with complex strain distributions that were difficult to link definitively to a specific strain concentration region, a majority of sites investigated here were quite clear in this correlation. The results are significant in allowing, for the first time, the correlation of damage initiation with prior local strain heterogeneity, and in turn with local microstructural parameters, i.e the length scales over which damage initiation occurs. This may then be an important step for the calibration and validation of micromechanics models. The path of the transverse ply crack observed in this work correlates with extended regions of locally high strain that precedes the formation of the crack.

This concludes the work presented in the paper. The conclusion below is presented for the work as a whole.

6 Conclusion

The aim of this work was to: a) advance understanding and hence the ability to predict damage initiation events in the transverse plies of CFRP and b) the development and verification of use of the existing DVC method which was identified as a potentially useful tool in this effort.

A literature review, Chapters 2 and 3 comprised a summary of a selection of more traditional methods of identifying transverse ply cracks in CFRP and highlighted the limitations of these approaches. The methodologies that would be used in the creation of this work were also explained and reviewed as was an appraisal of some established and modern modelling techniques.

The present work produced two chapters: a) methodology and verification and b) results, which were submitted as journal articles. In order not to repeat the conclusions of these chapters, the reader is referred to chapter 4 and 5 of this work.

Investigation of the influence of fibre volume fraction in damage initiation has proven inconclusive in this work. Microcracks have formed and developed in both high fibre volume fraction regions and low. A possible conclusion of this, although in no way substantiated, is that in this study notch geometry and existing surface damage may have played a bigger role in damage initiation.

Although no predictive modelling was conducted in this research, it is believed that the findings of this study will be potentially useful for future work in this field. Certain modelling techniques were identified which makes use of the SRCT and DVC techniques, the potential of the technique are illustrated in the future work chapter.

The author hopes that the results of the work has shown that the DVC and SRCT techniques are useful instigative tools for the study of damage initiation in CFRP. The development of techniques; the coupon orientation relative to the path of the beam to negate phase effects and the work conducted using DVC will potentially be of some value to future researchers. It is also hoped that at least a small contribution to our understanding of damage initiation in notched samples of CFRP has been made.

7 Future Work

The following section indicates future work that could further develop our understanding of damage initiation events, which will in turn aid the ability to predict performance. The work carried out to date has been about technique development and validation and has produced some exciting initial results, for example evidencing a length scale for representative volume elements within which local microstructure may control damage events.

7.1 Modelling

The modelling could be conducted in a similar way to the approach described in [38] whereby a cohesive zone model is used to predict the onset of fibre-matrix debonding; the non-linear behaviour in the matrix phase is modelled using Mohr-Coulomb plasticity. Microstructure, taken from the CT scans, may be processed using Avizo software (Avizo Standard Edition, 6.3.0, VSG, an FEI company, Burlington, USA) and meshed and transferred into FEA software. The displacement values determined from DVC can be used as boundary conditions applied directly to the external faces of a local mesh.

Initially a two-dimensional model could be trialled before a three-dimensional model is implemented. The three dimensions require extra boundary conditions to be applied. The determination of displacements to be used as boundary conditions in the x direction, along the fibre, has been shown to be challenging but either a manual calculation, an investigation as to the effect of the number of voxels used in the subvolume size in the fibre direction or the software's ability to track the displacement of the toughening particles might prove to be beneficial. The displacement and strain maps generated by the FEA model can be compared directly to the DVC results.

Once verified this technique could be used to extract and quantify the strain data ahead of damage initiation which can then be used to validate and inform the relevant theory, e.g. by validating the prediction of distortion and dilatational strains which may cause damage to initiate.

8 Poster presentation

Poster presented at ICTMS 2017, 3rd International Conference on Tomography of Materials and Structures Lund, Sweden 2017.

9 References

1. Van Paepegem, W. and J. Degrieck, *Fatigue degradation modelling of plain woven glass/epoxy composites.* Composites Part a-Applied Science and Manufacturing, 2001. **32**(10): p. 1433-1441.
2. Berthelot, J.M., et al., *Transverse cracking of cross-ply laminates .1. Analysis.* Composites Part a-Applied Science and Manufacturing, 1996. **27**(10): p. 989-1001.
3. Martyniuk, K., et al., *3D in situ observations of glass fibre/matrix interfacial debonding.* Composites Part a-Applied Science and Manufacturing, 2013. **55**: p. 63-73.
4. Garcia, I.G., V. Mantic, and E. Graciani, *Debonding at the fibre-matrix interface under remote transverse tension. One debond or two symmetric debonds?* European Journal of Mechanics a-Solids, 2015. **53**: p. 75-88.
5. Paris, F., E. Correa, and V. Mantic, *Kinking of transversal interface cracks between fiber and matrix.* Journal of Applied Mechanics-Transactions of the Asme, 2007. **74**(4): p. 703-716.
6. Correa, E., et al., *Effects of the presence of compression in transverse cyclic loading on fibre-matrix debonding in unidirectional composite plies.* Composites Part a-Applied Science and Manufacturing, 2007. **38**(11): p. 2260-2269.
7. Glud, J.A., et al., *Automated counting of off-axis tunnelling cracks using digital image processing.* Composites Science and Technology, 2016. **125**: p. 80-89.
8. Segui, J. 2015; Available from: https://www.comsol.com/blogs/protecting-aircraft-composites-from-lightning-strike-damage/.
9. Jon, G. and C. Stephen, *Strain invariant failure criteria for polymers in composite materials*, in *19th AIAA Applied Aerodynamics Conference*. 2001, American Institute of Aeronautics and Astronautics.
10. Tran, T.D., et al., *Micromechanical modelling for onset of distortional matrix damage of fiber reinforced composite materials.* Composite Structures, 2012. **94**(2): p. 745-757.
11. Scott, A.E., et al., *In situ fibre fracture measurement in carbon-epoxy laminates using high resolution computed tomography.* Composites Science and Technology, 2011. **71**(12): p. 1471-1477.
12. Wright, P., et al., *High resolution tomographic imaging and modelling of notch tip damage in a laminated composite.* Composites Science and Technology, 2010. **70**(10): p. 1444-1452.
13. Garcea, S.C., et al., *Fatigue micromechanism characterisation in carbon fibre reinforced polymers using synchrotron radiation computed tomography.* Composites Science and Technology, 2014. **99**: p. 23-30.
14. Bull, D.J., et al., *A comparison of multi-scale 3D X-ray tomographic inspection techniques for assessing carbon fibre composite impact damage.* Composites Science and Technology, 2013. **75**: p. 55-61.
15. Swolfs, Y., et al., *Synchrotron radiation computed tomography for experimental validation of a tensile strength model for unidirectional fibre-reinforced composites.* Composites Part a-Applied Science and Manufacturing, 2015. **77**: p. 106-113.

16. Borstnar, G., et al., *Three-dimensional deformation mapping of Mode I interlaminar crack extension in particle-toughened interlayers.* Acta Materialia, 2016. **103**: p. 63-70.
17. Bay, B.K., *Methods and applications of digital volume correlation.* Journal of Strain Analysis for Engineering Design, 2008. **43**(8): p. 745-760.
18. Bay, B.K., et al., *Digital volume correlation: Three-dimensional strain mapping using X-ray tomography.* Experimental Mechanics, 1999. **39**(3): p. 217-226.
19. Hussein, A.I., P.E. Barbone, and E.F. Morgan, *Digital Volume Correlation for Study of the Mechanics of Whole Bones*, in *Iutam Symposium on Full-Field Measurements and Identification in Solid Mechanics, 2011*, H.D. Espinosa and F. Hild, Editors. 2012. p. 116-125.
20. Liu, L. and E.F. Morgan, *Accuracy and precision of digital volume correlation in quantifying displacements and strains in trabecular bone.* Journal of Biomechanics, 2007. **40**(15): p. 3516-3520.
21. Lecomte-Grosbras, P., et al., *Three-Dimensional Investigation of Free-Edge Effects in Laminate Composites Using X-ray Tomography and Digital Volume Correlation.* Experimental Mechanics, 2015. **55**(1): p. 301-311.
22. Croom, B., et al., *Unveiling 3D Deformations in Polymer Composites by Coupled Micro X-Ray Computed Tomography and Volumetric Digital Image Correlation.* Experimental Mechanics, 2016. **56**(6): p. 999-1016.
23. Rethore, J., et al., *Three-dimensional analysis of fatigue crack propagation using X-Ray tomography, digital volume correlation and extended finite element simulations*, in *Iutam Symposium on Full-Field Measurements and Identification in Solid Mechanics, 2011*, H.D. Espinosa and F. Hild, Editors. 2012. p. 151-158.
24. Zauel, R., et al., *Comparison of the linear finite element prediction of deformation and strain of human cancellous bone to 3D digital volume correlation measurements.* Journal of Biomechanical Engineering-Transactions of the Asme, 2006. **128**(1): p. 1-6.
25. Madi, K., et al., *Computation of full-field displacements in a scaffold implant using digital volume correlation and finite element analysis.* Medical Engineering & Physics, 2013. **35**(9): p. 1298-1312.
26. Buljac, A., et al., *Numerical validation framework for micromechanical simulations based on synchrotron 3D imaging.* Computational Mechanics, 2017. **59**(3): p. 419-441.
27. Shakoor, M., et al., *On the choice of boundary conditions for micromechanical simulations based on 3D imaging.* International Journal of Solids and Structures, 2017. **112**: p. 83-96.
28. Fish, J., *Multiscale Modeling and Simulation of Composite Materials and Structures*, in *Multiscale Methods in Computational Mechanics: Progress and Accomplishments*, R. DeBorst and E. Ramm, Editors. 2011. p. 215-231.
29. Greco, F., L. Leonetti, and P. Nevone Blasi, *Adaptive multiscale modeling of fiber-reinforced composite materials subjected to transverse microcracking.* Composite Structures, 2014. **113**: p. 249-263.
30. Correa, E., V. Mantic, and F. Paris, *A micromechanical view of inter-fibre failure of composite materials under compression transverse to the fibres.* Composites Science and Technology, 2008. **68**(9): p. 2010-2021.

31. Smith, P.A., D.G. Gilbert, and A. Poursartip, *MATRIX CRACKING OF COMPOSITES INSIDE A SCANNING ELECTRON-MICROSCOPE.* Journal of Materials Science Letters, 1985. **4**(7): p. 845-847.
32. Canal, L.P., et al., *Application of digital image correlation at the microscale in fiber-reinforced composites.* Composites Part a-Applied Science and Manufacturing, 2012. **43**(10): p. 1630-1638.
33. Hull, D., & Clyne, T., *An Introduction to Composite Materials (Cambridge Solid State Science Series).* 1996, Cambridge: Cambridge University Press. doi:10.1017/CBO9781139170130.
34. Barton, J. *Transformation of Stress and Strain*. Available from: https://blackboard.soton.ac.uk/bbcswebdav/pid-2892790-dt-content-rid-2332417_1/courses/SESG6039-32830-15-16/Transformation of axes.pdf.
35. Seelio. Available from: https://seelio.com/w/1va9/composite-integrated-chip-ic-with-minimized-warpage.
36. Nairn, J.A. and S. Hu, *THE INITIATION AND GROWTH OF DELAMINATIONS INDUCED BY MATRIX MICROCRACKS IN LAMINATED COMPOSITES.* International Journal of Fracture, 1992. **57**(1): p. 1-24.
37. Nairn, J.A., S.F. Hu, and J.S. Bark, *A CRITICAL-EVALUATION OF THEORIES FOR PREDICTING MICROCRACKING IN COMPOSITE LAMINATES.* Journal of Materials Science, 1993. **28**(18): p. 5099-5111.
38. Mehdikhani, M., et al., *Multi-scale digital image correlation for detection and quantification of matrix cracks in carbon fiber composite laminates in the absence and presence of voids controlled by the cure cycle.* Composites Part B-Engineering, 2018. **154**: p. 138-147.
39. Case, S.W. and K.L. Reifsnider, *Micromechanical analysis of fiber fracture in unidirectional composite materials.* International Journal of Solids and Structures, 1996. **33**(26): p. 3795-3812.
40. Boniface, L., et al., *Transverse ply cracking in cross-ply CFRP laminates - Initiation or propagation controlled?* Journal of Composite Materials, 1997. **31**(11): p. 1080-1112.
41. Sebaey, T.A., et al., *Measurement of the in situ transverse tensile strength of composite plies by means of the real time monitoring of microcracking.* Composites Part B-Engineering, 2014. **65**: p. 40-46.
42. Gamstedt, E.K. and P. Brondsted, *Damage dissipation and localization during fatigue in unidirectional glass/carbon fibre hybrid composites*. Fatigue '99: Proceedings of the Seventh International Fatigue Congress, Vols 1-4, ed. X.R. Wu and Z.G. Wang. 1999. 1731-1736.
43. Gamstedt, E.K. and B.A. Sjogren, *Micromechanisms in tension-compression fatigue of composite laminates containing transverse plies.* Composites Science and Technology, 1999. **59**(2): p. 167-178.
44. Mortell, D.J., D.A. Tanner, and C.T. McCarthy, *An experimental investigation into multi-scale damage progression in laminated composites in bending.* Composite Structures, 2016. **149**: p. 33-40.
45. Maligno, A.R., N.A. Warrior, and A.C. Long, *Effects of inter-fibre spacing on damage evolution in unidirectional (UD) fibre-reinforced composites.* European Journal of Mechanics a-Solids, 2009. **28**(4): p. 768-776.
46. Hobbiebrunken, T., et al., *Influence of non-uniform fiber arrangement on microscopic stress and failure initiation in thermally and transversely*

loaded CF/epoxy laminated composites. Composites Science and Technology, 2008. **68**(15-16): p. 3107-3113.
47. Vaughan, T.J. and C.T. McCarthy, *Micromechanical modelling of the transverse damage behaviour in fibre reinforced composites.* Composites Science and Technology, 2011. **71**(3): p. 388-396.
48. Gonzalez, C. and J. Llorca, *Multiscale modeling of fracture in fiber-reinforced composites.* Acta Materialia, 2006. **54**(16): p. 4171-4181.
49. Sato, M., et al., *Temperature dependence of interfacial strength of carbon-fiber-reinforced temperature-resistant polymer composites.* Composite Structures, 2018. **202**: p. 283-289.
50. Vaughan, T.J. and C.T. McCarthy, *A combined experimental-numerical approach for generating statistically equivalent fibre distributions for high strength laminated composite materials.* Composites Science and Technology, 2010. **70**(2): p. 291-297.
51. Ge, W.J., et al., *An efficient method to generate random distribution of fibers in continuous fiber reinforced composites.* Polymer Composites, 2019. **40**(12): p. 4763-4770.
52. Hojo, M., et al., *Effect of fiber array irregularities on microscopic interfacial normal stress states of transversely loaded UD-CFRP from viewpoint of failure initiation.* Composites Science and Technology, 2009. **69**(11-12): p. 1726-1734.
53. Gentz, M., et al., *In-plane shear testing of medium and high modulus woven graphite fiber reinforced/polyimide composites.* Composites Science and Technology, 2004. **64**(2): p. 203-220.
54. Landis, E.N. and D.T. Keane, *X-ray microtomography.* Materials Characterization, 2010. **61**(12): p. 1305-1316.
55. Maire, E. and P.J. Withers, *Quantitative X-ray tomography.* International Materials Reviews, 2014. **59**(1): p. 1-43.
56. Youssef, S., E. Maire, and R. Gaertner, *Finite element modelling of the actual structure of cellular materials determined by X-ray tomography.* Acta Materialia, 2005. **53**(3): p. 719-730.
57. Liu, Y., et al., *Aggregate Morphological Characterization with 3D Optical Scanner versus X-Ray Computed Tomography.* Journal of Materials in Civil Engineering, 2018. **30**(1).
58. Novitskaya, E., et al., *Reinforcements in avian wing bones: Experiments, analysis, and modeling.* Journal of the Mechanical Behavior of Biomedical Materials, 2017. **76**: p. 85-96.
59. Bull, D.J., et al., *The influence of toughening-particles in CFRPs on low velocity impact damage resistance performance.* Composites Part a-Applied Science and Manufacturing, 2014. **58**: p. 47-55.
60. Lachambre, J., et al., *Extraction of stress intensity factors for 3D small fatigue cracks using digital volume correlation and X-ray tomography.* International Journal of Fatigue, 2015. **71**: p. 3-10.
61. Moffat, A.J., et al., *Micromechanisms of damage in 0 degrees splits in a [90/0](s) composite material using synchrotron radiation computed tomography.* Scripta Materialia, 2008. **59**(10): p. 1043-1046.
62. Wright, P., et al., *Ultra high resolution computed tomography of damage in notched carbon fiber-epoxy composites.* Journal of Composite Materials, 2008. **42**(19): p. 1993-2002.

63. Stamopoulos, A.G., K.I. Tserpes, and S.G. Pantelakis, *Multiscale finite element prediction of shear and flexural properties of porous CFRP laminates utilizing X-ray CT data.* Theoretical and Applied Fracture Mechanics, 2018. **97**: p. 303-313.
64. Stampanoni, M., et al., *Trends in synchrotron-based tomographic imaging: the SLS experience*, in *Developments in X-Ray Tomography V*, U. Bonse, Editor. 2006.
65. Hsieh, J., *Computed Tomography*. SPIE Press, Edgren, Fredrik. Wiley Inter-Science.
66. Hsieh, J., et al., *Recent Advances in CT Image Reconstruction.* Current Radiology Reports, 2013. **1**(1): p. 39-51.
67. 2005., I.; Available from: http://www.impactscan.org/impactcourseslides.htm.
68. Betz, O., et al., *Imaging applications of synchrotron X-ray phase-contrast microtomography in biological morphology and biomaterials science. 1. General aspects of the technique and its advantages in the analysis of millimetre-sized arthropod structure.* Journal of Microscopy-Oxford, 2007. **227**(1): p. 51-71.
69. ; Available from: http://www.instructables.com/id/How-to-Mount-Polish-and-Etch-a-Metallographic-Samp/.
70. Dowd, B.A., et al., *Developments in synchrotron x-ray computed microtomography at the National Synchrotron Light Source*, in *Developments in X-Ray Tomography Ii*, U. Bonse, Editor. 1999. p. 224-236.
71. Pan, B., et al., *Study on subset size selection in digital image correlation for speckle patterns.* Optics Express, 2008. **16**(10): p. 7037-7048.
72. Bay, B.K., *TEXTURE CORRELATION - A METHOD FOR THE MEASUREMENT OF DETAILED STRAIN DISTRIBUTIONS WITHIN TRABECULAR BONE.* Journal of Orthopaedic Research, 1995. **13**(2): p. 258-267.
73. Bay, B.K., et al., *Measurement of strain distributions within vertebral body sections by texture correlation.* Spine, 1999. **24**(1): p. 10-17.
74. McKinley, T.O. and B.K. Bay, *Trabecular bone strain changes associated with subchondral stiffening of the proximal tibia.* Journal of Biomechanics, 2003. **36**(2): p. 155-163.
75. McKinley, T.O. and B.K. Bay, *Trabecular bone strain changes associated with cartilage defects in the proximal and distal tibia.* Journal of Orthopaedic Research, 2001. **19**(5): p. 906-913.
76. McKinley, T.O., P.W. Callendar, and B.K. Bay, *Trabecular bone strain changes associated with subchondral comminution of the distal tibia.* Journal of Orthopaedic Trauma, 2002. **16**(10): p. 709-716.
77. Yeni, Y.N. and D.P. Fyhrie, *Finite element calculated uniaxial apparent stiffness is a consistent predictor of uniaxial apparent strength in human vertebral cancellous bone tested with different boundary conditions.* Journal of Biomechanics, 2001. **34**(12): p. 1649-1654.
78. Schoberl, E., et al., *Fibre-direction strain measurement in a composite ply under quasi-static tensile loading using Digital Volume Correlation and in situ Synchrotron Radiation Computed Tomography.* Composites Part a-Applied Science and Manufacturing, 2020. **137**: p. 18.

79. Smith, T.S., B.K. Bay, and M.M. Rashid, *Digital volume correlation including rotational degrees of freedom during minimization.* Experimental Mechanics, 2002. **42**(3): p. 272-278.
80. Franck, C., et al., *Three-dimensional full-field measurements of large deformations in soft materials using confocal microscopy and digital volume correlation.* Experimental Mechanics, 2007. **47**(3): p. 427-438.
81. Palanca, M., et al., *Three-Dimensional Local Measurements of Bone Strain and Displacement: Comparison of Three Digital Volume Correlation Approaches.* Journal of Biomechanical Engineering-Transactions of the Asme, 2015. **137**(7).
82. Gates, M., et al., *Subset Refinement for Digital Volume Correlation: Numerical and Experimental Applications.* Experimental Mechanics, 2015. **55**(1): p. 245-259.
83. Roberts, B.C., E. Perilli, and K.J. Reynolds, *Application of the digital volume correlation technique for the measurement of displacement and strain fields in bone: A literature review.* Journal of Biomechanics, 2014. **47**(5): p. 923-934.
84. Hild, F. and S. Roux, *Comparison of Local and Global Approaches to Digital Image Correlation.* Experimental Mechanics, 2012. **52**(9): p. 1503-1519.
85. Schreier, H.W. and M.A. Sutton, *Systematic errors in digital image correlation due to undermatched subset shape functions.* Experimental Mechanics, 2002. **42**(3): p. 303-310.
86. Yaofeng, S. and J.H.L. Pang, *Study of optimal subset size in digital image correlation of speckle pattern images.* Optics and Lasers in Engineering, 2007. **45**(9): p. 967-974.
87. Pan, B., Z.X. Lu, and H.M. Xie, *Mean intensity gradient: An effective global parameter for quality assessment of the speckle patterns used in digital image correlation.* Optics and Lasers in Engineering, 2010. **48**(4): p. 469-477.
88. Wang, Z.Y., et al., *Statistical analysis of the effect of intensity pattern noise on the displacement measurement precision of digital image correlation using self-correlated images.* Experimental Mechanics, 2007. **47**(5): p. 701-707.
89. Gonzalez, J. and J. Lambros, *A Parametric Study on the Influence of Internal Speckle Patterning for Digital Volume Correlation in X-Ray Tomography Applications.* Experimental Techniques, 2016. **40**(5): p. 1447-1459.
90. Jandejsek, I., O. Jirousek, and D. Vavrik, *Precise strain measurement in complex materials using Digital Volumetric Correlation and time lapse micro-CT data*, in *11th International Conference on the Mechanical Behavior of Materials*, M. Guagliano and L. Vergani, Editors. 2011. p. 1730-1735.
91. Forsberg, F. and C.R. Siviour, *3D deformation and strain analysis in compacted sugar using x-ray microtomography and digital volume correlation.* Measurement Science and Technology, 2009. **20**(9).
92. Forsberg, F., et al., *Full Three-Dimensional Strain Measurements on Wood Exposed to Three-Point Bending: Analysis by Use of Digital Volume Correlation Applied to Synchrotron Radiation Micro-Computed Tomography Image Data.* Strain, 2010. **46**(1): p. 47-60.

93. Verhulp, E., B. van Rietbergen, and R. Huiskes, *A three-dimensional digital image correlation technique for strain measurements in microstructures.* Journal of Biomechanics, 2004. **37**(9): p. 1313-1320.
94. Basler, S.E., et al., *Towards validation of computational analyses of peri-implant displacements by means of experimentally obtained displacement maps.* Computer Methods in Biomechanics and Biomedical Engineering, 2011. **14**(2): p. 165-174.
95. Wang, Y.Q., et al., *Quantitative Error Assessment in Pattern Matching: Effects of Intensity Pattern Noise, Interpolation, Strain and Image Contrast on Motion Measurements.* Strain, 2009. **45**(2): p. 160-178.
96. Dall'Ara, E., D. Barber, and M. Viceconti, *About the inevitable compromise between spatial resolution and accuracy of strain measurement for bone tissue: A 3D zero-strain study.* Journal of Biomechanics, 2014. **47**(12): p. 2956-2963.
97. Gillard, F., et al., *The application of digital volume correlation (DVC) to study the microstructural behaviour of trabecular bone during compression.* Journal of the Mechanical Behavior of Biomedical Materials, 2014. **29**: p. 480-499.
98. Zhu, M.L., et al., *Spatial resolution and measurement uncertainty of strains in bone and bone-cement interface using digital volume correlation.* Journal of the Mechanical Behavior of Biomedical Materials, 2016. **57**: p. 269-279.
99. Fushimi, S., T. Nagakura, and A. Yonezu, *Experimental and numerical investigations of the anisotropic deformation behavior of low-density polymeric foams.* Polymer Testing, 2017. **63**: p. 605-613.
100. Patterson, B.M., et al., *In situ X-ray synchrotron tomographic imaging during the compression of hyper-elastic polymeric materials.* Journal of Materials Science, 2016. **51**(1): p. 171-187.
101. Wismans, J.G.F., L.E. Govaert, and J.A.W. Van Dommelen, *X-Ray Computed Tomography-Based Modeling of Polymeric Foams: The Effect of Finite Element Model Size on the Large Strain Response.* Journal of Polymer Science Part B-Polymer Physics, 2010. **48**(13): p. 1526-1534.
102. Al-Athel, K.S., et al., *3D modeling and analysis of the thermo-mechanical behavior of metal foam heat sinks.* International Journal of Thermal Sciences, 2017. **116**: p. 199-213.
103. Chen, Y.M., R. Das, and M. Battley, *Finite element analysis of the compressive and shear responses of structural foams using computed tomography.* Composite Structures, 2017. **159**: p. 784-799.
104. Tagliabue, S., et al., *Micro-CT based finite element models for elastic properties of glass-ceramic scaffolds.* Journal of the Mechanical Behavior of Biomedical Materials, 2017. **65**: p. 248-255.
105. Ramezanzadehkoldeh, M. and B.H. Skallerud, *MicroCT-based finite element models as a tool for virtual testing of cortical bone.* Medical Engineering & Physics, 2017. **46**: p. 12-20.
106. Tran, T., et al., *A micromechanical sub-modelling technique for implementing Onset Theory.* Composite Structures, 2013. **103**: p. 1-8.
107. Tsai, S.W., *Theory of composites design*. A book for Composites design workshop series. 2008, Standford University.
108. SolidWorks. 2012; Available from: http://www.help.solidworks.com.

109. Gol'denblat, I.a.V.A.K., *Strength of glass reinforced plastic in the complex stress state.* Polymer Mechanics, 1966: p. 54-60.
110. Hart-Smith, L.J., *What the textbooks won't teach you about interactive composite failure criteria*, in *Composite Structures: Theory and Practice*, P. Grant and C.Q. Rousseau, Editors. 2001. p. 413-436.
111. Tay, T.E., et al., *Damage progression by the element-failure method (EFM) and strain invariant failure theory (SIFT).* Composites Science and Technology, 2005. **65**(6): p. 935-944.
112. Buchanan, D.L., et al., *Micromechanical enhancement of the macroscopic strain state for advanced composite materials.* Composites Science and Technology, 2009. **69**(11-12): p. 1974-1978.
113. Puck, A. and H. Schurmann, *Failure analysis of FRP laminates by means of physically based phenomenological models.* Composites Science and Technology, 2002. **62**(12-13): p. 1633-1662.
114. Kaddour, A.S., et al., *A comparison between the predictive capability of matrix cracking, damage and failure criteria for fibre reinforced composite laminates: Part A of the third world-wide failure exercise.* Journal of Composite Materials, 2013. **47**(20-21): p. 2749-U147.
115. Hashin, Z., *FAILURE CRITERIA FOR UNIDIRECTIONAL FIBER COMPOSITES.* Journal of Applied Mechanics-Transactions of the Asme, 1980. **47**(2): p. 329-334.
116. Puck, A., J. Kopp, and M. Knops, *Guidelines for the determination of the parameters in Puck's action plane strength criterion.* Composites Science and Technology, 2002. **62**(3): p. 371-378.
117. Hart-Smith, L.J., *Application of the strain invariant failure theory (SIFT) to metals and fiber-polymer composites (vol 90, pg 4263, 2010).* Philosophical Magazine, 2011. **91**(2): p. 353-353.
118. Pipes, R.B. and J.H. Gosse, *An Onset Theory for Irreversible Deformation in Composite Material*.
119. Cai, H.N., Y. Miyano, and M. Nakada, *Long-term Open-hole Compression Strength of CFRP Laminates based on Strain Invariant Failure Theory.* Journal of Thermoplastic Composite Materials, 2009. **22**(1): p. 63-81.
120. Chikhi, N., S. Fellahi, and M. Bakar, *Modification of epoxy resin using reactive liquid (ATBN) rubber.* European Polymer Journal, 2002. **38**(2): p. 251-264.
121. Lu, F., W.J. Cantwell, and H.H. Kausch, *The role of cavitation and debonding in the toughening of core-shell rubber modified epoxy systems.* Journal of Materials Science, 1997. **32**(11): p. 3055-3059.
122. Ha, S.K., et al., *Micromechanics of Failure for Ultimate Strength Predictions of Composite Laminates.* Journal of Composite Materials, 2010. **44**(20): p. 2347-2361.
123. Mayes, J.S. and A.C. Hansen, *Multicontinuum failure analysis of composite structural laminates.* Mechanics of Composite Materials and Structures, 2001. **8**(4): p. 249-262.
124. Griffiths, B. *Boeing sets pace for composite usage in large civil aircraft*. 2005; Available from: https://www.compositesworld.com/articles/boeing-sets-pace-for-composite-usage-in-large-civil-aircraft.

125. Dhakal, H.N., et al., *Abrasive water jet drilling of advanced sustainable bio-fibre-reinforced polymer/hybrid composites: a comprehensive analysis of machining-induced damage responses.* International Journal of Advanced Manufacturing Technology, 2018. **99**(9-12): p. 2833-2847.
126. Li, M.J., et al., *Experimental study on hole quality and its impact on tensile behavior following pure and abrasive waterjet cutting of plain woven CFRP laminates.* International Journal of Advanced Manufacturing Technology, 2018. **99**(9-12): p. 2481-2490.
127. Xu, J.Y., et al., *A Study on Drilling High-Strength CFRP Laminates: Frictional Heat and Cutting Temperature.* Materials, 2018. **11**(12): p. 13.
128. Schindelin, J., et al., *Fiji: an open-source platform for biological-image analysis.* Nature Methods, 2012. **9**(7): p. 676-682.
129. Hinton, M.J. and A.S. Kaddour, *Special Issue: The Second World-Wide Failure Exercise (WWFE-II): Part B: Evaluation of Theories for Predicting Failure in Polymer Composite Laminates Under 3-D States of Stress: Comparison with experiments Preface.* Journal of Composite Materials, 2013. **47**(6-7): p. 641-641.
130. Liu, K., Z.M. Yang, and H. Takagi, *Anisotropic thermal conductivity of unidirectional natural abaca fiber composites as a function of lumen and cell wall structure.* Composite Structures, 2014. **108**: p. 987-991.
131. Keyes, S.D., et al., *Mapping soil deformation around plant roots using in vivo 4D X-ray Computed Tomography and Digital Volume Correlation.* Journal of Biomechanics, 2016. **49**(9): p. 1802-1811.
132. Wang, Y., et al., *Using Local Edge Pattern Descriptors for Edge Detection.* International Journal of Pattern Recognition and Artificial Intelligence, 2018. **32**(3).
133. Garcea, S.C., I. Sinclair, and S.M. Spearing, *In situ synchrotron tomographic evaluation of the effect of toughening strategies on fatigue micromechanisms in carbon fibre reinforced polymers.* Composites Science and Technology, 2015. **109**: p. 32-39.
134. Borstnar, G., et al., *Interlaminar fracture micro-mechanisms in toughened carbon fibre reinforced plastics investigated via synchrotron radiation computed tomography and laminography.* Composites Part a-Applied Science and Manufacturing, 2015. **71**: p. 176-183.
135. Moffat, A.J., et al., *In situ synchrotron computed laminography of damage in carbon fibre-epoxy [90/0](s) laminates.* Scripta Materialia, 2010. **62**(2): p. 97-100.
136. Joffre, T., et al., *A 3D in-situ investigation of the deformation in compressive loading in the thickness direction of cellulose fiber mats.* Cellulose, 2015. **22**(5): p. 2993-3001.
137. Mortazavi, F., et al., *High resolution measurement of internal full-field displacements and strains using global spectral digital volume correlation.* Optics and Lasers in Engineering, 2014. **55**: p. 44-52.
138. Wilby, S.M., M.N.; Sinclair, I.; Spearing, S.M, *The measurement of transverse strains by digital volume correlation in a carbon fibre composite* in *In Progress*. 2019.